# NUMERICAL INVESTIGATION OF AIR-MIST SPRAY COOLING AND SOLIDIFICATION IN THE SECONDARY ZONE DURING CONTINUOUS CASTING

by

**Vitalis Ebuka Anisiuba**

**A Thesis**

*Submitted to the Faculty of Purdue University*
*In Partial Fulfillment of the Requirements for the degree of*

**Master of Science in Mechanical Engineering**

Department of Mechanical and Civil Engineering
Hammond, Indiana
December 2021

# THE PURDUE UNIVERSITY GRADUATE SCHOOL
# STATEMENT OF COMMITTEE APPROVAL

**Dr. Chenn Q. Zhou, Chair**
Department of Mechanical and Civil Engineering

**Dr. Hansung Kim, Member**
Department of Mechanical and Civil Engineering

**Dr. Ran Zhou, Member**
Department of Mechanical and Civil Engineering

**Approved by:**
Dr. Chenn Q. Zhou

*This work is dedicated to my parents and siblings whom despite the challenges of life, always support me in all that I do.*

# ACKNOWLEDGMENTS

I would like to acknowledge the Steel Manufacturing Simulation and Visualization Consortium (SMSVC) members for sponsoring this project. Special thanks to the project Technical Committee (PTC) members for their support all through the project. I would like to acknowledge the Center for Innovation through Visualization and Simulation (CIVS) for providing the resources needed for this project. CIVS also made me a better researcher, Engineer and Individual through the numerous programs and events they conduct. They helped in moulding me and brought forth some abilities that were latent in me. CIVS has helped me in improving my communication, presentation, time management and people’s skills as well as in many other facets of life. I am really happy to be part of CIVS family and I am highly indebted to CIVS.

I would like to thank my advisor, Professor Chenn Q. Zhou, for giving me the opportunity to be transformed through learning and development. I am really thrilled by her doggedness, tenacity, energetic, dynamic and goal-getting personality. She indeed is a moulder of people and she transforms weaknesses into strengths. Surely anyone that goes through her tutelage always comes out much better. I would also like to appreciate my other committee members, Professor Hansung Kim and Professor Ran Zhou. They were really part of my success story at Purdue. Not only did they review my thesis work, they also provided the ladder to my success through the course works I did under their tutor.

In a very special way, I would like to thank my mentors, Professor Armin Silaen and Dr. Haibo Ma. Words alone cannot express how grateful I am for the wonderful contributions and impact they made in my life. They did not only guide me through the project, they also helped in enhancing my analytical ability and improved on my sense of engineering judgement. They were ever ready to assist and support me all through the project. Technically speaking (in Dr. Haibo’s popular phrase), the success of my thesis lies in their efforts and support. I am very grateful and also opportune to work with these crops of mentors. I also appreciate Nick Walla, Professor Tyamo Okosun and Kyle Toth for their contributions and help in one way or the other towards accomplishing my project. I would like to thank all the past and present colleagues at CIVS especially the likes of John Resa, Saswot Thapa, Uzor Chukwunedum, Ogochukwu Oduruihe, Joel

Godinez, Rashed Al Manasir, Xipeng Guo, John Rosser, Xintong Liu, Sreelatha Sheshagoni etc. They made some useful impact towards my project and my stay at Purdue.

I would like to thank a very special friend and roommate, Emekwo Ukoha, who has been a pillar of support to me. Our 14 years of friendship has been full of support and encouragement. He always provides the shoulder to lean on when things get tough. My coming into the United States was greatly influenced by him. He is a friend turned brother and with him, I strongly believe in the adage that "family is not only by blood". Thanks very much for your unalloyed support. I would also like to thank all my friends, classmates, colleagues at my former places of work. All of you have in one way or the other impacted positively in my life and have been part of my success story. To my family, I love and cherish all you do for me, your prayers, encouragement and support. To my parents, Mr. Ambrose and Mrs. Anthonia Anisiuba, I pray that God will continually bless and keep you till old age. My twin sister, Chiamaka, whom is a better half of me, my other siblings, Aloysius, Chinaza and Evaristus, may God always be your guide, to bless and protect you all. I may be physically away from you people but my mind and spirit are always with you all.

To God Almighty, without whom we are nothing, I glorify you for making this journey a success. COVID-19 came shortly after I started this program yet it did not impact my academic program and I was able to accomplish it within the stipulated time. It is not by my might, it is only you, the I AM that I AM. May all adorations and thanksgiving be ascribed unto your holy name. For my family and friends who lost their lives or loved ones to COVID-19 or any other ailment, may your souls keep resting in peace. AMEN!

# TABLE OF CONTENTS

# LIST OF TABLES

# LIST OF FIGURES

# NOMENCLATURE

| | |
|---|---|
| St | Stoke’s number |
| $\Phi_v$ | dispersed phase volume |
| $\Phi_m$ | mass loading |
| $\epsilon$ | mean turbulent kinetic energy |
| $\tau_p$ | particle response time |
| $\tau_n$ | flow time scale |
| $\eta$ | Kolmogorov scale |
| d | particle density |
| $\rho_f$ | fluid density |
| $\rho_p$ | particle density |
| Fr | Froude number |
| $a_n$ | Kolmogorov acceleration |
| L | intact length |
| $t_s$ | sheet thickness |
| We | weber number |
| Re | Reynold’s number |
| $u_R$ | relative velocity |
| $\rho_l$ | liquid density |
| $\mu_l$ | liquid viscosity |
| $\sigma$ | surface tension |
| $u_l$ | liquid viscosity |
| $D_l$ | central tube diameter |
| $A_l$ | cross-sectional area for liquid |
| $A_g$ | cross-sectional area for liquid |
| $a_{NT}$ | parameter of Nukiyama-Tanasawa distribution |

|  |  |
|---|---|
| $p_{NT}$ | parameter of Nukiyama-Tanasawa distribution |
| $b_{NT}$ | parameter of Nukiyama-Tanasawa distribution |
| $q_{NT}$ | parameter of Nukiyama-Tanasawa distribution |
| $\mu_{drop}$ | droplet viscosity |
| Oh | Ohnesorge number |
| $\rho_{air}$ | air density |
| $\sigma_{drop}$ | droplet surface tension |
| $d_{drop}$ | droplet diameter |
| h | heat transfer coefficient |
| q | heat flux |
| $T_w$ | wall temperature |
| $S_{air\text{-}drop}$ | source term |
| g | gravity |
| $V_{cell}$ | cell volume |
| $\chi$ | composition field |
| $\Omega$ | maximum growth rate of wavy turbulence |
| $\Lambda$ | dominance wavelength of wavy disturbances |
| $T_{drop}$ | droplet temperature |
| $T_R$ | radiation temperature |
| $h_{fg}$ | latent heat of droplet |
| $\mu_{air}$ | air density |
| $C_D$ | drag coefficient |
| $x_{drop}$ | droplet position vector |
| $\sigma_{SB}$ | Stefan-Boltzmann constant |
| $\varepsilon_{drop}$ | droplet emissivity |
| $c_p$ | specific heat of droplet |
| $C_s$ | concentration of the vapour at droplet surface |

| | |
|---|---|
| $C_\infty$ | concentration of the vapour in the bulk flow |
| $\Psi$ | the impinge angle on the horizontal plane |
| $H_\pi$ | sheet height at $\psi = \pi$ |
| $\beta_\omega$ | k-ω SST turbulence model coefficient |
| $\beta_k$ | k-ω SST turbulence model coefficient |
| $m_{drop}$ | mass of droplet |
| $\rho_{steel}$ | density of steel |
| $k$ | turbulent kinetic energy |
| $\bar{\bar{\tau}}$ | stress tensor |
| $T_{liq}$ | liquidus temperature |
| $T_{sol}$ | solidus temperature |
| $f_{sol}$ | solid fraction |
| $h_{lat}$ | latent heat release |
| $u_{steel}$ | velocity of steel |
| $G_k$ | generation of turbulence kinetic energy due to mean velocity gradients |
| $G_\omega$ | generation of specific dissipation rate due to mean velocity gradients |
| $u_{stationary}$ | velocity of the stationary reference frame |
| $u_{moving}$ | velocity of the moving reference frame |
| $u_r$ | relative velocity between the stationary and moving reference frames |
| $V_{casting}$ | casting speed |
| $D_{standoff}$ | standoff distance |
| $Q_{water}$ | water flow rate |
| $P_{air}$ | air pressure |

# ABSTRACT

As a result of the intense air-water interaction in the spray nozzle, air-mist spray is one of the most promising technologies for attaining high heat transfer. CFD simulations and multivariable linear regression were used in the first part of this study to analyze the air-mist spray produced by a flat-fan atomizer and to predict the heat transfer coefficient using the casting operating conditions such as air pressure, water flow rate, cast speed and standoff distance. For the air-mist spray cooling simulation, a four-step simulation method was utilized to capture the turbulent flow and mixing of the two fluids in the nozzle, as well as the generation, transport, and heat transfer of droplets. Analysis of the casting parameters showed that an increase in air pressure results in efficient atomization, increases the kinetic energy of the droplets and produces smaller droplet size thus, the cooling of the slab increases significantly. Also, a decrease in water flow rate, standoff distance and casting speed would result in more efficient cooling of the steel slab. The second part of the study investigated the solidification of steel in the secondary cooling region. Caster geometry and casting parameters were studied to evaluate their impact on the solidification of steel. The parameters studied include roll gap, roll diameter, casting speed and superheat. It was found that a smaller ratio of roll gap to roll diameter is more efficient for adequate solidification of steel without any defect. Casting speed was found to have a significant effect on the solidification of steel while superheat was found to be insignificant in the secondary zone solidification. The result from the air-mist spray cooling was integrated into the solidification model to investigate the solidification of steel in the entire caster and predict the surface temperature, shell growth and metallurgical length. To replicate real casting process, temperature dependent material properties of the steel were evaluated using a thermodynamic software, JMatPro. The air-mist spray model was majorly investigated using ANSYS Fluent 2020R1 CFD tool while the solidification of steel was studied using STARCCM+ CFD software. Using the findings from this study, continuous casting processes and optimization can be improved.

# 1. INTRODUCTION

## 1.1 Continuous casting overview

Secondary cooling is critical in the continuous casting process, which was introduced in the late 1950s and is now used to produce more than 90% of the steel in the world [1,2]. In 2009, global crude steel production exceeded 1220 million tons, with continuously cast steel accounting for 92 percent of total output. [3] Consequently, spray cooling's significance in this and many other processes in which it is involved becomes evident since spray cooling is crucial.  Figure 1-1 shows the continuous casting process.

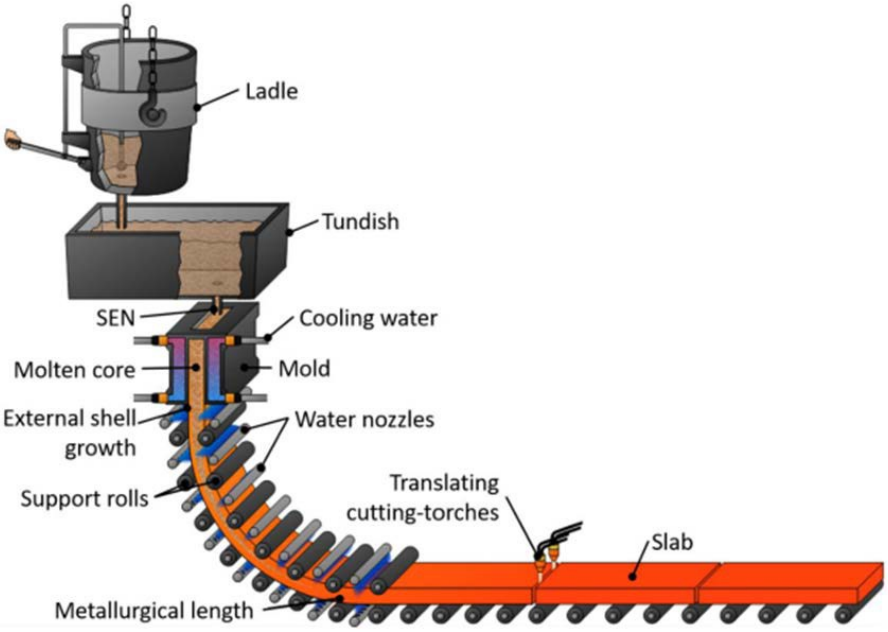

Figure 1-1. Continuous casting process [4]

At around 1473 K (1200 °C), a solidified shell in steel CC exits the mold or primary cooling system. In order to guarantee full solidification across its thickness, the strand enters a containment-spray-cooling setup known as the secondary cooling system, which is comprised of tightly spaced support rollers between which nozzles are interspaced to produce a spray cooling pattern. The secondary cooling system of CC machines (i.e., direct spray impingement, roll contact, radiation, and convection to draining water) contributes for roughly 60 percent of the heat drained via this system, although this contribution may be substantially bigger in its upper zones [6,7].

## 1.2 Motivations and Objectives

The continuous casting process, in which liquid steel is solidified by a water-cooled mold and water sprays to form semi-finished slabs or billets, accounts for approximately 98 percent of crude steel produced in the United States. Secondary cooling is a complex operation since the rate at which the slab is cooled has a direct impact on the surface quality and interior quality. The removal of heat from the slab must be effective without causing slab cracking and deformation. Steel manufacturers must deal with inefficient spray cooling and solidification, which reduces steel quality by causing defects such as cracking and breakout. One of the new trends in continuous casting to improve yield and energy efficiency is to use real-time online dynamic casting control systems, which are designed to consistently produce high quality steel products using real-time temperature measurements and dynamic adjustment of spray cooling rate. The main difficulty is obtaining an accurate Heat Transfer Coefficient (HTC) on the surface of the steel product as a boundary condition for on-site real-time heat transfer and solidification calculations. Extensive effort has been put into developing HTC correlations to predict spray cooling rate experimentally.

These correlations, however, are limited to a few operating conditions. Not only is the development process labor-intensive, but the correlation may fail to predict correct HTC when process changes occur. As a result, knowledge and understanding of the heat transfer phenomena occurring during the secondary cooling process in continuous steel casting are critical for controlling and optimizing the process. Non-optimized solidification also results in inhomogeneous steel properties. As a result, the project entailed modeling continuous casting with computational fluid dynamics tools in order to control and optimize the process. The study attempts to develop a 3-D CFD model to simulate droplet formation, droplet transport, and impingement heat transfer during secondary cooling using an air-mist nozzle, as well as to investigate the effect of casting parameters for air-mist nozzles such as air pressure, water flow rate, casting speed, and standoff distance, and to generate a multivariable correlation that can predict the lumped HTC at any casting condition. It then investigated the steel solidification process further by assessing the impact of roll gap, roll diameter, casting speed, and superheat, and then used an integration strategy to model the solidification of the entire continuous caster to predict the metallurgical length and slab temperature.

### 1.3 Simulation software

In the field of computational fluid dynamics (CFD), numerical techniques and algorithms are used to analyze fluids in several phases in both reacting and non-reacting flows, and may include a variety of thermodynamic, heat transport, turbulence and chemical reaction complexity. To create an accurate and representative CFD model, several disciplines including engineering, mathematics, and computer science are used. They may be used for predictive reasons including testing new scenarios that would be too unsafe or costly to execute in current operations, testing how processes would scale up, modeling the repercussions of potentially hazardous circumstances or regulating and optimizing existing processes. Modeling fluid dynamics is based on mass conservation, momentum conservation and energy conservation, the three basic governing equations. Because of the complicated nature and physics of solidification, creating an in-house code to determine F&S within a caster would be time consuming. As a result, commercial CFD software like ANSYS, Star-CCM+, or COMSOL would be preferable. The air-mist spray study was carried out using ANSYS Fluent 2021 R1 (ANSYS Inc., Pittsburgh, PA, USA), renowned for its sophisticated physics modeling capabilities and industry-leading precision in fluid simulation software. Because of its advanced solidification modeler, superior mesh options, and ease of handling data in table format, the STAR CCM+ software (Siemens Digital Industries Software, Plano, Texas, USA) was used to study steel solidification.

# 2. LITERATURE REVIEW

## 2.1 Air-mist spray cooling process

Atomization is the breakdown of a large volume of liquid into a large number of individual droplets. [8]. It was postulated by [9] postulated that an unstable wave development on the liquid jet's surface is the result of aerodynamic interaction between the liquid and the gas. A spray is a jet of fine particles (of different drop sizes) of liquid discharged from an atomizer for a direct application to a surface. Sprays may be made in several ways. One of the most fundamental aspects of atomization is the hydraulics of atomization itself, which is governed by flow dynamics inside the atomizer. The shape and penetration of the spray, as well as its specific characteristics of number density, drop velocity, and drop size distribution as functions of time and space, are all determined by the development of the jet or sheet and the growth of small disturbances that eventually lead to disintegration into ligaments and then drops as shown in Figure 2-1

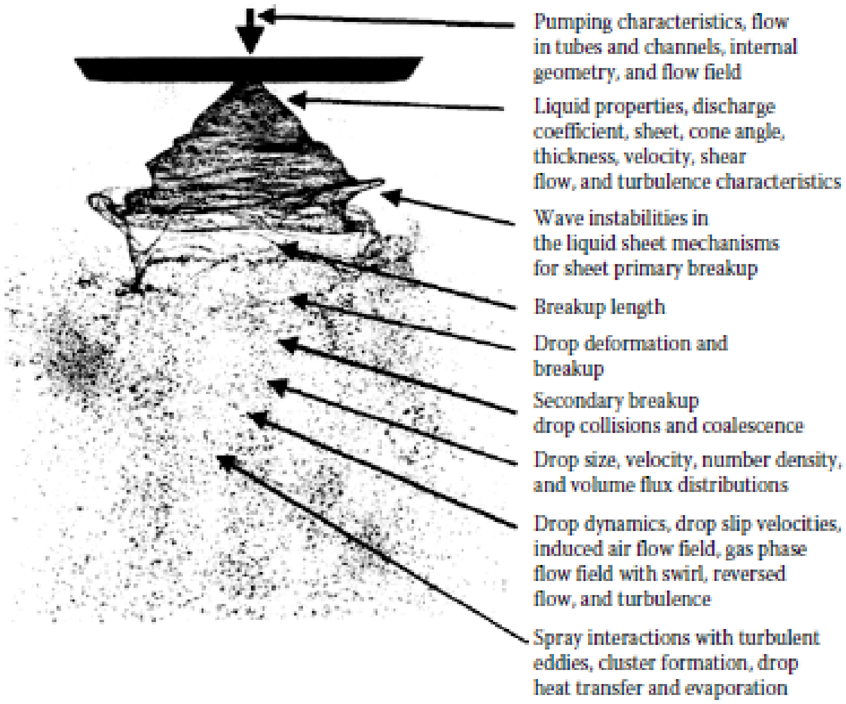

Figure 2-1. Droplets forming process [9]

Basically, air-water mist is a suspension of very small droplets of water in an air jet that is created as a result of liquid shearing and then atomization caused by pressured air jet impingement on the margin of the liquid opening. The kinetic energy of a moving airstream is used by air-mist atomizers to fracture a liquid jet or sheet into ligaments and then droplets. For quenching metal plates in research and development, air-atomized spray is becoming increasingly popular due to its ability to extract more heat from the plate in a shorter period of time [9]. Air-mist atomizers have the potential to break a liquid jet or sheet into ligaments and then droplets by utilizing the kinetic energy of a flowing airstream [8]. Since the late 1970s, there has been a lot of discussion on air-mist heat extraction studies. When compared to spray—hydraulic—nozzles, the wide range of cooling conditions [10,11], from mild to intense, as well as the low proclivity to clogging, have been underlined as advantages of air-mist—pneumatic—nozzles. As a result, there is a large turn down (ratio between lowest and maximum flow) and a high degree of control over air/water volumetric ratios [12]. Furthermore, it was asserted that air-mist nozzles, rather than hydraulic nozzles, resulted in fewer longitudinal cracks than hydraulic nozzles because they reduced changes in slab surface temperature [47]. Using the same water flow rate in an experiment, mist cooling had a higher heat transfer coefficient than spray cooling [11,13], as would be predicted given that mist cooling includes the application of a pressure that affects the properties of water droplets, resulting in more intense mist cooling. Fine droplets are produced by air mist nozzles, and evaporation is the primary source of their cooling effect. This type of nozzle has a wide range of controllability, and the intensity of the cooling can be changed by varying the air and water pressures [14]. Comparatively speaking, they can distribute spray droplets at higher velocities than typical hydraulic systems inside their own created gas flow fields. In addition, the drop size generated by them is typically less than that produced by simple hydraulic atomizers [15]. The use of air mist nozzles with flat jets in continuous steel casting production for secondary cooling has been proven for over fifteen years. [16,17]. This kind of atomizer has one major drawback: it requires an external source of high-pressure air [8].

### 2.1.1 Multiphase Flow

Mass, momentum, and energy coupling between phases are critical in dispersed multiphase flows. In dispersed multiphase flows, the development of the interface between the phases is seen as of minor concern. It is true that processes such as droplet or bubble breakup and agglomeration affect the interface between the phases. Dispersed multiphase flows, on the other hand, account for the particle-size spectra of the interface between the dispersed and carrier phases without addressing the detailed development of the interface [18]. Depending on the dispersed phase volume percentage, turbulent flows containing particles may be generically classified as either dilute or dense [19]. Fluid drag and lift are the primary forces that control particle motion in dilute flows while interparticle collisions are nonexistent. However, collisions or continuous contact are used to regulate the movement of particles in dense flows. There are two important factors that influence the degree of interaction between the phases: fractional volume occupied by the dispersed phase ($\Phi_v$) and mass loading ($\Phi_m$), defined as the mass ratio of dispersed phase to carrier phase. Dispersed phase dynamics are strongly influenced by the turbulent flow of the carrier when $\Phi_v$ and $\Phi_m$ are modest (i.e., one-way coupled). Dispersed phase dynamics cannot be disregarded when the dispersed phase's mass is equivalent to that of the carrier phase's mass (i.e., two-way coupled). A four-way coupling regime occurs as $\Phi_v$ rises, resulting in interactions between particles (such as collision, aggregation and break-up) becoming more essential. When it comes to particle distribution, the phenomena of preferential accumulation [22-24] is one of the most important. Even in isotropic turbulence, particle distribution is not uniform, as is now well acknowledged. To prevent vorticity, heavy-than-fluid particles prefer to cluster in areas of high strain rate. Vortical zones, on the other hand, tend to attract lighter-than-fluid particles (or bubbles). There is also a stochastic component introduced to interphase coupling when the Reynolds number of the particles exceeds a few hundred.

Due to the varying inertias of the two particles involved, the motion of inertial particle pairs may be significantly influenced. Dispersion of droplets in a fluid is critical for effective mass and temperature exchange between the two phases. The authors in [32] observed that lowering the Froude number (Fr) leads to an increase in the accelerations but a decrease in their intermittency, whereas for monodisperse particles, decreasing the Fr leads to a uniform suppression of the inertial particle relative velocities in all directions. [33,34]. Particle inertia can be characterized by the

Stokes number, $St \equiv \tau_p/\tau_\eta$, where $\tau_p$ is the particle response time, $\tau_\eta$ is the flow time scale, and can also be expressed as

$$St = \frac{\rho_p - \rho_f}{18\rho_f}\left(\frac{d}{\eta}\right)^2 \tag{1}$$

where η is the kolmogorov scale, d is the particle diameter, ϵ is the mean turbulent kinetic energy dissipation rate, $\rho_p$ and $\rho_f$ are the particle and fluid density. Gravity's influence on flow may be quantified using the Froude number,

$$Fr = \frac{a_n}{g} = \frac{\epsilon^{\frac{3}{4}}}{v^{\frac{1}{4}}g} \tag{2}$$

where $a_\eta \equiv u_\eta/\tau_\eta$ is the Kolmogorov acceleration [32,33]. Bidispersity alone has been observed to increase particle relative velocities, and this relative speeds are further increased by gravity [35-38]. Due to gravitational settling, the effects of the Reynolds number $R_\lambda$ on particle acceleration are magnified for Stokes numbers St greater than 1. Furthermore, gravity affects how inertial particles interact with the turbulent flow by altering the particle settling velocity [30,39]. gravity causes particles to descend through a fluid flow, which decreases their velocity compared to a fluid flow without gravity [34]. In the regime $Fr \ll 1$ and $St \geq O(1)$, gravity has a substantial impact on particle displacement over time because of the rapid settlement of the particles [32,35]. But when $|\Delta St| \ll 1$, gravity reduces the relative dispersion because settling velocity is minimal, and gravity reduces the nonlocal contribution to particle dynamics [32,35]. For $Fr=\infty$, because inertial particles avoid strongly vortical regions where fluid acceleration is rapid, and because of the filtering effect, which makes the particles sluggish with increasing St, they have a modulated response to fluid accelerations along their trajectory, the particle accelerations decrease monotonically with increasing St. [40,41]. Particles dispersing with and without gravity were studied by [42] using DNS, and they observed that the differential settling velocities of the particles led to a quicker relative dispersion of bidisperse compared to those dispersing without gravity.

### 2.1.2 Jet Breakup (Primary atomization)

Droplet size can be controlled by studying the jet breakdown mechanism in great detail. Liquid-jet breakup length has a direct correlation with the breakup method or mechanism. There are two distinct steps in the atomization of liquid jets: the primary breakup near the atomizer outlet and the following secondary breakup of the arbitrary-shaped liquid ligaments and the big droplets created from the main breakup farther downstream [36,37]. According to [38], surface oscillations are generated when a liquid jet emerges from an atomizer due to the conflict between cohesive and disruptive forces on its surface. The liquid jet is disintegrated into ligaments or droplets if the vibrations are intensified in the right circumstances. In this process, which is known as primary atomization, pressure, aerodynamics, centrifugal, surface tension, and internal effects including turbulence and velocity profile relaxation are all involved [8].

It is the shear stress at the liquid gas interface that breaks up the liquid jet in the primary breakup zone [8,39-41]. The jet breakup length, which is the length of the continuous liquid core corresponding to full fragmentation of the jet into droplets and ligaments, is used to measure the extent of the main atomization zone. Liquid-to-gas velocities, the shape of the nozzle's spout, and both fluids' physical qualities all influence the breakup length [39,42]. Liquid jet breakup length in air-blast atomizers has been measured in the past by a number of researchers [39,40,43-46]. The shadowgraphic representation of the jet is used in the majority of these investigations. However, the dense cloud of droplets and ligaments surrounding the liquid core typically inhibits proper probing of the main breakdown zone.. However, according to [40], even when the atomizing gas and intake liquid flows are stable and oscillation-free, the spray properties (such as liquid volume flux and droplet number density) downstream of the atomizer are subjected to periodic temporal changes.

The liquid jet is vulnerable to a variety of instabilities, including capillary, helical, Kelvin–Helmholtz (KH) instability, etc., and many processes of breakdown of the liquid core and ligaments have been found in prior investigations. When a critical waveform is achieved on the liquid–air contact, the liquid jet breaks into ligaments and/or droplets [36,39,47]. Researchers in [39] found that the wave frequency at the nozzle exit rises with increasing gas velocity. Due to the amplification of the primary instability, lateral parts of a liquid jet near the nozzle exit undergo high accelerations in a direction perpendicular to their surfaces, rendering them vulnerable to the RT instability. As a result, inside the potential core of the large-diameter gas jet the liquid jet completely disintegrates into a fine spray of water. Primary atomization may be caused by KH instability, according to many previous studies [48-50]. Droplets and ligaments may form as a result of RT instability, which is brought on by the limited amplitude of waves on the jet surface and by the flap of the jet itself, as previously noted. However, despite the fact that the two primary effects (capillary instability and hydrodynamic interaction) are firmly established from a qualitative point of view, there has been no definite quantitative agreement between theoretical analysis and actual breakup length [51].

When a thin water sheet was placed in a co-current high-speed air stream, the breakup frequency, intact length, droplet velocity and mean droplet diameter were quantified by experimentation. Values from a large number of photos were used to calculate intact measurements. As a function of sheet thickness, the Reynolds number, and the Weber number, an empirical equation was established as:

$$L = 1.23 t_s^{0.5} We^{-0.5} Re^{0.6} \tag{3}$$

where L and $t_s$ are the intact length and sheet thickness in millimeters. The Weber number and Reynolds number are defined as

$$We = t_s \rho_A \frac{u_R^2}{2\sigma} \tag{4}$$

$$Re = \frac{t_s u_L \rho_L}{\mu_L} \tag{5}$$

where $\rho_A$ is the gas density; $u_R$, is the relative velocity between the liquid sheet and gas; $\sigma$ is the surface tension; and $u_L$, $\rho_L$, and $\mu_L$ are the liquid velocity, density, and viscosity, respectively. For a fixed liquid sheet thickness, the intact length decreases as the relative velocity between the gas and the liquid increases. The length of the liquid sheet rises as the velocity of the liquid increases. Spinners' sheets were measured and a relationship between sheet thickness and flowrate was charted by [52], as illustrated in Figure 2-2.

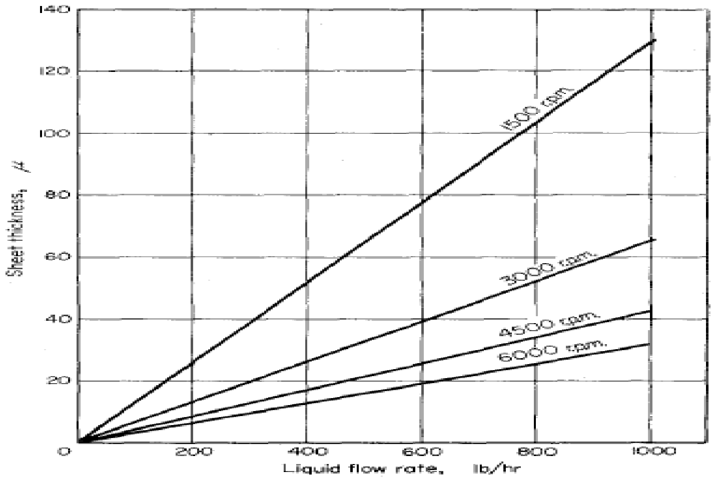

Figure 2-2. Variation of shell thickness against flow rate

Some researchers proposed some empirical correlations to evaluate the jet breakup length which are summarized in Table 2-1.

Table 2-1. Experimental correlations for the mean jet breakup length in coaxial

| Researchers | Breakup length correlation | Operating conditions |
|---|---|---|
| Eroglu et al. [39] | $\frac{L}{D_l} = 0.66 We_g^{-0.4} Re_l^{0.6}$ | $Re_l$ = 1100 – 18000, $We_g$= 13 – 267 |
| Leroux et al. [44] | $\frac{L}{D_l} = \frac{10}{M^{0.3}}$ | $Re_l$ = 45 – 1000, $We_g$=1-1000, M= 0.17 – 60 |
| Zhao et al. [45] | $\frac{L}{D_l} = 5.2(\frac{A_l}{A_g})^{-0.17} M^{-0.28}$ | $Re_l$ = 783 – 35000, $We_g$= 8.8 – 455, M= 0.011 – 620 |
| Kumar et al [46] | $\frac{L}{D_l} = 0.27 We_g^{-0.18} Re_l^{0.44}$ | $Re_l$ = 3000 – 5000, $We_g$= 80 – 300, M= 1.1 – 8.3 |
|  | $\frac{L}{D_l} = \frac{5.45}{M^{0.22}}$ |  |
| Engelbert et al. [40] | $\frac{L}{D_l} = 40 We_{exit}^{-0.27}$ | $Re_l$ = 5000 – 35000, $We_{exit}$= 70 – 2600 |

$A_l$ and $A_g$ are the cross-sectional area for the liquid and air flow, respectively, at the exit of the atomizer, $D_l$ is the central tube inner diameter. $We = \rho_g \frac{(u_g - u_l)^2 D_l}{\sigma}$, $M = \frac{\rho_g u_g^2}{\rho_l u_l^2}$, $Re_l = \frac{\rho_l u_l D_l}{\mu_l}$

### 2.1.3 Droplet size and velocity

Droplets formed by jet disintegration have a wide range of diameters due to the heterogeneous nature of the atomization process. The size of droplets in most practical applications ranges from a few micrometers to a few hundred micrometers [8]. A thorough understanding of droplet size distribution is required for basic heat and mass transfer analysis [53]. It is mathematically convenient to represent the droplet size distribution in a spray by a continuous function, along with an arbitrarily defined representative diameter and some measure of deviation from this mean diameter. Table 2-2 lists some of the most well-known representative diameters.

Table 2-2. Droplet size definitions

| **Diameter** | **Definition** |
|---|---|
| $D_{V0.1}$ | 10 % of total liquid volume or mass has diameters smaller or equal to it |
| $D_{32}$ | Sauter mean diameter (SMD) has the same volume to surface area ratio |
| $D_{V0.5}$ | Volume mean diameter (VMD) 50 % of total liquid volume or mass has diameters larger than the median value and 50 % smaller than median value |
| $D_{V0.9}$ | 90 % of total liquid volume or mass has diameters smaller or equal to it |

Another well-known dimension is the mean diameter. Although the mean diameter is useful in many calculations and mathematical derivations, it is not the same as the representative diameter in nature. Mugele and Evans established the concept of mean diameter in 1951 [53]. The general form of mean diameter is illustrated in Eq. (5). The order of the mean diameter is calculated as the sum of a + b.

$$D_{ab} = \left[\frac{\sum N_i D_i^a}{\sum N_i D_i^b}\right]^{\frac{1}{a-b}} \tag{6}$$

Where $Ni$ is the number of droplets in size range $i$ and $Di$ is the middle diameter of size range $i$. It is worth mentioning that no single mean diameter is superior to another and no single universal mean diameter can completely define the droplet size distribution in any spray. Table 2-3 shows some of the mean diameter definitions and their applications.

Table 2-3. Mean diameter definitions

| a | b | a + b | Name | Definition | Applications |
|---|---|---|---|---|---|
| 1 | 0 | 1 | Arithmetic mean | $D_{10} = \frac{\sum N_i D_i}{\sum N_i}$ | Comparisons |
| 2 | 0 | 2 | Surface mean | $D_{20} = \sqrt{\frac{\sum N_i D_i^2}{\sum N_i \, D_i}}$ | Surface area controlling |
| 3 | 0 | 3 | Volume mean | $D_{30} = \sqrt{\frac{\sum N_i D_i^3}{\sum N_i}}$ | Volume controlling |
| 3 | 2 | 5 | Sauter mean | $D_{32} = \frac{\sum N_i D_i^3}{\sum N_i \, D_i^2}$ | Mass transfer |
| 4 | 3 | 7 | De Brouckere mean | $D_{43} = \frac{\sum N_i D_i^4}{\sum N_i \, D_i^3}$ | Combustion equilibrium |

The continuous frequency distribution curves outperform the discrete histograms when it comes to representing the droplet size distribution. A continuous function with only a few parameters can be used to uniquely determine a frequency distribution curve. This is useful for smoothing results when only a small number of measurements are available, as well as extrapolating droplet sizes outside of the measurement range. Normal, log-normal, four-parameter log-hyperbolic, three-parameter log-hyperbolic, Nukiyama-Tanasawa, Rosin-Rammler, and modified Rosin-Rammler distribution functions are among the most well-known droplet size distribution functions. Among all the size distribution functions, the four-parameter log-hyperbolic equation and the Nukiyama-Tanasawa equation are best known for their accuracy and flexibility. Both equations, however, have shortcomings. The four-parameter log-hyperbolic equation is extremely sensitive to even minor changes and may exhibit numerical stability issues [54, 55]. It is only advised if detailed information about size variation is required throughout the spray [56]. The Nukiyama-Tanasawa equation, on the other hand, necessitates simultaneous optimization of the four parameters [8] and is written as follows:

$$f(D) = a_{NT} D^{p_{NT}} exp[-(b_{NT} D)^{q_{NT}}] \qquad (7)$$

where $a_{NT}, b_{NT}, p_{NT}, q_{NT}$ are the Nukiyama-Tanasawa model constants. It is only possible if the multivariable regression analysis can be performed by computer software. As a result, relatively simple two-parameter equations are more popular in the engineering community. The Rosin-Rammler equation, also known as the Weibull distribution, is the most commonly used simple distribution function [57]. The two constants in the equation are the representative diameter of some kind, X, and the spread number, q. The spread number indicates the spread of droplet size around the representative diameter. The spread number of an ideal spray that produces droplets of uniform size is infinite. The spread number for the majority of the sprays ranges from 1.5 to 4 [8]. Because of the nature of its mathematical expression, the Rosin-Rammler equation can only be used for single-peaked size distributions. Nonetheless, the Rosin-Rammler equation will remain popular due to its simplicity.

Another important feature of a spray is its droplet velocity. It has an immediate impact on the subsequent impingement outcome, which determines droplet-wall heat transfer. Particle Image Velocimetry (PIV) [57-59] and Laser Doppler Velocimetry (LDV) [60-62] are two techniques for measuring droplet velocity. The PIV technique has the advantage of being able to generate two-dimensional or even three-dimensional velocity vector fields, whereas LDV only measures velocity at a single point. Zhang et al. [63] conducted a recent evaluation of both techniques. They measured droplet velocity in an air-mist spray using both techniques and concluded that the LDV technique outperforms the PIV technique near the nozzle tip. They proposed a new technique, which is a combination of PIV and LDV, to improve the accuracy while minimizing measurement efforts. The labor-intensive LDV measurement is recommended for the region near the nozzle tip, while the PIV technique can be used to resolve the velocity field further downstream.

### 2.1.4 Droplet breakup and collision (secondary atomization)

The droplet breakup and collision mechanisms are critical in numerical simulations. The droplet breakup and collision mechanisms are only required when the simulation uses the Lagrangian approach. Droplets are treated as discrete points moving through a continuous gas/liquid phase in this method. Droplets in numerical simulations do not deform and break up, nor do they collide and coalesce, as they do in the physical world, due to the nature of the point mass assumption. Thus, breakup and collision models are required for simulations involving droplets/bubbles. These models typically define one or a few critical conditions, which are repeatedly tested during numerical iterations. When the conditions are met, the program updates the diameter, velocity, and number of droplets/bubbles accordingly. In other words, the Lagrangian approach ignores the breakup/coalescence process and only considers the outcomes of such a process. This highlights the significance of the breakup/collision models, as they significantly influence the accuracy of the numerical simulations.

Historically, extensive research has been devoted to the droplet breakup process. One reason for this trend is that most heat and mass transfer processes are influenced by the rate of liquid vaporization, which is strongly dependent on the liquid breakup process. The surface to volume ratio increases after breakup, and a high surface to volume ratio greatly promotes the heat and mass transfer process.

According to Lane [64] and Hinze [65], there are various mechanisms of breakup, and the outcomes of breakup are also diverse. Droplet breakup in air research is divided into two categories: steady acceleration and sudden exposure. Although the precise mechanism of secondary atomization is unknown, it is thought that the phenomenon can be described by the Weber number and the Ohnesorge number:

$$Oh = \frac{\mu_{drop}}{\sqrt{\rho_{air}\sigma_{drop}d_{drop}}} \tag{8}$$

Researchers have identified several breakup regimes based on the two critical numbers, sometimes just the Weber number. The droplet breakup process has been classified into three regimes by Reitz et al.: (1) bag breakup [66], (2) shear or boundary-layer stripping breakup [67], and (3) catastrophic breakup [68]. They do, however, cast serious doubt on the validity of shear or boundary-layer stripping breakup theories [69]. According to the previous two theories, the breakup is caused by either a boundary layer separation caused by gas shear at the liquid interface or the formation and breaking of capillary surface waves. Both theories suggest that the droplet Reynolds number is important in determining the rate of droplet breakup. Reitz and colleagues demonstrated experimentally that droplet breakup in this regime is primarily determined by the droplet Weber number rather than the droplet Reynolds number. They also proposed a better term for this regime: "sheet thinning and deformation" [69]. Regrettably, no critical Weber number values are given for each regime.

Various analytical models have been developed as a result of previous experimental observations. The Taylor Analogy Breakup (TAB) model is the most well-known and classic. Taylor's analogy between an oscillating and distorting droplet and a spring mass system serves as the foundation for the TAB model. By solving the differential equation for a damped and forced oscillator, the distortion and oscillation of the droplet can be obtained at any time. Energy conservation determines the size of the child droplets after breakup, and the velocity direction of the child droplets is set to be perpendicular to that of the parent droplet. More information on the derivation can be found elsewhere [70, 71]. The TAB model is applicable to a wide range of engineering sprays where both spray velocity and Weber number are low. The WAVE model is more appropriate for applications where the Weber number is greater than 100. Reitz and Bracco [72, 73] proposed the WAVE model, which is recommended for high-speed sprays. Reitz sees atomization as the injection of a series of "blobs" the size of the nozzle exit diameter. The breakup time and resulting droplet size are related to the jet stability analysis's fast-growing Kelvin-Helmholtz instability. This method can successfully predict breakup in a variety of regimes and has been widely used in engine fuel injection analysis [72, 74]. For numerical simulations, other breakup models are also available. Kelvin-Helmholtz Rayleigh-Taylor (KHRT) model [75, 76], Stochastic Secondary Droplet (SSD) model [77], Enhanced Taylor Analogy Breakup (ETAB) model [78], Droplet Deformation Breakup model [79], and Unified Spray Breakup (USB) model [80] are among these models. Further details can be found elsewhere [81].

### 2.1.5 Impingement heat transfer

Due of the substantial temperature variations on the surface of the solidified shell in secondary cooling zones, complicated phase transformations and residual stresses might occur within the slab. Rapid heat evacuation from the slab must be homogeneous to minimize cracking or distortion of the slab. Certain fundamental phenomena, such as atomization of water droplets through spray nozzles, impingement and heat transfer at the droplet wall, and water droplet evaporation during or after impingement heat transfer, have been identified by researchers over the past decades. The mechanisms of spray cooling during the continuous casting process are complex, however. Spray and impinging heat transfer are the two main subcategories of these issues. [83]. Heat transfer coefficient (HTC) measurements over slab surfaces as a metric for quantifying heat transfer rate [84-88] have been produced via several experimental approaches. As a transitional characteristic between spray cooling and solidification, HTC distribution is crucial. However, the HTC may also be considered a predictor of the solidification of liquid steel. HTC distribution gives a unique perspective on spray adjustment and slab quality control. Because the slab moves constantly, the average temperature is greater than 1000K, and the liquid steel inside the solid shell is dynamically hardening, it is almost difficult to detect HTC on its surface [83]. HTC is also a localized parameter whose value is affected by both spray characteristics and slab surface conditions, namely water flow rate, air pressure, standoff distance, nozzle to nozzle distance, and slab temperature [89]. As a consequence, a large number of trials are needed to produce correlations for various nozzle types under various operating situations.

Studies on the air mist cooling process above the Leidenfrost temperature to determine the heat transfer coefficient are numerous [90-94], but they are typically inapplicable to cooling settings that vary from the experimental conditions. According to a certain class of heat transfer coefficient models, the heat transfer coefficient is related to water flux w (L min$^{-1}$ m$^{-2}$), droplet diameter d (m), and jet velocity v. (m s$^{-1}$),

$$h = f(d, v)w^{b} \tag{9}$$

although it was reported in [91,92] that the jet velocity has little effect on spray cooling heat transfer. To measure the local heat flux q under actual circumstances of air-mist cooling, an induction heating technique was devised, and the following formula was derived [57]:

$$-q = 0.307w^{0.319}u_{z,v}^{0.317}T_{w}^{0.144}d_{30}^{-0.036} \tag{10}$$

The author also developed a correlation to predict the heat transfer coefficient as:

$$h = 379.93w^{0.318}u_{z,v}^{0.330}T_{w}^{-0.895}d_{30}^{-0.024} \tag{11}$$

When the wall temperature Tw is between 723K and 1453K, which corresponds to the film boiling regime, it has been demonstrated that q increases with increasing drop velocity, water impact flux, slab surface temperature, and drop diameter, and that q decreases with decreasing drop diameter [95]. The impacting droplets of water spray will only come into touch with the surface for a brief amount of time during the film boiling regime; yet, the heat transfer that results are significant [12]. Convection in the layer of vapour beneath the droplet-surface contact is one of the heat transfer mechanisms that occur at the contact point between the two droplets. The heat transmission from the surface of the drops is accompanied by radiative heat transfer from the surface and convection heat transfer from flowing air on the surfaces. Because of the droplet-surface interactions, the heat transfer is also influenced by the material characteristics and roughness of the surface. For steel surfaces, it was discovered in a study [96] that the surface heat flux maintains within the range of 0.5MW/m$^2$ even when the film boiling regime is employed. The heat flux at the onset of transition boiling regime, i.e., at the minimal film boiling heat flux, was also reported in [97], and it was found to be in the range of 0.43MW/m$^2$ with a steel surface at 500ºC as an initial temperature. Heat transfer coefficient is strongly related to droplet diameter and initial collision velocity [98]. This indicates that the heat-transfer process and droplet-deformation behavior after impact are closely linked. According to consensus [98,99], the Weber number linked with the normal-collision velocity is the most accurate way to characterize the impact or deformation mode of the drops.

When air pressure is increased in the range of 200 to 400 kPa, it is hypothesized that the effect on heat extraction is due to the effect on the droplet size and velocity, with the hypothesis being that when compared to hydraulic nozzles, tiny droplets with high momentum are more suited to penetrate the vapor layer and reach the heated surface. However, the authors [100] claimed that when water impact flux increased, the influence of air pressure reduced, thus sprays and air-mists generated cooling effects that were equivalent; their study included water impact flux ranging from 0.68 to 2.72 L/m$^2$s and included sprays and air-mists produced cooling results that were similar. On the other hand, the researchers at [101] and [102] found that for a given water impact flow (in the range of 0.2 to 16 L/m$^2$s), the heat transfer coefficient increases as the air nozzle pressure increases. In their study, the scientists found that increasing the air flow rate to the water flow rate ratio results in finer and quicker droplets that contact the surface more quickly. It has been discovered in other studies [101,103-105] using air-mist nozzles that An increase in air pressure at a fixed water flow rate increases the boiling convection heat flux, although no connections between these parameters and heat transfer coefficient have been found. Because the experiments [91, 93, and 106] did not include a hot surface, the drop size and velocity used to interpret the heat transfer data were different in each study [91, 93, and 106]. A decrease in the volume (and number) of droplets with sufficient inertia was observed with an increase in water flow rate while maintaining constant air pressure. The diameter of the drops generated became larger and their velocities became smaller in general as the water flow rate increased at constant air pressureDrops with a median diameter of 100 to 200 µm were said to be optimum, and drop diameter was the second most important mist parameter on heat extraction after water impact flux [101]. The authors claimed that bigger droplets would only partly evaporate and leave a considerable percentage of liquid on the surface, but smaller drops would be unable to penetrate the vapor layer and reach the surface. They recommended a compromise between droplet diameter and droplet velocity in order to achieve efficient heat extraction on the surface. When it comes to heat transfer above leidenfrost temperature, that is, when it comes to within the film boiling regime, it was discovered in [103] that the parameter controlling heat transfer intensity was the kinetic energy of droplets, which was shown to be affected by air pressure. Furthermore, according to another study [94], heat transmission is regulated not only by water impact flow but also by droplet diameter and droplet velocity, all of which are major factors.

Since the introduction of the continuous casting process, various enhancements have been made to the secondary cooling area of the furnace. Using computational fluid dynamics (CFD) to build an accurate model that correlates varying nozzle settings with the heat transfer coefficient (HTC) over the surface of the slabs, the spray cooling control will be improved in the secondary cooling phase of the reactor. There are currently no models that can do this for air-mist spray cooling, and in order to obtain the correlation, the nozzles must be sent out for experimental testing, which can take several weeks to complete. If a model could produce the same results in a fraction of the time, this would be a huge breakthrough because it would reduce the amount of time spent waiting for the results and eliminate the need to outsource the testing of the nozzles.

Some critical characteristics, such as casting speed and standoff distance, are not included in the correlations presented thus far. Changing the casting speed can change the droplet residence time on the steel surface, resulting in an increase or decrease in the amount of energy transferred [107]. The speed of the heated surface influenced the flow of liquid on it as well as the creation of vapour in front and behind the impinging jet, according to a direct link between casting velocity and heat transfer coefficient proposed [14]. This allegation, however, was not backed up by evidence. Their conclusion was that the cooling intensity does not remain constant when the casting speed is changed. When CC is modelled for design or control purposes, they discovered that the velocity of motion of the cooled surface is still another variable that must be considered. Comparisons between steel and aluminum found that volumetric flux was enhanced when the orifice was closer to the surface (standoff distance) [108]. This has been shown to hasten the onset of the rapid cooling stages of the quench while also improving overall cooling efficacy. The investigation of the influence of nozzle-to-surface distance on heat transfer during spray cooling of brass and Inconel [109] revealed that as the nozzle-to-surface distance increases, the heat transfer coefficient decreases more slowly, with the rate of decrease being determined mostly by the water flux of the spraying system. Because of this, it is required to construct a more thorough and general HTC correlation in order to incorporate these events into the model.

One possibility is to use a numerical method to quantify HTC on the slab surface in a localized area. CFD has developed into a strong tool and has achieved widespread acceptance for its ability to solve complex fluid flow and heat transfer problems in a reasonable amount of time, thanks to the advancements in high-performance computing technology. Despite this, only a few good numerical models of spray cooling and solidification during secondary cooling have been recorded, owing to the intricate physical phenomena involved. Development of a complete numerical model that can be utilized to forecast spray pattern and associated heat transfer during the secondary cooling process is crucial [110].

## 2.2 Solidification of Steel

In CC, the solidification process involves a variety of different physical phenomena that must be regulated in order to manage the overall quality of the product. Two of the more prominent factors leading to decreased product quality would include particle inclusions – largely entailing slag, flux powder or argon gas – along the solidification front, and surface defects; such as oscillation marks and various surface cracks [111-113]. Although advances in technology have aided in reducing the impact of these factors during production, they remain a constant threat in CC. Aside from altering the material composition of the product or improving upon equipment or operating practices upstream of the caster, regulation of the heat transfer, as well as the introduction of impurities during the solidification process are the two principal contributors instigating these defects.

The most dominant physical phenomena on flow and HT is the MZ region which is the zone between the liquidus and solidus temperatures. Columnar solidified dendrites forming along the shell front brake off from cross flow and slow the flow in the MZ region. The slower and thicker moving molten steel consequently impacts the conductive and convective HT and therefore the shell growth. Carman and Kozeny introduced a MZ model which relates the microstructure of the dendrites with its larger impacts on flow and HT [114], [115]. Other works describe these complex phenomena in greater detail and can be found elsewhere [116-118]. Figure 2-3 clearly depicts a few of the many complex phenomena that occurs within the CC process.

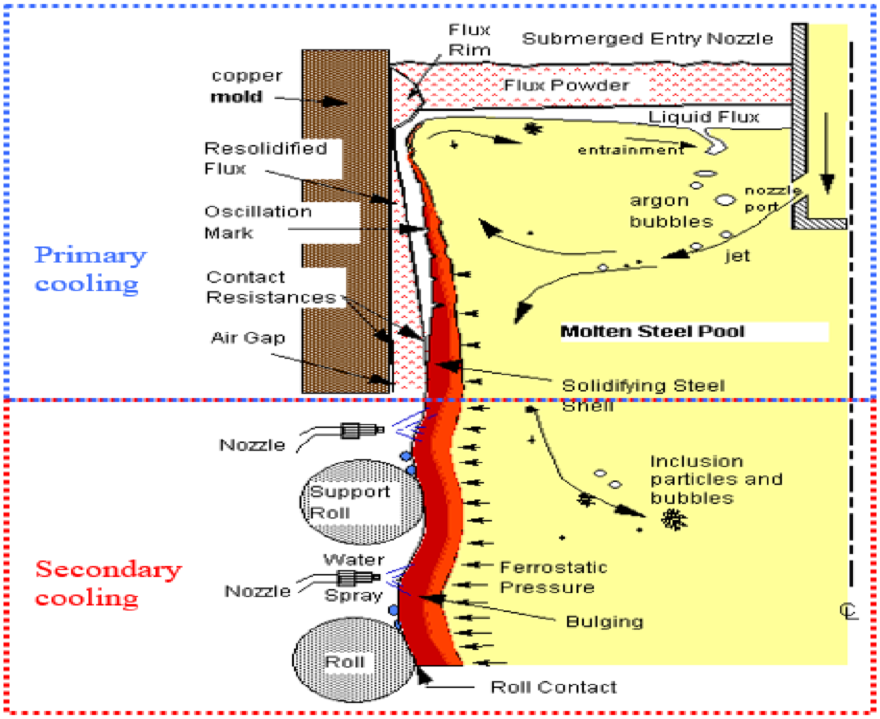

Figure 2-3. Primary and secondary cooling physical phenomena [118]

The hardened steel shell functions as a container for the leftover liquid as it is pulled from the mold by rollers mounted underneath the mold at casting speed [119]. An irregular and thin shell thick steel slab may create problems in manufacturing or shatter the caster's mold. Slab stability in the secondary zone below the mold is the primary goal of the secondary cooling. During the cooling process, spray nozzles and roll contact with the slab play a vital role. Defects and reheating may be reduced significantly by using this method of controlling the surface temperature. Secondary zone reheating may cause some cracks in the slab surface [120]. The slab surface may be reheated if the spray cooling zones are less than the melt core value [121]. Based on measurement on a breakout shell and the numerical simulations conducted by Professor Brain Thomas et al. the solidified shell can grow up to 20mm-25mm at the mold exit on both narrow face and broad face [122]. Once the semi-solidified slab enters secondary cooling section, liquid steel enclosed by the solid shell continues to lose heat and solidify due to the direct and intense spray cooling onto the slab surface. As a result, solid shell gradually grows from both narrow face and broad face towards its center throughout the whole secondary cooling process until it totally solidifies.

Direct observation and measurement of the solidification process is almost impossible due to the high casting temperature and the movement of the semi-liquid steel inside the solid shell. One exception for direct measurement of solid shell is when breakout occurs during the continuous casting. Once the molten steel bursts through the shell after the breakout occurs, the remaining hollow solidified shell can provide great insights onto the solidification process, such as the shell thickness at different locations, the oscillation mark depth and width, and inclusion entrainment [119].

Phase transitions and other microstructural changes impact the shell's strength and ductility as it travels between consecutive rolls in the spray zones after exiting the mold. Ferrostatic pressure, withdrawal, friction against rolls, bending and unbending, are all factors that contribute to the thermal strain on the part of the material. The shell deforms and creeps as a result of these complicated stress patterns. Crack development and propagation may result as a result of subsequent depressions in the strand's surface [14]. Lower in the caster, heat and solutal buoyancy effects, resulting by density variations between the various compositions formed by microsegregation, promote fluid flow. Macrosegregation and accompanying defects such as centerline porosity, cracks and undesirable property fluctuations are caused by this flow [123]. Creep at increased temperatures, coupled metallurgical embrittlement and thermal stress, make the steel shell susceptible to various deformation and fracture issues.

High-quality slabs can only be produced with precise and rigorous control of secondary cooling in continuous steel casting. Unless the temperature profile down the caster is tuned to reduce stress, such as unbending, during temperature regions of low ductility, defects such as transverse surface cracks might occur [125]. Cracking is exacerbated by rapid casting speeds and a narrow machine radius in thin-slab casters, where surface examination to identify faults is very difficult. Thus, there is a strong motivation to use control systems to improve spray cooling in order to achieve desirable temperature profiles.

Managing secondary cooling may be difficult. Emissivity changes from intermittent surface scaling and the harsh environment of the steam-filled spray chamber have made optical pyrometers unreliable in conventional feedback control systems [126]. [12]. The rapid pace of thin-slab casting necessitates a quick response from the operator. Modern air-mist cooling nozzles provide the potential benefits of quicker and more uniform cooling, but they pose the additional problem of air flow rate as another process variable to regulate.

Prior efforts to establish real-time dynamic control of cooling of continuous casters have been attempted. Spray-water flow should be regulated such that each section of the strand surface receives the same heat history. This has long been acknowledged. During and after transients, such as casting slowdowns during ladle exchanges, this is extremely critical and not usually apparent. optical pyrometers and other temperature sensors. Real-time model-based methods were suggested by both Okuno et al. [127] and Spitzer et al. [128] to monitor the temperature in horizontal slices across the strand to maintain the surface temperature at four to five fixed points. Every 20 seconds, computations were run, and feedback-control sensors were used to calibrate the system. Due to the inaccuracy of temperature sensors like optical pyrometers, these systems have proved troublesome in reality.

A method developed by Barozzi et al. [129] dynamically controls spray cooling and casting speed at the same time [130]. Because of the sluggish computer speed at the time, they had to rely on feedforward control to get the anticipated temperatures to match the set settings. Lally advocated employing fundamentally based computational models to optimize spray cooling in order to eliminate defects [130]. It was unable to implement online control at the time because of the poor computer speed and inefficient core models and control algorithms.

The steel is supported by rolls to prevent bulging owing to ferrostatic pressure. Diener [131] monitored the temperature of guide rollers in the secondary cooling zone of a slab continuous caster at various distances from the surface of the guide rollers without internal cooling. The cooling impact of the rollers was shown to be significant. Barber [132] used embedded thermocouples in the strand to detect the surface temperature of a slab [133]. The rollers' contribution to heat transmission in the secondary cooling zone was investigated.

# 3. METHODOLOGY

## 3.1 Air-mist spray cooling model

Because the densities and dynamic viscosities of the two fluids of concern, air and water, are 0.00123 and 0.0178, respectively, it is assumed that they are incompressible. For a variety of reasons, a four-step simulation technique was adopted. It is first necessary to create a simulation of internal flow in the nozzle, in order to accurately depict the mixing and turbulence phenomena that occur between air and water within the nozzle. The spraying system co. flat fan nozzle with a spray angle of 900 is employed in this simulation. For this reason, a very tiny cell size is chosen to capture the majority of the phenomena occurring between the point of jet exit from the nozzle and the impingement and cooling of the steel slab, which results in a very long computational time to run just once for the nozzle-to-surface distance. Furthermore, the VOF to DPM approach in ANYSYS Fluent was tested by running the entire spray domain at once and was found to be successful in converting the liquid phase into droplets; however, the number of droplets produced was very small and the computational time was too high, leading to the use of an alternative method of droplets size distribution (Nukiyama-Tanasawa) [134] to generate the droplets in STAR CCM+ CFD software to generate the droplets.

### 3.1.1 Model development

Illustration of the simulation approach and the most critical physics in the spray cooling process is shown in Figure 3-1. For modeling the development and breakup of jets [135-138], the Eulerian-Eulerian technique has gained popularity numerically. As a result of the tight interaction between the liquid jet and the surrounding air, this method can be time-consuming and mathematically complex. When the region of interest is located further downstream, many scholars have chosen for the Eulerian-Lagrangian technique as an alternative strategy. When the primary and secondary breakups are ignored, the initial spray characteristics are defined at the breakup length, at which point the liquid jet has entirely broken down into droplets [139]. Due to its lower processing cost when compared to the Eulerian-Eulerian technique, the Eulerian-Lagrangian method is used. The entrainment of air caused by the high-speed water spray is represented in the Eulerian frame, whereas water droplets are considered as discrete phases and tracked in the Lagrangian frame, respectively.

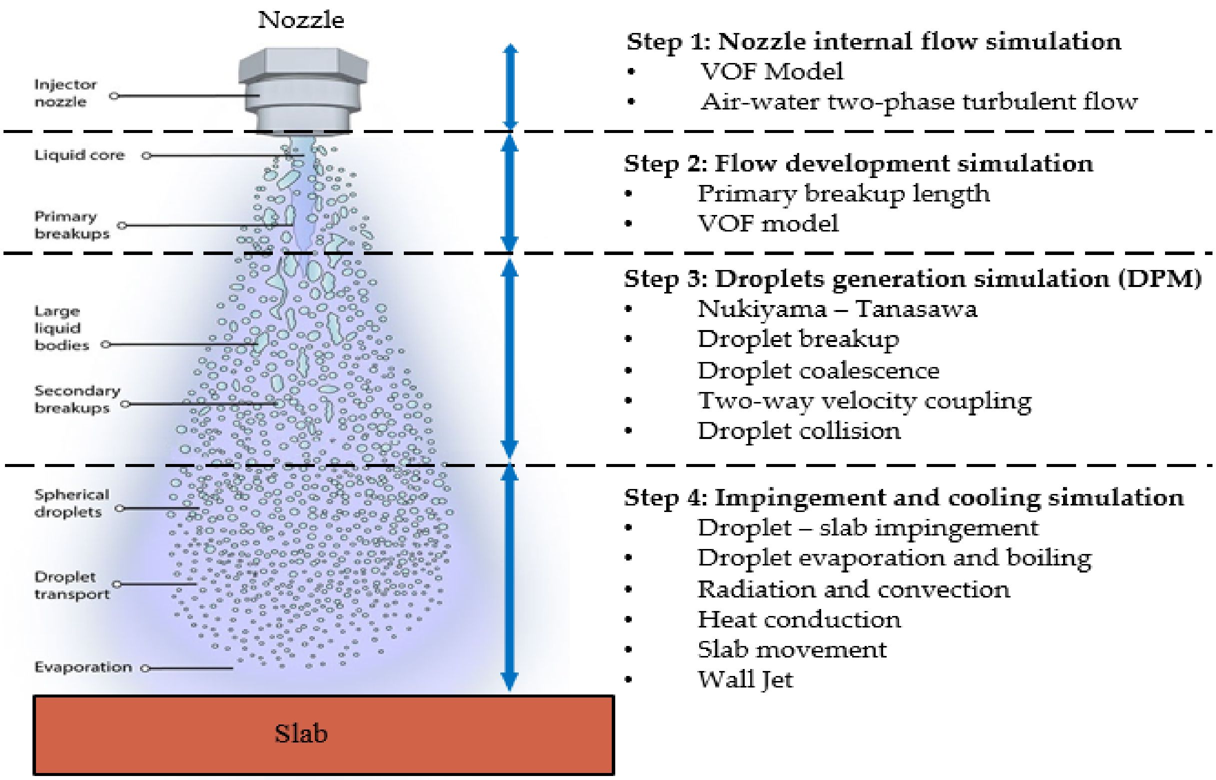

Figure 3-1. Simulation methodology, physics and CFD models of spray cooling [140]

### 3.1.2 Governing equations

***Continuous phase (air)***

The motion of the air phase was described in a Eulerian frame of reference according to the following equations.

Continuity equation:

$$\frac{\partial \rho_{air}}{\partial t} + \nabla.(\rho_{air} u_{air}) = 0 \tag{12}$$

where $\rho_{air}$ is the air density, and $u_{air}$ is the air velocity

Momentum equation:

$$\frac{\partial}{\partial t}(\rho_{air} u_{air}) + \nabla.(\rho_{air} u_{air}^2) = -\nabla P + \nabla(\mu_{air} \nabla. u_{air}) + \rho_{air} g + S_{air-drop} \tag{13}$$

where $S_{air-drop}$ is the source-term coupling the momentum of the air with that of the drops according to the following expression:

$$S_i = \frac{\pi}{6\rho v_{cell}} \sum \dot{\eta} \left( \rho_{drop}^{out} u_i^{out} \left( d_{drop}^{out} \right)^3 \right) - \rho_{drop}^{in} u_i^{in} \left( d_{drop}^{in} \right)^3 \quad (14)$$

The momentum transmitted between the air and the drops in a specific cell of the fixed Eulerian grid is equal to the change in the momentum of all the drops, g, passing through it throughout the Langrangian time-step, according to the particle source in cell model [141].

The majority of impinging jets used in industry produce turbulent flow as a result of the development of vortices along the sides of the jet, which is analogous to the Kelvin-Helmholtz instability. Accurately anticipating the presence of turbulence is extremely difficult, and it is not always possible. In accordance with the extensive comparisons made by [142], The Shear Stress Transport (SST) model by Menter [143] is one of the best turbulence models for forecasting impinging jet flow in terms of accuracy without needing a lot of computing power. The SST model combines the k–ω model near the wall, which requires a finely spaced mesh near the wall to generate accurate results, and the k–e model farther from the wall in order to take advantage of the strengths of each model in order to maximize the accuracy of the results.

***Multiphase flows:***

The numerical modeling of multiphase flows requires the exact characterization of interface dynamics, which permits flow regimes to be formed and related inter-phase transfer processes to be characterized. This is the foundation of numerical simulation of multiphase flows. Interpenetrating-continua technique, also known as the two-fluid method [144], is used to describe phenomena occurring at the interface between separating phases. Direct interface tracking methods, on the other hand, are used to directly mimic topology and dynamics of the interface [145]. (ITM). Each point in the mixture is occupied simultaneously (in variable proportions) by both phases in the averaged two-fluid formalism, therefore distinct conservation equations are required for each field in the formalism. For predicting specific kinds of multiphase flows, the volume of fluid (VOF) approach is one of the most often applied Eulerian-based ITMs [145-148], and it is shown to be effectiveThe liquid volume-fraction field, or the volumetric proportion filled by one of the phases inside volume V, is defined using the VOF technique. $F_{ij}$ is the traditional descriptor (in a discrete form) for this fluid feature, which is defined by:

$$F_{ij} = \frac{1}{v_{cell}} \int_{V} \chi(x, t) dV \quad (15)$$

where $\chi$ is a composition field. Eq. (7), therefore, represents the evolution of the liquid volume-fraction, identifying flow regions containing pure liquid (where $F_{ij} = 1$) from pure gas flow regions (where $F_{ij} = 0$). Interfacial cells are such that $0 < F_{ij} < 1$.

***Atomization***

To put it simply, atomization is the act of breaking up a continuous liquid into hundreds or thousands of droplets, resulting in an increase in the surface area of the liquid. Therefore, atomization improves the efficiency of all processes related with surface phenomena as a result of its effect on their efficiency. Physically, droplets are formed as a consequence of two separate breakup processes: the breaking up of the liquid sheet and the breaking up of the ligaments. The hydrodynamics inside the atomizer and the breakdown of the liquid sheet dictate this, which is traditionally represented by the size and velocity distributions of the droplets within the spray stream. Primary breakup refers to the first breakup processes, as opposed to secondary breakup, which occurs when the droplets generated as a consequence of the primary breakup process break up further into smaller droplets due to aerodynamic instabilities or droplet-droplet collisions (see Figure 1). It is well-known that the main split is a well-studied process, and the relevant hypotheses have been extensively tested in recent decades [73,149-152].

The liquid jet is vulnerable to numerous instabilities depending on the atomizer's operating flow parameters, such as capillary, helical, Kelvin–Helmholtz (KH) instability, and several processes of breakup of the liquid core and ligaments have been found in previous investigations. Some researchers conducted experimental studies and proposed empirical correlations to evaluate the primary breakup length for air-blast nozzles [39,40,44-46]. In this study, the breakup length was estimated as [39]

$$\frac{L}{D_l} = 0.66 \mathrm{We}_g^{-0.4} \mathrm{Re}_l^{0.6} \tag{16}$$

***Droplet coalescence and breakup***

The droplet coalescence model is based on the O'Rourke method [153], which involves stochastic collision estimation. The WAVE breakdown model is used to account for droplet breakup produced by the droplet's relative velocity to the surrounding air. The model presupposes that the breakup time and size of the subsequent offspring droplets are dictated by the fastest-growing Instability of Kelvin-Helmholtz:

$$\frac{dr_{parent}}{dt} = \frac{\Lambda\Omega(r_{parent} - r_{child})}{3.726 B_1 r_{parent}} \tag{17}$$

### *Droplet motion and convective heat transfer*

The Lagrangian method was used to model the motion of the drops. Their motion equation, which followed Newton's law, considered aerodynamic drag and gravity force and was expressed as follows:

$$\frac{du_{drop}}{dt} = \frac{3\mu_{drop} C_D Re_{drop}}{4\rho_{drop} d_{drop}^2}\left(u_{air} - u_{\ drop}\right) + \frac{g(\rho_{drop} - \rho_{air})}{\rho_{drop}} \tag{18}$$

The air-droplet interaction is represented by the drag force term, and the drag coefficient, $C_D$, can be calculated using the piecewise function in [154]. Other aerodynamic forces that may effect droplet motion were neglected since they are on the order of the gas-droplet density ratio, [144], which in this instance is $10^{-3}$. Furthermore, since the drops are not in a high-shear area of the flow field throughout the bulk of the flow field, the Saffman lift and Magnus forces were neglected; [144] this was justified because the motion of the drops in the neighborhood of the impact plane was not studied in the present paper. During the continuous phase iterations, droplet trajectories are estimated individually at regular intervals. The drops' trajectory was calculated using the following formula based on the change in their position-vector components over time:

$$\frac{dx_{drop}}{dt} = u_{drop} \tag{19}$$

Air-droplet interaction is modeled via the drag force term, which is added to the momentum equation of air as a source.

Droplet temperature changes during the spray cooling process are computed from the following energy balance equation of a droplet:

$$m_{drop} c_p \frac{dT_{drop}}{dt} = \pi d_{drop}^2 h\left(T_\infty - T_{drop}\right) + \frac{dm_{drop}}{dt} h_{fg} + \pi d_{drop}^2 \varepsilon_{drop} \sigma_{SB}\left(T_R^4 - T_{drop}^4\right) \tag{20}$$

The Ranz-Marshall model [155] may be used to calculate the convective heat transfer coefficient h. The concentration difference between the surface of the droplet and the airstream governs the rate of droplet vaporization, and the associated mass change rate of the droplet may be computed using the formula below:

$$\frac{\mathrm{dm_{drop}}}{\mathrm{dt}} = \pi \mathrm{d}_{\mathrm{drop}}^{2} \mathrm{k_c} (\mathrm{C_s} - \mathrm{C_\infty}) \tag{21}$$

The coefficient $kc$ in Eq. (6) can be obtained from the Sherwood number correlation with the similar form as Eq. (8):

$$Sh_{drop} = \frac{k_c d_{drop}}{D_{vapour}} = 2.0 + 0.6 Re_{drop}^{0.5} Sc^{0.33} \tag{22}$$

***Droplet-wall impingement model***

The wall jet model developed by Naber and Reitz [156] considers three different outcomes, namely stick, reflect, and wall jet, depending on the properties of each individual incoming droplet. In the stick mode, after impingement, the droplet remains in contact with the wall and continues to vaporize. The normal velocity component of a droplet is changed to the opposite sign in the reflect mode, while the magnitude of both the normal and tangential velocity components remains constant. The model treats the impingement of a continuous stream of closely spaced droplets as an inviscid liquid jet emitted from the stagnation point on the solid surface in the wall jet mode. The empirical function for the liquid jet with a height of H as a function of the angle at which the droplet exits the horizontal impingement is used in the analytical solution for an axisymmetric impingement:

$$\mathrm{H}(\Psi) = \mathrm{H}_\pi e^{\beta\left(1-\frac{\Psi}{\pi}\right)} \tag{23}$$

The probability that a droplet leaves the impingement point at an angle between $\Psi$ and $\Psi + \Delta\Psi$ is given by integrating the expression for ($\Psi$):

$$\Psi = -\frac{\pi}{\beta} \ln\left[1 - \mathrm{P}\left(1 - e^{-\beta}\right)\right] \tag{24}$$

The expression for $\beta$ is given as:

$$\sin(\emptyset) = \frac{e^{\beta}-1}{(e^{\beta}-1)\left(1+\left(\frac{\pi}{\beta}\right)^2\right)} \tag{25}$$

***Impingement heat transfer model***

Even though a droplet is expected to stay spherical throughout its existence, it may distort and remain in close touch with the solid surface after an impingement. Based on pure heat conduction, the amount of heat exchanged between the droplet and the solid shell can be calculated as:

$$\frac{\mathrm{d}}{\mathrm{dt}}\left(\mathrm{m_{drop} c_p T_{drop}}\right) = \frac{\mathrm{k_{drop} A_{cond}}}{\mathrm{s_{slab}}}\left(\mathrm{T_{slab}} - \mathrm{T_{drop}}\right) \tag{26}$$

The expression in [98] is used to calculate the effective droplet-wall contact area, Acond. Throughout the continuous casting process, the slab temperature is higher than the Leidenfrost temperature [157Droplet vaporization is used to forecast vaporization from discrete phase droplets. It begins when the droplet's temperature exceeds the vaporization temperature and continues until the droplet reaches the boiling point or the volatile portion of the droplet is entirely consumed. Given the high temperature of the slab, it is expected that the vaporization rates would be substantial, and therefore the influence of the evaporating material's convective flow from the droplet surface to the bulk gas phase becomes significant. To this effect, the convective/diffusion-controlled model of [158, 158] was used to model the droplet vaporization.

***Slab movement***

The moving reference frame and the stationary reference frame were utilized in the simulations to mimic the impact of the slab moving relative to the nozzle. For the air and droplets, the governing equations are solved with reference to the stationary reference frame, whereas the energy equation for a moving slab in the computational domain is defined as shown below:

$$\frac{\partial}{\partial t}\left(\rho_{steel}h_{steel}+\frac{\overline{|u|}_r^2\rho_{steel}}{2}\right)+\nabla.\left[\bar{u}_r\left(\rho_{steel}h_{steel}+\frac{\bar{u}_r^2\rho_{steel}}{2}\right)\right]=\nabla.\left[k_{steel}\nabla T+\bar{\bar{\tau}}\bar{u}_r\right] \quad (27)$$

The relative velocity, $\boldsymbol{\bar{u}_r}$ between the two reference frames is defined as:

$$\bar{u}_r=\bar{u}_{stationary}-\bar{u}_{moving} \quad (28)$$

### 3.1.3 Simulation approach

***Section 1 (Internal Flow in the Nozzle)***

In order to splat against the surface of a deflector, the water enters at an angle of 90 degrees with respect to the air flow. Splashes are further separated and accelerated as they travel along a mixing chamber toward the exit due to shear forces exerted by the air stream as they pass through it. In order to describe the internal flow in the nozzle, the VOF approach was employed since it has a conservative formulation and allows for the direct calculation of a solution without discontinuities [145,160]. It is utilized as a marker function in this method to determine how much secondary phase (liquid) is present. Because both phases have the same velocity field, the interface kinematic boundary condition is immediately satisfied. Through the use of a Dirac's delta function, the normal stress jump condition of surface tension is introduced as a source term into the momentum equation [160]. The CSF model has been used to simulate the surface tension's normal stress jump condition. In this study, surface tension is viewed as a three-dimensional continuous influence across the interface, rather than as a boundary condition at the interface.

Among the numerous schemes available in Fluent for face flow calculation in VOF, the Euler Implicit has been selected as the steady solution. It is important to note that this approach applies the same interpolation treatment to all cells, regardless of whether they contain one or multiple phases. The term gravitational force has been introduced as a new source term. It is possible to combine the Standard k-x formulation near the wall with a modified k-e model in the far field using the k- SST model [161]. In this case, the Reynolds numbers for the water entrance nozzle were computed as 14425, and the k- SST was used to calculate internal flow at both the inner and outer layers because it is more accurate and requires less computation time. Because of its approach, the model is valid throughout the near-wall zone as long as the mesh resolution is enough, and so no specific near-wall modeling is necessary, which saves time and money. The mathematical model was solved using the commercial CFD code Fluent V.2020.R1, which is available for purchase online. The SIMPLE method [162] was employed to handle the pressure–velocity coupling problem.

***Section 2 (Flow Development)***

This entails developing the flow outside the nozzle and determining the liquid's breakup length, or the point at which droplets begin to form: the primary breakup of the liquid jet near the atomizer outlet and the following secondary breakdown of the arbitrarily formed liquid ligaments, as well as the huge droplets created by the first breakup farther downstream. The initial phase of breakage occurs at the nozzle's tip. The cavitation bubbles created within the nozzle, in essence, induce primary breakup, pushing the liquid to shatter into ligaments and large droplets. Using the empirical correlation for air blast nozzle, the primary breakup length was estimated. In this case, the Reynolds and Weber numbers were calculated at a fixed reference point near the nozzle outlet tip, and the corresponding empirical correlation was used to calculate the breakup length. The VOF method was used to develop the flow from the nozzle outlet to the breakup length.

### *Section 3 (Droplets Generation)*

At the primary breakup point, droplets begin to form. The droplets travel away from the nozzle, and the gas-liquid interface becomes unstable due to the velocity difference at the shear layer of the liquid jet, to the point where viscous forces do not dampen the instabilities. Secondary breakup occurs when the instability overcomes the surface tension forces and disintegrates the liquid. The velocity profile at breakup length was extracted and used as one of the injection data for the droplet distribution to generate the droplets. The Nukiyama-Tanasawa (NT) droplet distribution method was used, and because it is not available in the ANSYS Fluent software, the STAR CCM+ software was used. The VOF – DPM approach in ANSYS Fluent used an explicit solver with a time step of 1 x10-5sec and 7.5 million cells in the mesh, resulting in a very long computation time of about sixty hours and yet could not produce sufficient droplets. The NT approach, on the other hand, used an implicit solver with a time step of 1x10-3sec and 0.25 million cells in the mesh to generate a large number of droplets in less than an hour for the same condition that was used in ANSYS Fluent. According to the STAR CCM+ manual, the method necessitates some parameters for the NT equation. The droplet sauter mean diameter was extracted from the nozzle catalogue for cool-cast nozzle [15] for each air pressure and water flow rate and was used to estimate the input for the NT equation described in the literature review section to generate the input data required for the droplet generation using the NT droplet distribution. The best fit was provided by alpha and beta values of 1.2 and 1.1, respectively. For the VOF-to-DPM transition model to be effective and produce accurate results, the cell size needs to be close to the droplet size which is in orders of microns. The cell size used was different for each case since the droplet sizes differ at different air pressure or water flow rate. Mesh sensitivity study was not conducted as no mesh would be ideal for all the cases. However, the mesh size was chosen based on the maximum droplet size from the droplets size data that was estimated using N-T equation. The cell size was such that the DPM volume fraction is less than 10%.

Spray cooling is accomplished through the use of a large number of droplets, each of which is traced using the Langrangian method. In the current study, the effect of turbulence modulation caused by interaction between spray drops and gas was modeled using the method described by [163]. The WAVE model was used for secondary droplet breakup because it is designed for high-speed injections with weber numbers greater than 100. In this case, mass is accumulated from the parent drop at a rate determined by break up time until the shed mass equals 5% of the initial parcel mass. At this point, a new parcel with a new radius is created. The new parcel has the same attributes as the original parcel, with the exception of radius and velocity. The momentum of the parent parcel is modified such that momentum is preserved, and the new parcel is given a velocity component chosen at random in the plane orthogonal to the parent parcel's direction vector. The magnitude of the new parcel's velocity is the same as that of the original parcel.

***Section 4 (impingement and cooling)***

The input parameter was air and droplet data from section 3's outlet. The overall heat transfer is explained in [12] as having three different components. The droplet impingement was simulated using the wall jet model, and the cooling of the steel slab was simulated using the boiling and evaporation model. The air jet is hypothesized to thin the liquid layer by shear forces, sweep away the vapor, and lower the vapor partial pressure above the liquid film, resulting in increased evaporation [88].

Using the section 3 results, an injection file was created. Fifty continuous phase iterations were performed between two discrete phase iterations prior to impingement, while 300 continuous phase iterations were performed between two discrete phase iterations following droplet impingement on the slab surface. The discrete phase was simulated with particle radiation interaction, two-way coupling, stochastic collision, coalescence, and breakup models. The software package used to run all the cases was ANSYS Fluent 2020R1, with each case taking approximately 48 hours to converge using 128 processors.

## 3.2 Solidification model

### 3.2.1 Simulation approach

The Eulerian Volume-Of-Fraction model is applied to the current study to simulate the phase change and convection inside the semi-solidified steel slab. The molten steel and the solid steel are treated as two immiscible continuous phases. One set of conservation equations governs the fluid flow in the molten steel region, the mushy zone region, and the solid region. The Reynold Average Navier Stokes (RANS) k-shear stress transport (k- SST) model is used to analyze turbulence in the flow model. This model combines the best aspects of both the normal k-model and the k-model. The k- SST uses blending functions to better address barriers like walls and baffles than the traditional k- model, and it also forecasts flows with separation and unfavorable pressure gradients better than the k- model [164].

The enthalpy-porosity approach, which uses a momentum source term based on a switching function to duplicate the effects of the MZ and solidified shell, is used to quantify flow resistance owing to solidification. The Metzner Slurry Viscosity Model's first zone governs low solid fraction locations and posits molten steel as the dominant phase of the solid-liquid combination, with the existence of tiny cemented crystals inside the melt responsible for increasing viscosity [114]. The Carman-Kozeny Mushy Zone (CKMZ) permeability model's second zone addresses viscosity abruptly, assuming that dendritic crystal formation progressing towards the melt is the source of increasing flow resistance [115].This work only utilizes the CKMZ model.

Among the existing volume-averaging methods, the mixture solidification model, also known as the Enthalpy-Porosity method, is the most popular model for continuous casing simulations and has produced meaningful results [165-167]. The Enthalpy-Porosity method was proposed by Voller et al. in 1985 [168] to resolve the “moving liquid-solid interface” issue and the “zero velocity in solid region” issue [168-172]. The Enthalpy-Porosity method is illustrated in Figure 3-2. In this volume fraction approach for solidification, one can see the 3 defined regions within the model for liquid, MZ, and solid.

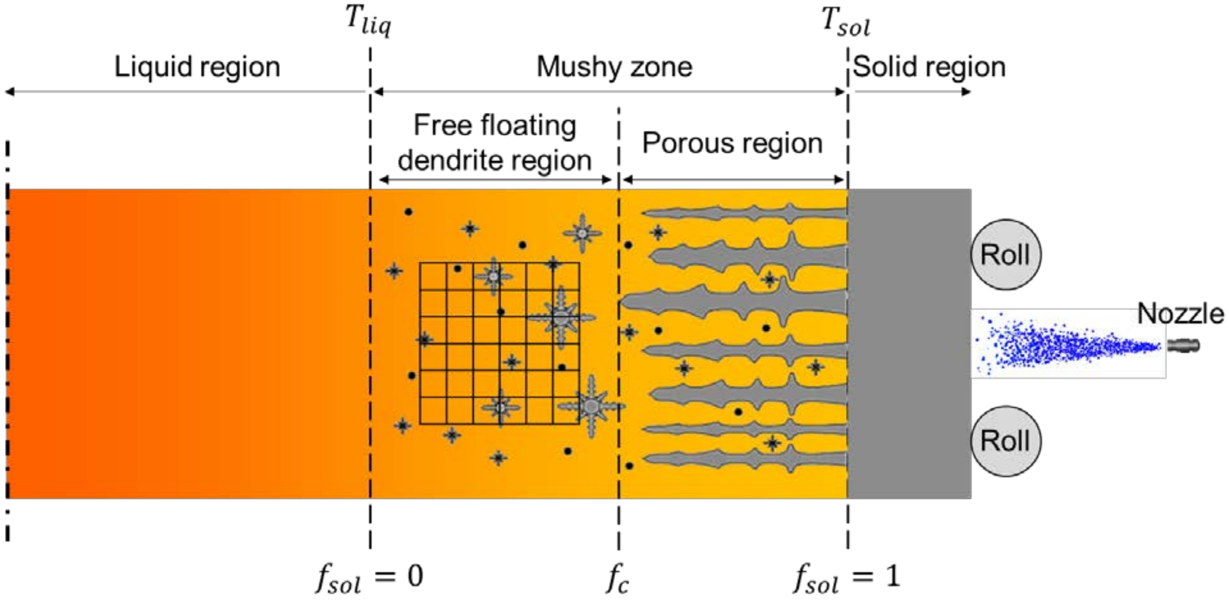

Figure 3-2. Enthalpy – Porosity method [173]

The relative solid volume fraction is used to calculate energy or enthalpy using a piecewise function. Depending on the location being simulated, the enthalpy will alter the HT characteristics (the solidified shell, MZ, or molten steel). The latent heat release is calculated on the cell basis. At each iteration, velocity and temperature of each cell centroid are solved (assume it is the finite volume method, other types of numerical methods need to derive their governing equations, but the concept still holds), and then the following step function is employed:

$$\mathrm{h_{lat}} = \begin{cases} \mathrm{L} & \mathrm{T_{liq}} \le \mathrm{T} \\ \mathrm{L(1 - f_{sol}} & \mathrm{T_{sol}} < \mathrm{T} < \mathrm{T_{liq}} \\ 0 & \mathrm{T} \le \mathrm{T_{sol}} \end{cases} \tag{29}$$

Where $L$ is the latent heat of fusion and $f_{sol}$ is the solid fraction in a control volume, which accounts for space in a cell occupied by dendrites. These two critical temperatures (the liquidus temperature $Tliq$ and the solidus temperature $Tsol$) divide the computational domain into three regions: pure liquid region ($Tliq<T$), pure solid region ($T<Tsol$) and the mushy region ($Tsol<T<Tliq$), as shown in Figure 1-29.

### 3.2.2 Governing equations

***Mass conservation***

The equation for conservation of mass of an incompressible and isotropic Newtonian fluid can be written as follows:

$$\frac{\partial \mathrm{\rho_{steel}}}{\partial \mathrm{t}} + \nabla \cdot (\mathrm{\rho_{steel}} \vec{\mathrm{u}}_{\mathrm{steel}}) = 0 \qquad (30)$$

Where$\rho_{steel}$ and $\vec{u}_{steel}$ are the density and velocity of the liquid and solid mixture, respectively.

***Momentum conservation***

Steel alloys solidify over a range of temperatures. The lower and upper boundaries of the temperature range are donated as solidus and liquidus temperature, respectively. A single momentum conservation equation is solved throughout the computational domain.

$$\frac{\partial}{\partial \mathrm{t}}(\mathrm{\rho_{steel}} \vec{\mathrm{u}}_{\mathrm{steel}}) + \nabla \cdot (\mathrm{\rho_{steel}} \vec{\mathrm{u}}_{\mathrm{steel}}) = -\nabla \mathrm{P} + \nabla\big[\mathrm{\mu_{eff}}(\nabla \vec{\mathrm{u}}_{\mathrm{steel}} + \nabla \vec{\mathrm{u}}_{\mathrm{steel}}^{\mathrm{T}}\big] + \mathrm{\rho_{steel}} \vec{\mathrm{g}} + \mathrm{S_{porous}} \quad (31)$$

Where $P$ is the pressure, $\mu eff$ is the effective viscosity, and it changes the liquid viscosity in the free-floating dendrite region, $S_{porous}$ is a momentum source term that takes effect in the porous region.

***Turbulence model***

The $k$-$\omega$ SST model is chosen for turbulence modeling due to its accuracy and computational efficiency and is given as

$$\frac{\partial}{\partial \mathrm{t}}(\mathrm{\rho_{steel}} \mathrm{k}) + \nabla \cdot (\mathrm{\rho_{steel}} \mathrm{k} \vec{\mathrm{u}}_{\mathrm{steel}}) = \nabla \cdot \left[\left(\mathrm{\mu_{eff}} + \frac{\mathrm{\mu_t}}{\mathrm{\sigma_k}}\right)\nabla \mathrm{k}\right] + \mathrm{G_k} - \mathrm{\rho_{steel}} \mathrm{\beta_k} \mathrm{k} \omega + \mathrm{S_k} \quad (32)$$

$$\frac{\partial}{\partial \mathrm{t}}(\mathrm{\rho_{steel}} \omega) + \nabla \cdot (\mathrm{\rho_{steel}} \omega \vec{\mathrm{u}}_{\mathrm{steel}}) = \nabla \cdot \left[\left(\mathrm{\mu_{eff}} + \frac{\mathrm{\mu_t}}{\mathrm{\sigma_\omega}}\right)\nabla \mathrm{k}\right] + \mathrm{G_\omega} - \mathrm{\rho_{steel}} \mathrm{\beta_\omega} \omega^2 + \mathrm{S_\omega} \quad (33)$$

Where $k$ is the turbulence kinetic energy, $\omega$ is the turbulence dissipation rate, $\mu_t$ is the turbulent viscosity, $G_k$ is the generation of turbulence kinetic energy due to mean velocity gradients, $\omega$ is the generation of turbulence dissipation rate, $\sigma_k$ and $\sigma_\omega$ are the turbulent Prandtl numbers. $\beta_k$ and $\beta_\omega$ are model coefficients while $S_k$ and $S_\omega$ source terms to account for the presence of the mushy zone.

***Energy conservation***

The Enthalpy-Porosity model applied in the current study does not track the liquid-solid interface explicitly. Instead, the model uses an enthalpy formulation to determine the solid distribution, which significantly reduces the computational time. The conservation of energy for both liquid and solid is written as follows:

$$\frac{\partial}{\partial \mathrm{t}}\left(\mathrm{f}_{\mathrm{liq}}\rho_{\mathrm{liq}}\mathrm{h}_{\mathrm{liq}}\right)+\nabla\cdot\left(\mathrm{f}_{\mathrm{liq}}\rho_{\mathrm{liq}}\mathrm{h}_{\mathrm{liq}}\vec{\mathrm{u}}_{\mathrm{liq}}\right)=\nabla\cdot\left(\mathrm{k}_{\mathrm{liq}}\nabla\mathrm{T}_{\mathrm{liq}}\right)-\mathrm{S}_{\mathrm{liq-sol}} \tag{34}$$

$$\frac{\partial}{\partial \mathrm{t}}(\mathrm{f}_{\mathrm{sol}}\rho_{\mathrm{sol}}\mathrm{h}_{\mathrm{sol}})+\nabla\cdot(\mathrm{f}_{\mathrm{sol}}\rho_{\mathrm{sol}}\mathrm{h}_{\mathrm{sol}}\vec{\mathrm{u}}_{\mathrm{sol}})=\nabla\cdot(\mathrm{k}_{\mathrm{sol}}\nabla\mathrm{T}_{\mathrm{sol}})-\mathrm{S}_{\mathrm{liq-sol}} \tag{35}$$

Where liquid and solid are denoted by the subscript $liq$ and $sol$, respectively. $\rho$ is the density, $h$ is the sensible enthalpy, $\vec{u}$ is the velocity, $k$ is the thermal conductivity, $T$ is the local temperature, $liq{-}sol$ is the energy exchange between liquid and solid. The liquid and solid fraction must satisfy the following constraint in each control volume:

$$\mathrm{f}_{\mathrm{liq}}+\mathrm{f}_{\mathrm{sol}}=1 \tag{36}$$

The liquid enthalpy shown in Eq. (185) is calculated by:

$$\mathrm{h}_{\mathrm{liq}}=\mathrm{h}_{\mathrm{sol}}+\mathrm{h}_{\mathrm{lat}} \tag{37}$$

# 4. COMPUTATIONAL DOMAIN AND BOUNDARY CONDITIONS

## 4.1 Air mist spray model

### 4.1.1 Nozzle internal region

The dimensions and detailed information of the internal geometry is not included in this article as they are proprietary information. Figure 4-1 shows the 3-D air-mist nozzle used in this study.

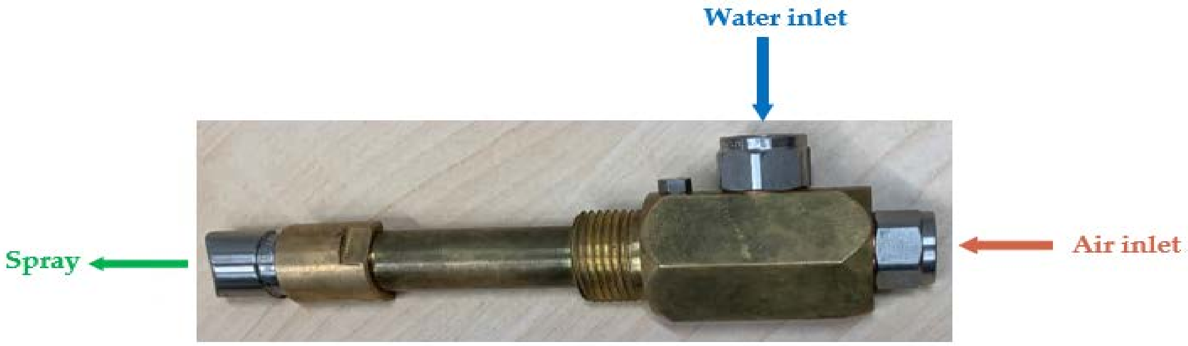

Figure 4-1. Air-mist nozzle

Figure 4-2. shows the polyhedral mesh of the spray nozzle used in this study. A base size of 1 mm, a total of 10 prism layers to capture flow characteristics close to the wall, a total thickness of 0.2 mm, and a transition layer ratio of 1.1 were used for the simulation. The water inlet was modeled as a mass flow inlet, the air inlet as a pressure inlet, the nozzle tip outlet as pressure at 1 atm, and the nozzle walls were subjected to a non-slip condition.

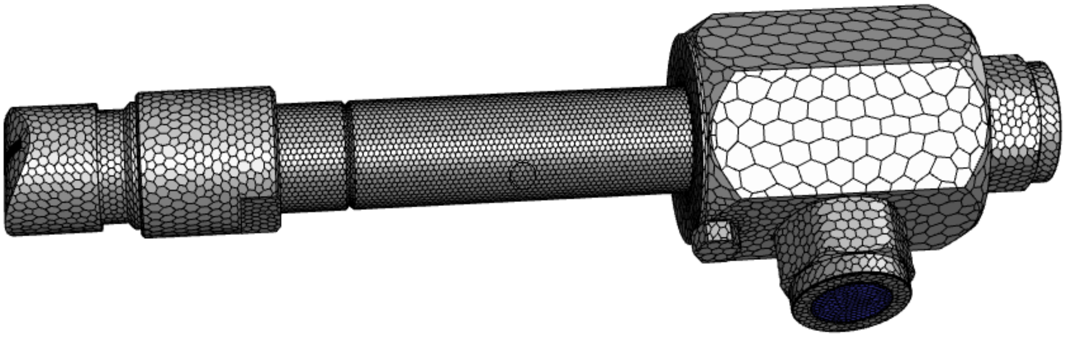

Figure 4-2. Nozzle meshing using Polyhedral mesh

Table 4-1 shows the casting parameters that were simulated to conduct a parametric study on the effects of air pressure, water flow rate, casting speed and standoff distance and to generate HTC correlation using these parameters.  A 65-case matrix was generated to represent 65 different continuous casting conditions. Pseudo automatic time step was used. Air was the primary phase while water was the secondary phase and implicit VOF disperse interface model were used. Air nozzle inlet was set as pressure inlet, and the nozzle tip exit was set as pressure outlet at 1 atm. Gas properties for the compressed air phase were calculated with respect to its gage pressure. Constant fluid and gas properties were used in the simulations and a surface tension of 0.0724 N/m was set. Water inlet was modeled as mass flow inlet, the air inlet was modelled as pressure inlet and a non-slip condition was imposed on the nozzle walls. The inlet temperature of water was maintained at 300K in all the conditions simulated.

Table 4-1. Casting parameters

| | |
|---|---|
| Air pressure (psi) | 30, 40, 45 |
| Water flow rate (gpm) | 2, 2.5, 3.7,4.5, 6.5 |
| Casting speed (inch/min) | 40,45, 46,49,50,60 |
| Standoff distance (inches) | 5.118, 6.7, 6.89, 8.5, 12, 23, 37, 44 |

### 4.1.2 Spray development

Two steps were introduced here. The first step was to validate the droplet size at 190mm domain height. The second step was to create an external nozzle flow with the potential core length as the domain height. The air-domain dimensions were calculated using distance measurements taken during the test [174] and the flat fan air-mist nozzle characteristics. Figure 4-3 depicts a polyhedral mesh with a refined potential core area and a cell size of 500 µm. The potential core length downstream of the nozzle tip is 20 mm. Wake refinement with 28-degree spray angle was used to achieve the refined area. The rest of cells size are 3 mm with growth factor of 1. The monitor plane is at 190mm to replicate the condition in the measurement for validation of the droplets size

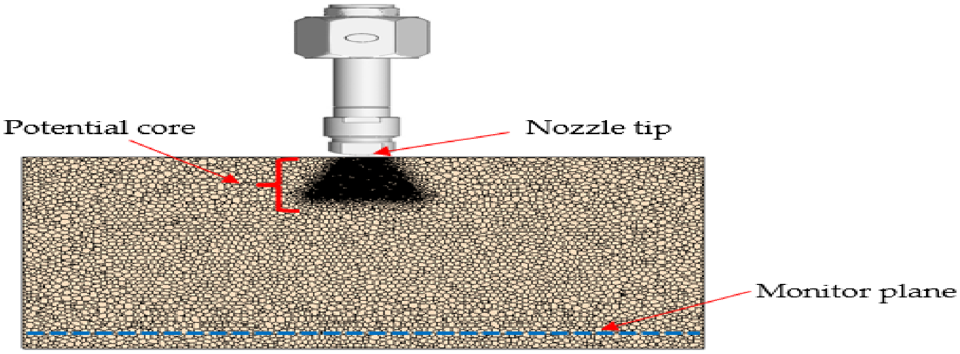

Figure 4-3. Polyhedral mesh for validation and spray development

Surface tension between water liquid and gases was set as 0.0724 N/m. Implicit, sharp interface, VOF-Compressive, for the volume fraction and SIMPLE scheme for the pressure-velocity coupling were used for the simulation using a time step of $1 \times 10^{-3}$ seconds. K-omega SST viscosity model was used. The velocity profile and the water volume fraction at the outlet tip of the nozzle in section was used as the inlet condition.

### 4.1.3 Droplets Generation

Figure 4-4 depicts a polyhedral mesh that has been refined at the top flat fan spray pattern. The domain height varies depending on the case because breakup lengths vary, but it is measured from the breakup length to 40mm above the slab. A 3mm cell size was used, with 5 prism layers.

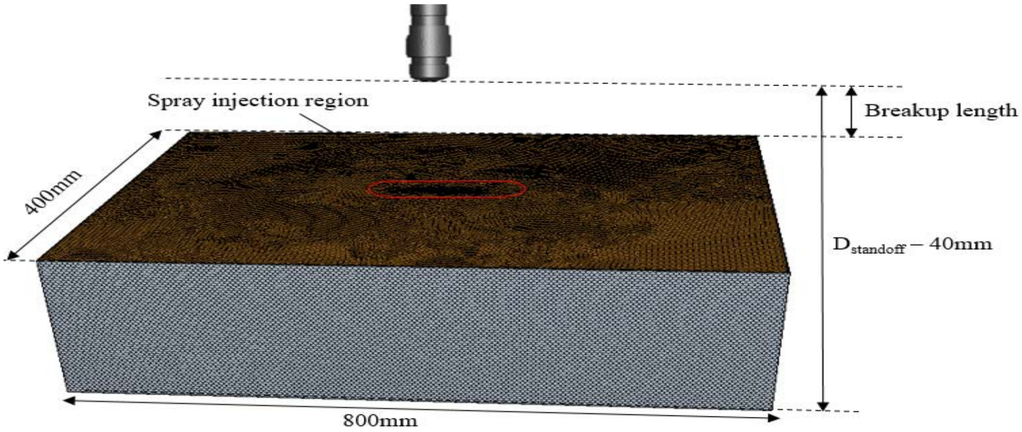

Figure 4-4. Computational mesh for droplets generation

At the injection surface, different cell sizes were used to refine the injection surface based on the maximum droplet size in each case. Eulerian – Lagrangian approach was used with air as the continuous phase and the water droplet as the Lagrangian phase. The NT method was used for the droplet size distribution. KHRT breakup model, turbulent dispersion, two-way coupling, pressure gradient and drag forces were used to simulate the Lagrangian phase. The simulation was run at steady state condition using SST (Menter) K-Omega viscosity model.

### 4.1.4 Impingement and Cooling

The computational mesh used in this section is depicted in Figure 4-5. The cell size was chosen so that the DPM volume fraction was less than 10%. As a result, in each case, the cell size is determined by the maximum droplet size. The slab is 800 x 400 x 30 inches in size (mm). In all instances, the spray domain height is 40mm.

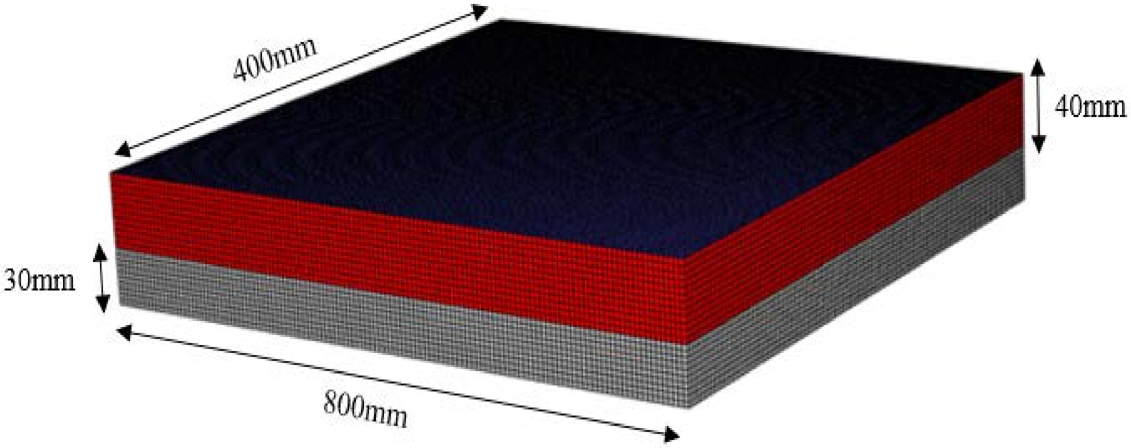

Figure 4-5. Structured mesh for the impingement and cooling

The slab is moving at the speed of casting. The velocity inlet was used for air, while the pressure outlet was used for the spray domain's sides. At the slab's bottom, a symmetry condition was used. The temperature on the upstream side of the moving slab in the casting direction was set to 1473K to represent the average temperature of the steel at the start of the secondary cooling zone. Because the temperature of the cells on the downstream side is unknown, the temperature of the cells on the downstream side is mapped to the surface using a user-defined function. The remaining slab sides are modeled as adiabatic because no heat loss is assumed. At 1473K, the steel properties were evaluated, and these, as well as the air properties, were set as constants. The k-SST viscous model, species transport, energy, and radiation models were all employed. Using the section 3 results, an injection file was created. Fifty continuous phase iterations were performed between two discrete phase iterations prior to impingement, while 500 continuous phase iterations were performed between two discrete phase iterations following droplet impingement on the slab surface. The discrete phase was simulated using particle radiation interaction, two-way coupling, stochastic collision, coalescence, and breakup models. ANSYS Fluent 2020R1 is the software package that was used to run all the cases.

## 4.2 Solidification model

Figure 4-6 illustrates the full thin slab caster used in the simulation. The full details of the caster are not shown since they are proprietary information. The length of the caster is too long such that running simulation with the full length would be computationally expensive so, the caster was sectioned into its segments and the simulation was done from one segment at a time to the next segment. In each segment, the top surface is assigned the velocity profile from the downstream of its preceding segment. A pressure outlet is used as the boundary condition in the downstream.

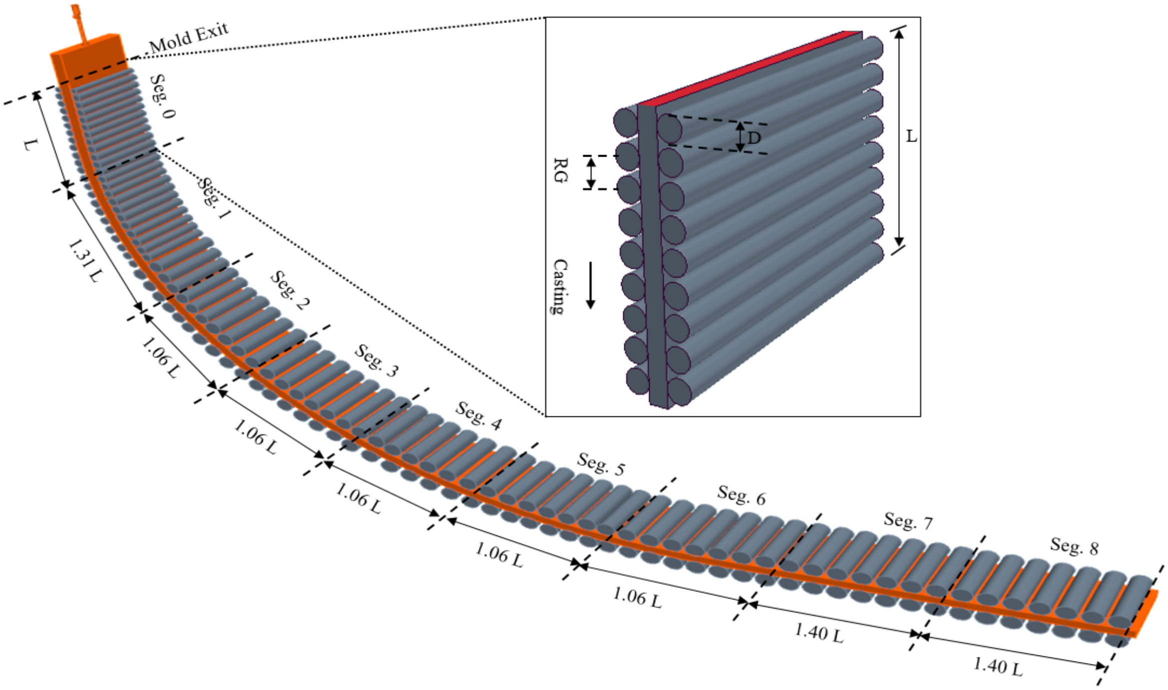

Figure 4-6. Whole caster geometry

Considering that the whole caster is a closed loop with no outlets in any segment, a small portion from the next segment is added to the domain of the segment under consideration to ensure that the pressure outlet boundary conditions do not affect the results. When the metallurgical length (point at which all of the liquid steel completely solidifies) was reached, the model was switched from solidification model to solid heat transfer model to further predict the surface temperature of the solidified steel. The continuous casting process is quite complex, and it exhibits a variety of physical characteristics that have been related. At first, the following assumptions were made:

- The first five segments of the caster were assumed to be vertical while the rest were assumed to be horizontal.
- The roller contact angle is 7°.
- A constant value of 450W/m$^2$-K was used as the spray HTC in the entire broad face.
- A constant convective HTC of 8.7 W/m$^2$-K was applied in the narrow face.
- The surrounding environment was assumed to be at room temperature.
- The dendrite arm spacing was assumed to be constant
- All the material properties apart from viscosity were assumed to be constant and were evaluated within the temperature range of the segment.

The steel grade used in this study is a low carbon steel with 0.2% carbon content, the superheat was 36°F and the casting speed was 40ipm. The solidification was used in the first few segments of the caster but upon reaching the metallurgical length, the model was switched from solidification model to solid heat transfer model. The effect of roll diameter and roll gap on the solidification of steel was investigated and the case setup is shown in Table 4-2. The first segment (segment 0) was used for this study.

Table 4-2. Case setup for the effect of roll diameter and roll gap

| | Case 1 | Case 2 |
|---|---|---|
| Roll diameter | D | 1.21 D |
| Roll gap | RG | 1.25 RG |
| Gap/diameter | 5.42 | 5.22 |
| No. of rolls | 9 | 7 |

## 4.3 Integration model

The physical processes were replicated in the integration model. Since the solidification process is sensitive to the thermal-mechanical properties of the molten steel, it is pertinent that the temperature dependent properties of the steel are used instead of the constant properties assumed earlier. The steel grade used in this study has 0.451% carbon content. HTC is a localized parameter and so the constant spray HTC assumed earlier was modified by extracting the HTC from the spray simulation and mapping it onto the corresponding region in the solidification simulation domain. Figure 4-7 illustrates the mapping of spray HTC onto the broad face of a segment.

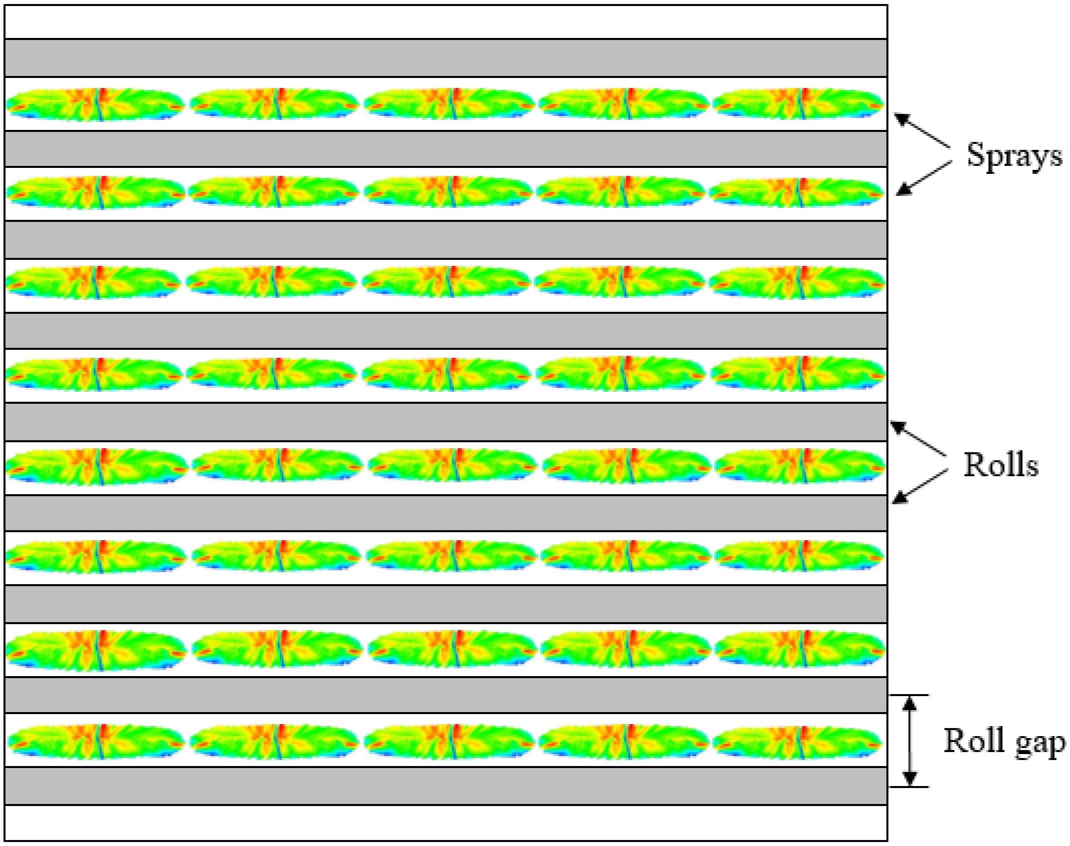

Figure 4-7. Spray HTC mapping unto the BF

The HTC result from a single spray simulation was replicated into five places in a row to replicate the five sprays in the real casting operation for this particular caster.

### 4.3.1 Obtaining Temperature Dependent Properties from JMAT-Pro

The material properties (MP) for the F&S model and thermal-mechanical model are obtained through the professional thermo-data software, JMAT-Pro. The software allows one to enter three inputs, alloy composition, cooling rate, and grain size, to obtain the constant and TDMP needed for the models. Unfortunately, only the steel composition is known so to obtain the other information, the slab surface temperature in **Error! Reference source not found.** was used to evaluate the cooling rate since the carbon investigated by the authors was of same grade as the steel in this report while the grain size was also evaluated. Figure 4-8 shows the two plots from [175] from which the cooling rate and grain size were evaluated.

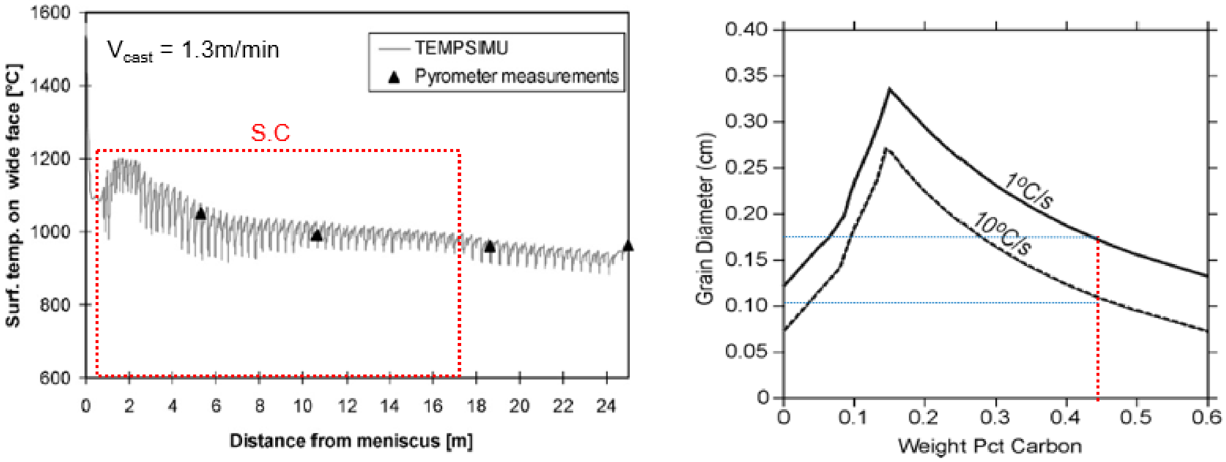

(a) (b)

Figure 4-8. Evaluation of cooling rate and grain size

To evaluate the cooling rate, the caster length in the study was mapped unto Figure 4-8(a) and the surface temperature difference within the length was calculated. This temperature difference within the caster length and the casting speed were used to evaluate the cooling rate. Since the information of the carbon content in this study is known and the cooling rate has been evaluated, they were used in Figure 4-8(b) to evaluate the grain diameter.

# 5. RESULTS AND DISCUSSION

## 5.1 Air mist spray model

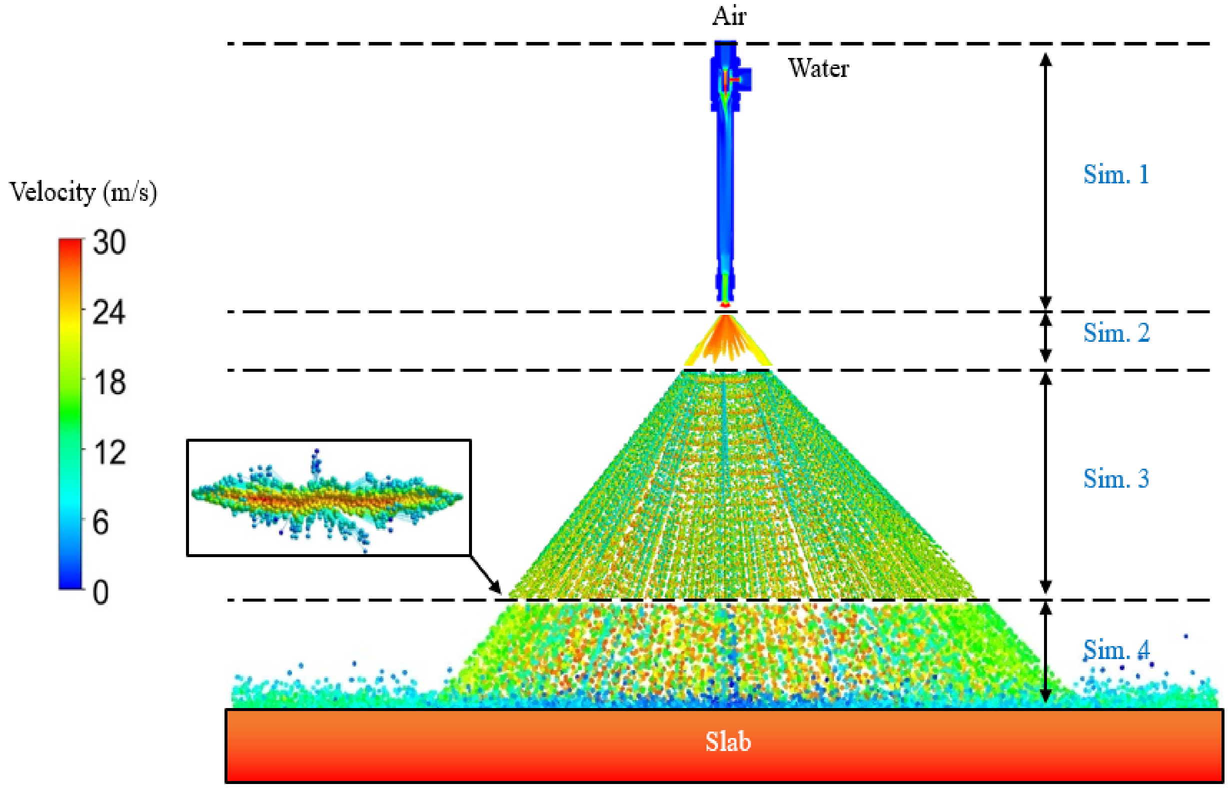

Figure 5-1 Overlap of the simulation results from each section

Figure 5-1 shows an overlapped result of the different step. It could be seen that flat fan shaped spray pattern was generated in the third step. Some results in each step would be shown to illustrate the air-mist spray features at different casting conditions. Considering that a lot of casting conditions were simulated to generate the HTC correlation, only few of the conditions would be shown to describe the effect of changing the casting conditions.

### 5.1.1 Flow in the nozzle

Figure 5-2 depicts the results for the velocity magnitude contour and water volume fraction of water in the nozzle. An increase in air pressure causes an increase in kinetic energy, as well as an increase in the aerodynamic interaction between air and water. The increased kinetic energy is infused into the velocity, reducing surface tension forces. As a result, the water volume is reduced and the velocity is increased. As a result, the air nozzle pressure conditions have a significant impact on the degree of atomization of the liquid inside the nozzle.

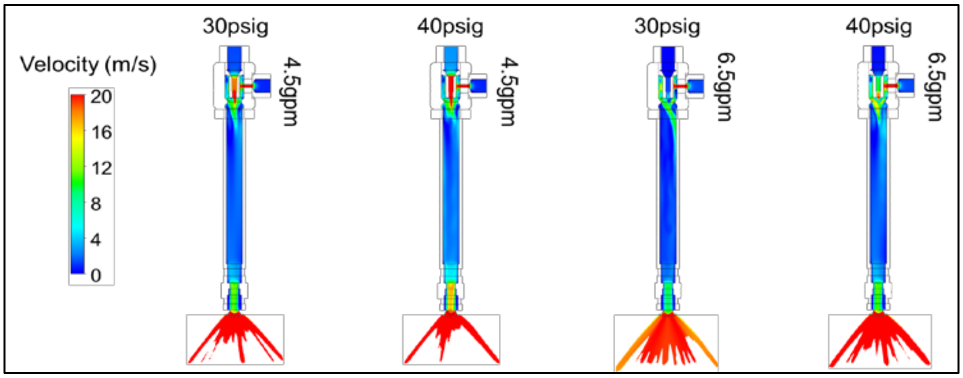

(a)

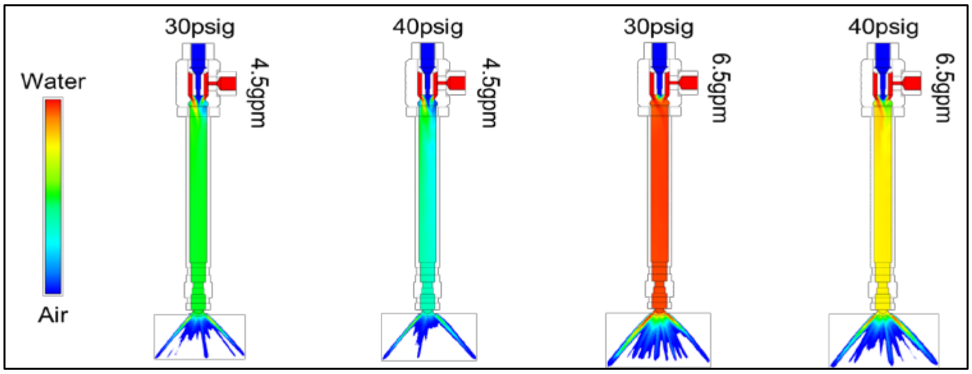

(b)

Figure 5-2. Cross section of nozzle showing (a) velocity magnitude (b) water VOF

When the flow rate of water increases, the volume fraction of water increases and the velocity decreases. This is due to the fact that as the flow rate of water increases, the concentration of water increases, as does the mass flux of water, resulting in an increase in frictional pressure gradient and thus a higher total pressure drop, resulting in lower velocity. The average results at the nozzle tip is shown in Table 5-1.

Table 5-1. Conditions at the nozzle tip

| Cases | Water Volume Fraction (avg.) | Avg. velocity (m/s) |
|---|---|---|
| 30psi air and 2gpm water | 0.251 | 26.468 |
| 40psi air and 2gpm water | 0.200 | 32.641 |
| 30psi air and 3.7gpm water | 0.578 | 19.978 |

### 5.1.2 Droplets formation and generation

Using the empirical correlation for air-blast nozzles [98], the flow properties at the nozzle tip were evaluated to estimate the breakup length. Table 5-2 summarizes some of the flow property results and the estimated breakup lengths.

Table 5-2. Spray properties at the nozzle tip and the breakup length

| Air pressure (psi) | Water flow rate (gpm) | Ave. weber number | Ave. Reynolds number | Breakup length (mm) |
|---|---|---|---|---|
| 30 | 2 | 76.079 | 1083.681 | 14.565 |
| 30 | 2.5 | 50.381 | 803.261 | 14.845 |
| 30 | 3.7 | 41.295 | 556.486 | 15.412 |
| 40 | 2 | 116.523 | 1372.402 | 13.866 |
| 40 | 2.5 | 73.316 | 828.161 | 13.013 |
| 40 | 3.7 | 50.725 | 782.182 | 13.399 |
| 45 | 2 | 139.986 | 1494.343 | 14.316 |

The average weber number and Reynolds number decreased as the water flow rate increased for the same air pressure, which can also be related to the decrease in velocity. The weber number and the Reynolds number are both directly proportional to velocity. As a result, the fluid is less unstable, and the breakup length is longer. When the air pressure was increased for the same water flow rate, the average weber number and Reynolds number increased, resulting in increased instabilities in the fluid and a shorter breakup length. This is consistent with [161]'s explanation that the shear layer causes flow instability at higher Reynolds numbers. As the weber number, which relates kinetic energy and surface tension, rises, the droplets gain more kinetic energy, which is much higher than the surface tension, causing greater instability and sheet breakup at shorter travel distances. Figure 5-3 shows the contour of velocity at the breakup up for all the cases.

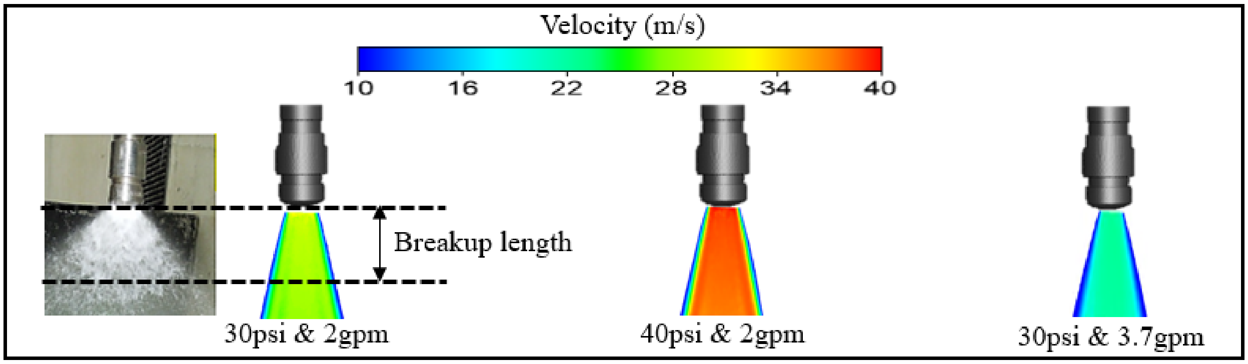

Figure 5-3. Velocity contour of the simulation conditions

### 5.1.3 Impingement and Cooling

Droplets fall and collide with the hot steel slab surface, eventually cooling it. Figure 5-4 depicts a typical cooling effect on the steel slab. Water is sprayed into the roll gap, which is the space between two successive rollers, during the casting process. The non-spray region of the slab, on the other hand, retains the spray cooling effect via convection and radiation. The spray and casting parameters influence the degree and uniformity of slab cooling.

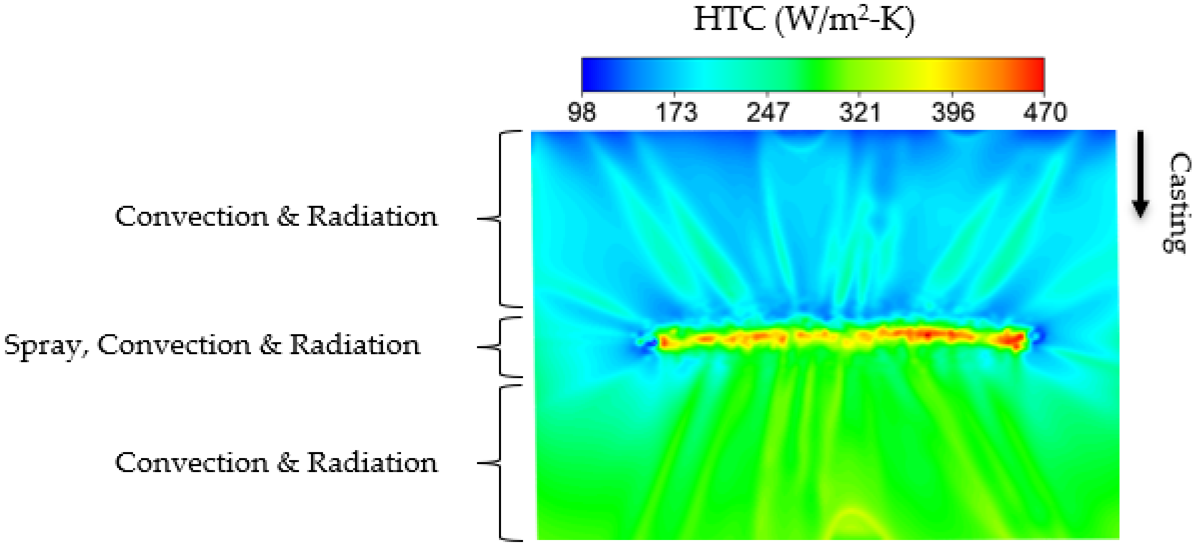

Figure 5-4. Cooling effect of the steel slab

Two cases at (30psi air pressure/2gpm water flow rate and 40psi air pressure/2gpm water flow rate) were used to analyze the particle Stokes and Reynolds number and is shown in Table 5-3.

Table 5-3. Average particle Stokes and Reynolds number

| | Є ($m^2/s^3$) | | η (m) | | St. | | Re | |
|---|---|---|---|---|---|---|---|---|
| | 30psi | 40psi | 30psi | 40psi | 30psi | 40psi | 30psi | 40psi |
| On slab | 643 | 761 | 4.69 x $10^{-5}$ | 4.50 x $10^{-5}$ | 8700 | 7205 | 5850 | 7082 |
| 10mm above slab | 59 | 56 | 8.64 x $10^{-5}$ | 8.61 x $10^{-5}$ | 444 | 482 | 1309 | 2189 |
| 30mm above slab | 42 | 16 | 9.42 x $10^{-5}$ | 1.17 x $10^{-4}$ | 578 | 360 | 1655 | 1413 |

According to numerous researchers [8,9,83,107,137,139,176], a typical two-phase gas-liquid atomization process is dominated by hydrodynamic or inertial force attributed to undulations/perturbation and inertial force attributed to drag/shearing effect, viscous force attributed to oppose a change in liquid geometry, and surface tension forces attributed to a minimal surface energy. Although particle inertia can be characterized by the stokes number, its significance in spray atomization and transport has not been reported in any literature. It can be seen that the droplets Stokes number as well as Reynolds number are very high. The values reported in [18,23,25,28,32] for monodisperse and bidisperse particles which had impact on particle inertia, dispersion, dissipation and preferential accumulation were less than 400 for Reynolds number and less than 10 for the Stokes number. Although particle inertia can be characterized by the Stokes number, the Weber number associated with the normal-collision velocity is the most accurate way to characterize the impact or deformation mode of the drops, according to consensus [98,99]

### 5.1.4 Parametric Studies

#### *Effect of air pressure on slab cooling*

Figure 5-5(a) shows the plots of the steel slab surface temperature. To visualize the effect of air pressure, the droplets velocity and diameter after impingement on the slab is shown in Figure 5-5(b) and (c) respectively. These plots were at a constant water flow rate of 2gpm and at 8.5 inches’ standoff distance. It is pertinent to state that droplets exhibit different behavior upon impingement as mentioned earlier.

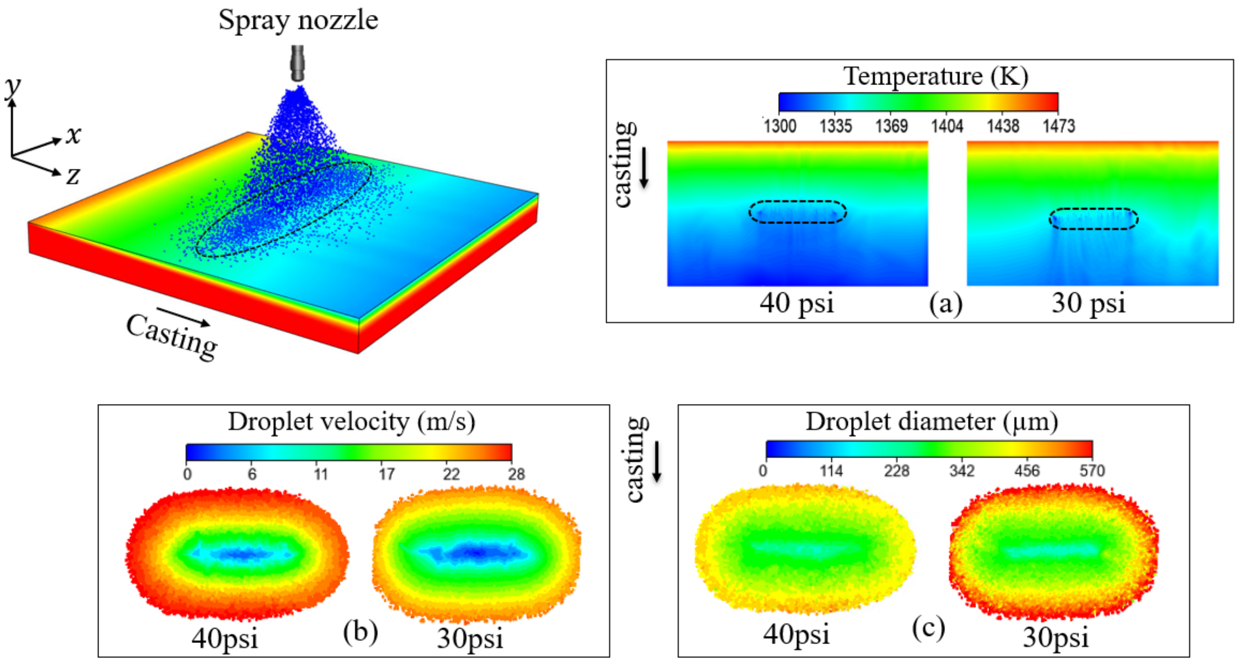

Figure 5-5. Slab surface contour of (a) temperature (b) droplets velocity (c) droplets diameter

A closer look at the droplet diameter showed the trend explained by [176] that finer drops usually occupy the jet center and coarser drops at the border possibly due to the intersections of the cross-wise streams of water and air at the entrance of the mixing chamber in this type of nozzle. It was further explained that this method of mixing cause some swirling in the drops produced with the consequent segregation of the larger ones at the periphery of the mixing chamber.

As discussed previously, the air-nozzle pressure conditions have a large effect on the degree of atomization of the liquid inside the nozzle such that fine droplets are produced. It was observed that the maximum droplet diameter on the steel slab decreased from 625μm to 521μm when the air pressure was increased from 30psi to 40psi which represents about 17% reduction in maxuimum droplet size. Although some percentages of the foggy drops are blown away by the free stream air or are evaporated before reaching the steel slab, very significant number of fine drops do reach the slab at high speed. As the small droplets have large surface area to volume ratio, they will extract more heat. The visualization done by [95] revealed that interactions of the droplets with the surface are more intense at higher air nozzle pressure which suggests that a very rapid evaporation must occur. An increase in air pressure from 30psi to 40psi resulted in an increase in HTC as there is higher heat removal. This is because the increase in air pressure increased the droplet velocity and reduced the droplet size thus, the droplets have higher momentum to penetrate the vapor layer formed above the slab surface due to leidenfrost effect and higher kinetic energy which is a key parameter governing the higher heat extraction above the leidenfrost temperature as opined by [103]. This effect agrees with the reports of [12,88,174,176]. Table 4 shows the averaged properties of the droplets on the steel slab.

Table 5-4. Average droplets properties on the slab at 2gpm water flow rate

| Droplets properties | Unit | 30psi air | 40psi air |
|---|---|---|---|
| Droplets coverage area | $m^2$ | 0.0623 | 0.0867 |
| Droplets weber number | - | 1522 | 1660 |
| Sauter mean diameter | µm | 439 | 381 |
| Droplets concentration | $Kg/m^3$ | 0.9854 | 0.4278 |
| Droplets volume fraction | - | $9.87 \times 10^{-4}$ | $4.29 \times 10^{-4}$ |
| Droplets Number density | $Number/m^3$ | 4.85 x 107 | 2.29 x 107 |

Evaluation of the droplets properties on the slab surface showed that the droplets concentration on the slab decreases at higher air pressure as smaller droplets produced by increasing the air pressure could be carried away by the entrained free stream air or could evaporate before reaching the slab. For the condition evaluated in Table 5-4, there was about 57% reduction in the droplets concentration on the slab when the air pressure was increased from 30psi to 40psi. The space covered by the impinging and reflected droplets has an elliptical shape and its area was calculated were it was seen that increasing the air pressure from 30psi to 40psi resulted in about 39% increase in the droplets coverage area on the steel slab. It was generally agreed in [98, 99, 156] that the one factor governing the impact and deformation mode of the drops is the ratio of the inertial to surface tension forces of the drops given by the weber number associated with the normal collision velocity of the drops. The results shown in Table 3 also supports that increasing the air pressure from 30psi to 40psi at a constant water flow rate of 2gpm increases the average droplets weber number on the steel slab by 9.1%. The droplets-to-droplets collision rate as well as the droplets number density, that is, the number of droplet particles per unit cell volume were found to both decrease as the air pressure increases. The uniformity of the spray cooling obtained by evaluating the standard deviation in the localized heat transfer coefficient showed that increase in air pressure results in more uniform cooling of the slab.

### *Effect of water flow rate*

Figure 5-6 shows the effect of water flow rate on slab cooling. Figure 5-6(a) shows the temperature contour of the slab after droplets impingement while Figure 5-6(b) shows the HTC contour of the spray coverage area on the slab.

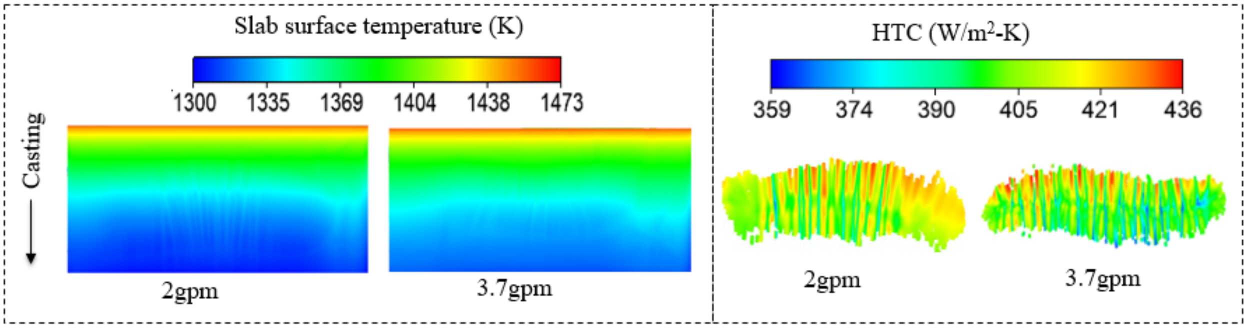

Figure 5-6. Effect of water flow rate on slab cooling

An increase in the water flow rate from 2gpm to 3.7 gpm results in lower cooling. As presented by [174], an increase in water flow rate at constant pressure imposes larger resistance on the air in the nozzle flow due to reduction in the cross-sectional area available for its flow and from the greater irreversible work it has to do for atomizing and accelerating an increasing amount of water. This result in ineffective atomization producing larger droplets size and lower velocity. This lower velocity limits the droplet – slab contact as the droplets momentum are lower and inadequate to penetrate the vapor layer above the slab surface. This is in tandem with the report in [12,174,176]. As reported by [177], increase in water flow rate at constant air pressure generally would decrease the spray cooling effectiveness because the droplets upon impinging the hot steel slab surface, do not evaporate effectively because of the hindrance by the liquid remains from the previous drops that also evaporated partially.

### *Effect of casting speed*

Two cases at constant air pressure of 40psi and water flow rate of 2gpm are shown in Figure 5-7 to illustrate the impact of casting speed on slab cooling. An increase in casting speed results in lower contact time between the slab and the droplets thus, lower cooling effect. The casting speed has negligible effect on the impinging and reflecting droplets velocity and sauter mean diameter on the slab. However, it was observed that the collision rate increases with casting speed resulting in relatively higher droplet number density on the slab. The discrete phase evaporation rate which measures the exchange of mass due to droplet-particle evaporation, was found to increase as the casting speed decreases.

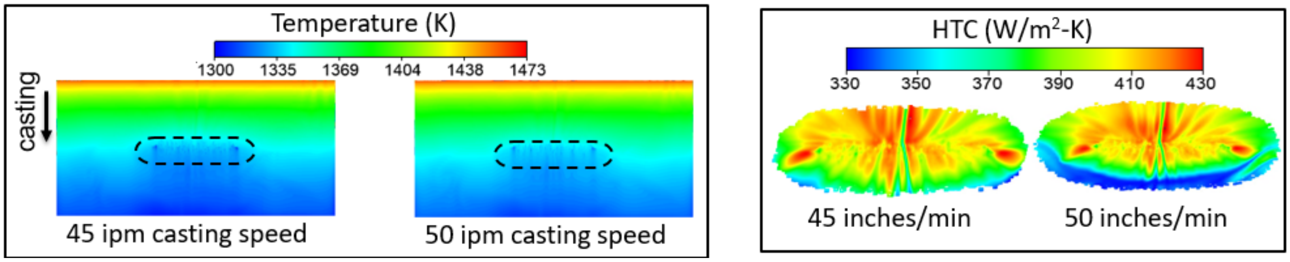

Figure 5-7. Effect of casting speed on slab cooling

***Effect of Standoff distance***

Figure 5-8 shows the contour of droplets velocity and the temperature at the steel slab surface at different spray standoff distance. As the standoff distance increases for the same air pressure and water flow rate, the spray area becomes wider as the higher travel distance enables more droplets collision and coalescence that could produce finer droplets but the droplets concentration decreases as more droplets are lost either by evaporation or are being carried away by the free stream air.

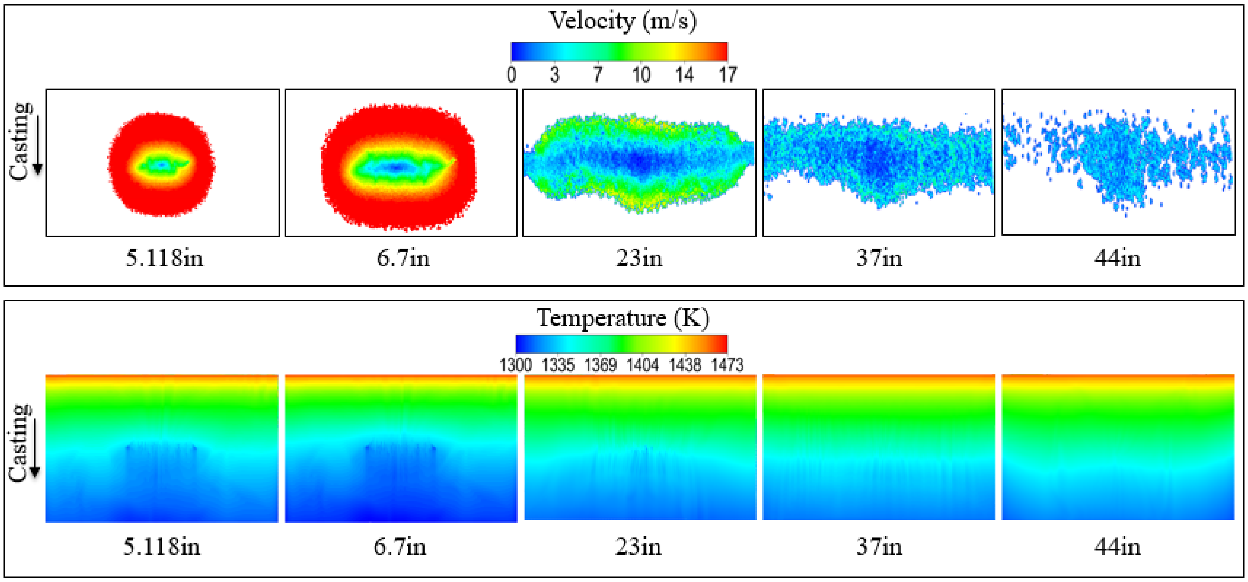

Figure 5-8. Effect of standoff distance

Also, with increase in the standoff distance, the droplets losses its kinetic energy and so the droplets velocity decreases resulting in lower cooling. However, an increase from 5.118” to 6.7” showed a better heat removal as the number of droplets and the spray coverage area increase with a very minimal decrease in droplets velocity but upon increasing the distance to 8.5”, the heat transfer coefficient decreased. It was also observed that as the standoff distance increases, the slab surface temperature difference decreases while the spray uniformity improves with the spray cooling having a standard deviation of 27.9K for the 5.118 inches standoff distance and 12.2K for the 44 inches standoff distance.

The essential standoff distance for each type of nozzle was discovered in an insightful investigation [178]. It's the absolute minimum standoff distance required for successful cooling, regardless of the water's mass flow rate. As long as the goal slab temperature is met, increasing the spray standoff distance within the critical standoff distance is encouraged. The total number of nozzles required for a continuous caster decreases as the spray cooling coverage below each nozzle grows, and a steel mill can save a significant amount of money on nozzles as a result. When a spray nozzle is put at a distance greater than the crucial standoff distance, however, the cooling effect is barely evident. Droplet size decreases considerably at a large spray standoff distance, according to the current study. If they can land on the slab surface, smaller droplets do assist spray cooling due to their high surface to volume ratio. To put it another way, droplets must avoid being whisked away by entrained air and maintain sufficient speed after breaking up to penetrate the vapor layer floating over the slab surface.

### 5.1.5 Heat Transfer Coefficient Correlation

HTC is a localized parameter whose value varies depending on the casting and transversal directions. HTC values were determined using the approach described in [107]. Either linear regression analysis or curve fitting can be used to determine the relationship between the characteristic HTC and the four operating parameters. However, the final form of the correlation should be mathematically simple; otherwise, it will take a long time to compute, causing the casting control to be delayed. The simplest correlation is to suppose that the typical HTC, or aggregated HTC, is an explicit linear function of the operational parameters [107]:

$$\mathrm{HTC_{lump}} = \mathrm{X_0} + \mathrm{X_1 P_{air}} + \mathrm{X_2 Q_{water}} + \mathrm{X_3 V_{casting}} + \mathrm{X_4 D_{standoff}} \qquad (38)$$

where $\mathrm{P_{air}}$ is air pressure (psi), $\mathrm{Q_{water}}$ is water flow rate (l/min), $\mathrm{V_{casting}}$ is casting speed (m/min) and $\mathrm{D_{standoff}}$ is the standoff distance (inches). The coefficients in Eq. 21 can be found through multivariable linear regression analysis. The final form of the multivariable linear regression-based correlation is shown as follows:

$$\mathrm{HTC_{lump}} = 430.794 + 0.713\mathrm{P_{air}} - 1.648\mathrm{Q_{water}} - 25.623\mathrm{V_{casting}} - 0.627\mathrm{D_{standoff}} \qquad (39)$$

Figure 5-9 shows the comparison between the CFD-predicted HTCs and the correlation-predicted HTCs. The multivariable linear correlation has an average error of 2.03%. the plot shows that the multivariable correlation is very accurate at predicting the CFD heat transfer coefficient. The correlation involves three basic mathematic operations, i.e., multiplication, addition and subtraction. Such features should allow fast prediction, thereby enabling real-time casting control. When spray characteristics change, the current numerical technique should considerably minimize the time it takes to build new correlations. Furthermore, the need for innovative steel products is growing at a fast pace. Spray cooling methods for various types of steel include varying nozzle types (hydraulic or air-mist), nozzle positioning, and spray intensity (spray flow rate and standoff distance). Fast novel cooling solutions can be developed using the current high-performance computer assisted numerical technique.

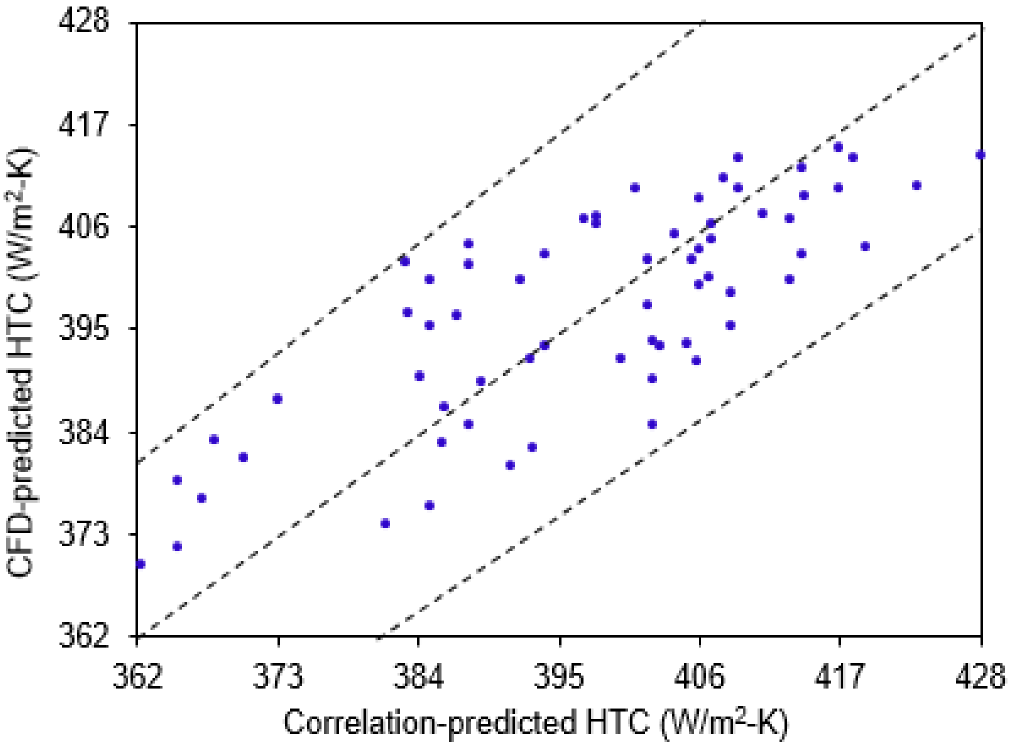

Figure 5-9. Parity plot of CFD and correlation-predicted HTC

## 5.2 Solidification of Steel

### 5.2.1 Effect of roll diameter and roll gap

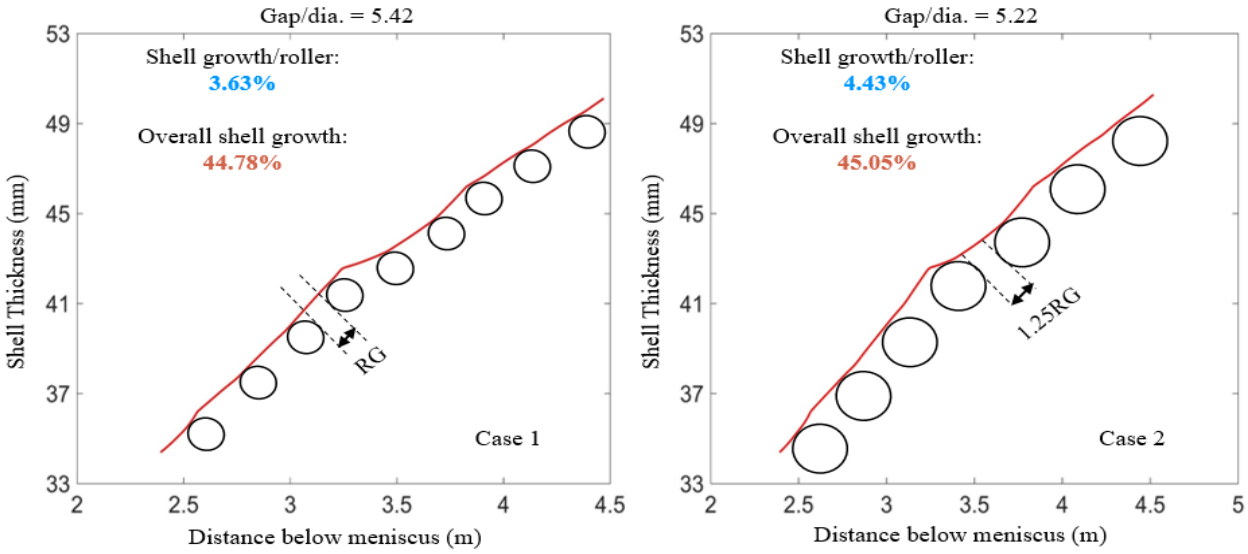

Figure 5-10. Effect of roll gap/roll diameter on shell growth

Figure 5-10 shows the effect of roll gap and roll diameter on shell growth in the first segment of the caster while their effect on slab surface temperature is shown in Figure 5-11. A ratio of the two parameters was used to make quantitative comparison since both parameters were changed at the same time. Increase in roll diameter increases the roller – slab contact area. Conduction is a function of surface area and so the increase in diameter results in higher heat transfer and the roller-slab contact also increases which further helps in extracting more heat from the slab surface thereby cooling it. This would result in increase in shell growth. However, increasing the roll diameter at a constant roll gap would reduce the area available for the spray cooling which accounts for 60% of the cooling during continuous casting.

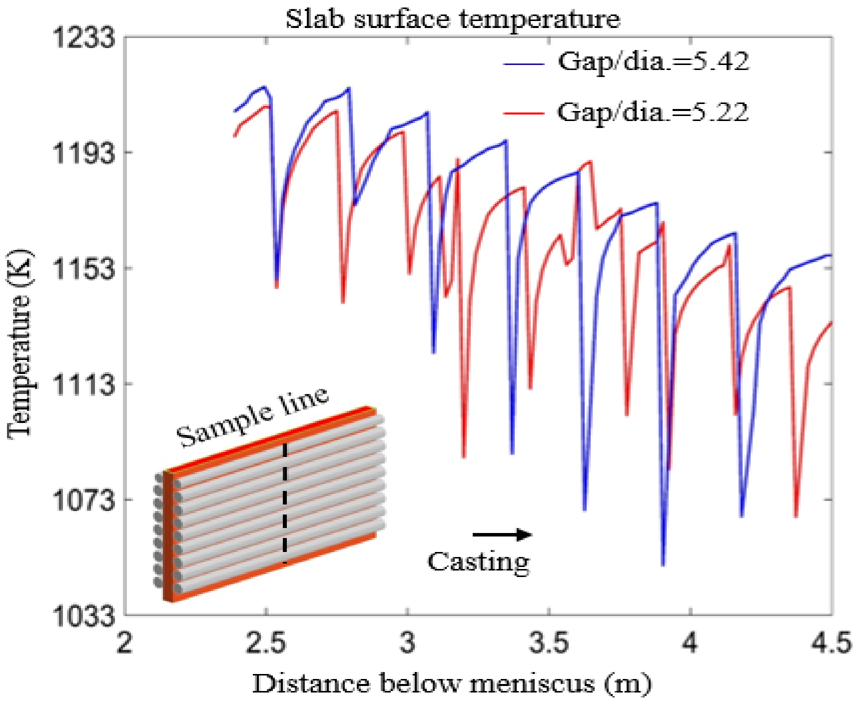

Figure 5-11. Effect of roll gap/roll diameter on surface temperature

The lengths between the temperature dips match to the distances between the rollers, indicating that the roller contact causes the temperature drops. The interactions between the rollers and the strand create the quick fall in temperature. When the temperature hits its lowest point, the contact is broken and the temperature begins to rise again. The larger the roll gap, the higher the heat removal from the slab and the shell growth. This is because an increase in roll gap increases the surface area for spray-slab contact and also results in increased radiation heat removal from the slab due to this increased surface area. However, increase in roll gap would lead to a decrease in the resistance to ferrostatic pressure as the rolls that help to provide this resistance are now further apart. This would result in defects such as bulging. It is therefore necessary to adjust the roll gap to roll diameter ratio to achieve efficient cooling of the slab without defect. The smaller this ratio, the higher the heat transfer and a sufficient resistance to ferrostatic pressure is maintained.

### 5.2.2 Effect of Superheat

Superheat is the difference between the solidification temperature and the pouring temperature of the metal. Figure 5-12 shows a plot of shell thickness and slab surface temperature in the first segment (segment 0) at two different superheats of 30°F and 40°F. It can be seen that increase in superheat from 30°F and 40°F results in a slight increase in surface temperature and a slight decrease in shell thickness. Superheat therefore has a very little significance in secondary cooling of steel.

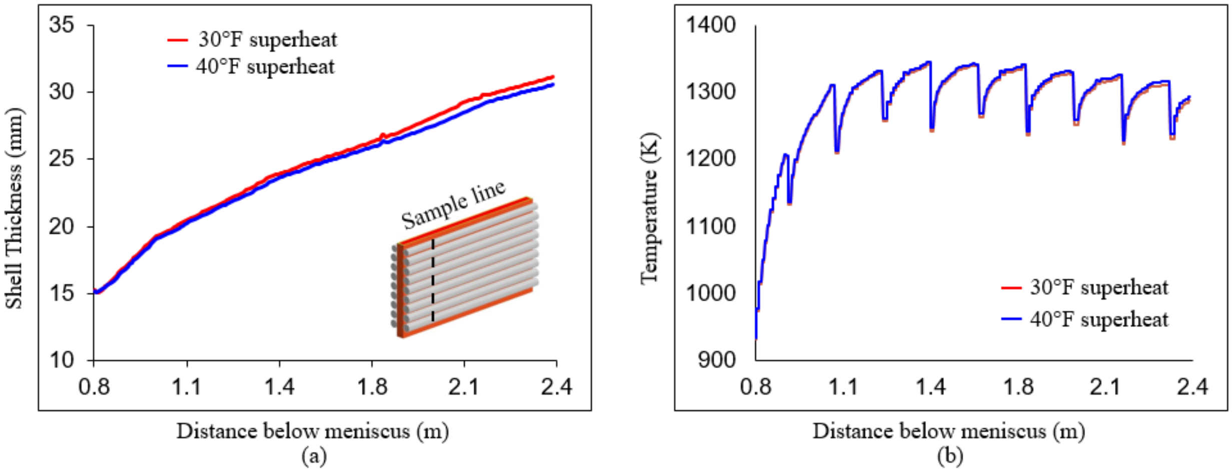

Figure 5-12. Effect of superheat

### 5.2.3 Effect of Casting Speed

Figure 5-13 shows a plot of shell thickness and slab surface temperature in the first segment (segment 0) at two different superheat of 40ipm and 49ipm respectively. It was stated in [179,180] that increasing the casting speed causes the growing depth of liquid pool and also increases the surface temperature of the slab. The result obtained in this study agrees with [179,180]. As the casting speed increases, the spray-slab and roller-slab contact time decreases resulting in lower shell growth as the shell thickness is thinned which could induce bleed out, bulging, inner cracks or other defects. This would equally result in higher metallurgical length. To ensure that the steel solidifies within desired range before reaching the end of the caster at higher casting speed, the spray flow rate has to be increased.

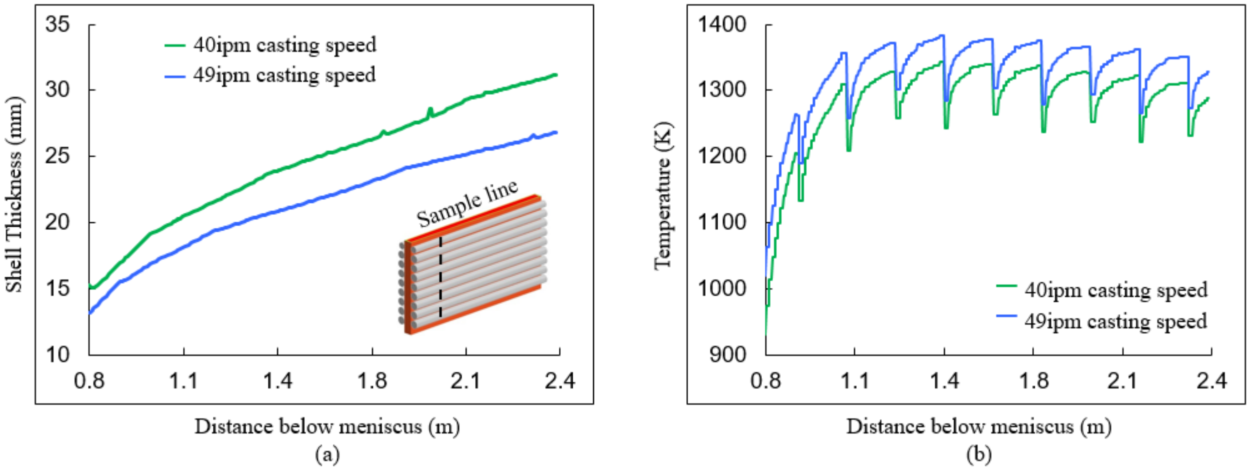

Figure 5-13. Effect of casting speed

### 5.2.4 Whole caster solidification

The shell growth from one segment to another along the caster is shown in Figure 5-14. The sample line of the plot is 0.72m away from the midpoint in the slab width direction. The sample point was chosen because it is in the lowest cooling region due to the recirculation of the steel in the mold. It was also the point used during the model development for the model validation.

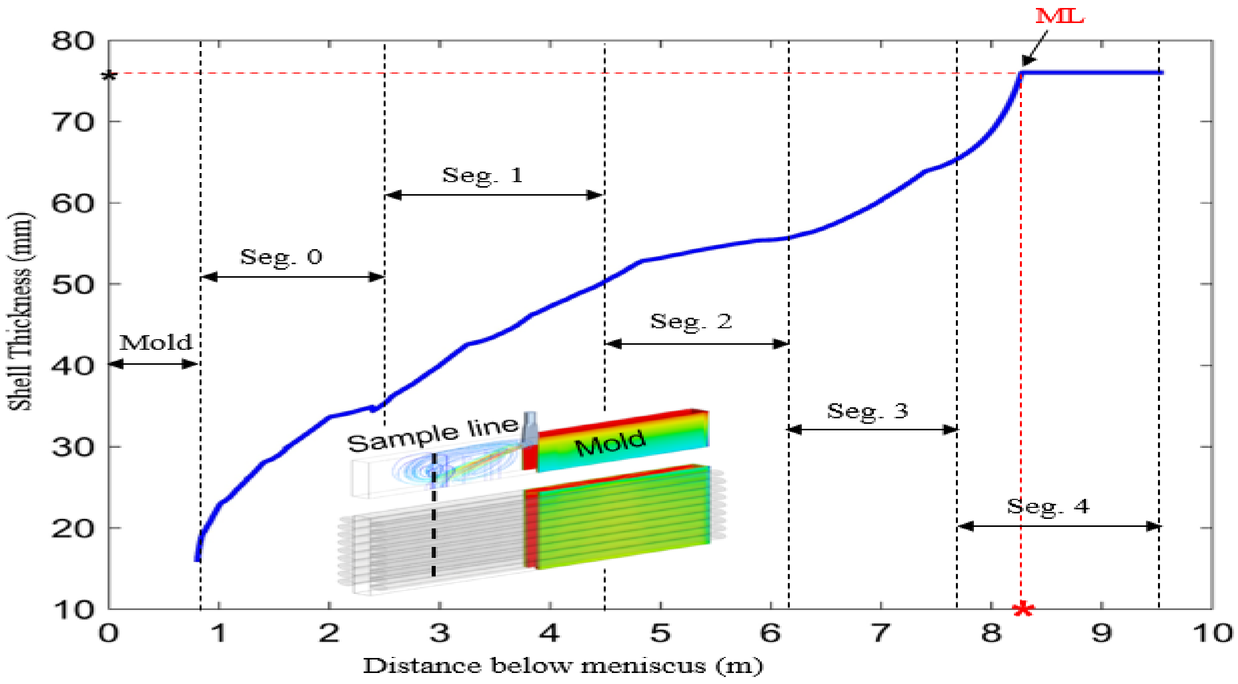

Figure 5-14. Shell growth and metallurgical length prediction

For the steel grade studied (0.2% C) the result showed that at a casting speed of 40ipm and superheat of 36°F, the molten steel completely loses its latent heat in the fifth segment (segment 4) and completely becomes solid. Thus, the metallurgical length was predicted as 8.27m. This was compared against plant data (8.54); the absolute difference was only 0.27m while the percentage difference was about 3.16%. Figure 5-15 shows the shell growth in each segment.

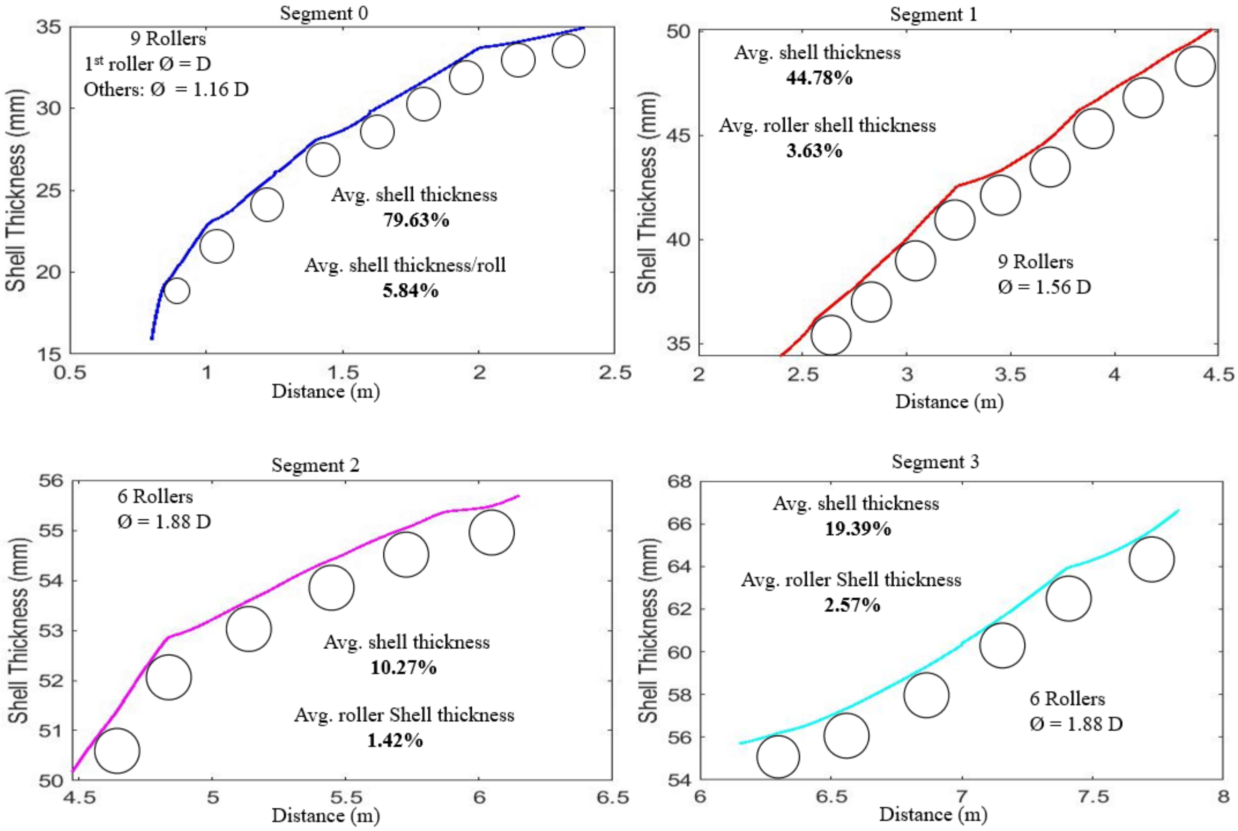

Figure 5-15. Shell growth in each segment

It is worthy of note that the roll diameter and roll gap in each segment of this caster is different. Again, the shell growth in a segment depends on its inlet condition. The heat removal is typically by the support rollers, the spray cooling water and by radiation. The shell growth is highest in the first segment and decreases down the caster. The higher the number of rolls, the higher the heat removal.

Figure 5-16 shows the slab temperature profile at the sample line. The sample line was made at the midpoint along the width of the slab. The slab centre and surface temperature from the mold exit down to the end of the caster is shown.

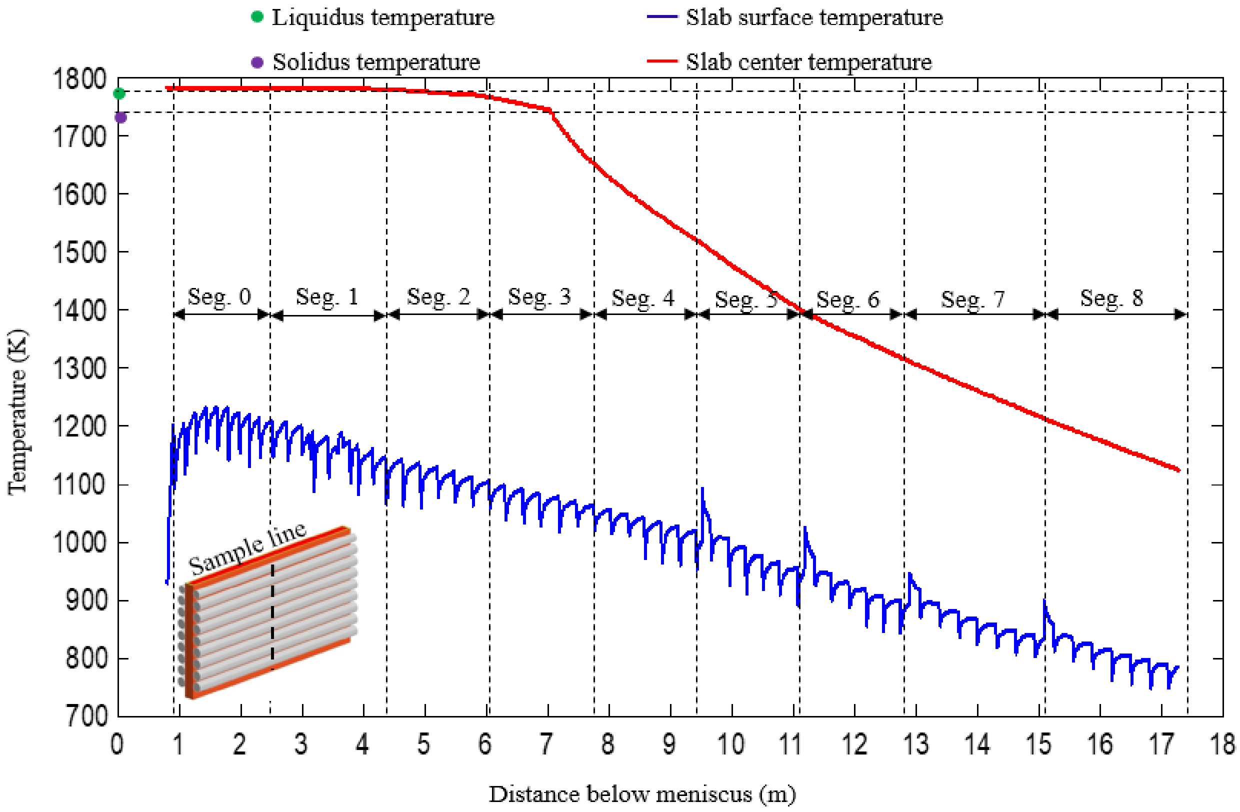

Figure 5-16. Slab temperature at the sample line

The solidus and liquidus temperature for this steel grade (0.2% Carbon) are 1745K and 1785K respectively. The surface cooling rate in each segment was evaluated and is shown in Table 5-5.

Table 5-5. Slab surface cooling rate

| Segment | Cooling rate (°C/s) |
|---|---|
| 0 | 3.246 |
| 1 | 1.159 |
| 2 | 0.841 |
| 3 | 0.780 |
| 4 | 1.077 |
| 5 | 1.993 |
| 6 | 1.798 |
| 7 | 1.090 |
| 8 | 1.177 |
| Full caster | 0.497 |

The results show that the cooling rate of the steel decreases down the caster as the steel solidifies. However, the cooling rate increased when the steel reached the metallurgical length (8.27m).

## 5.3 Integration of Spray and Solidification model

### 5.3.1 Material Properties

As mentioned earlier, the whole caster solidification methodology was modified to account for the localized HTC and the temperature dependent material properties. Table 5-6 shows the parameters evaluated and used to generate the material properties of steel as well as the important solidification temperature for the steel grade evaluated using JMatPro.

Table 5-6. Evaluated JMatPro input data

| | |
|---|---|
| Steel grade (% Carbon) | 0.451 |
| Cooling rate (°C/s) | 0.37 |
| Grain size (cm) | 0.192 |
| Superheat (°F) | 32 |
| Casting speed (ipm) | 40 |
| $T_{solidus}$ (K) | 1695 |
| $T_{liquidus}$ (K) | 1765 |

Comparing the steel grade (0.451% C) with the one simulated earlier (0.2% C), one could see that as the carbon content increases (higher steel grade), the liquidus and the solidus temperatures decreases. The viscosity was also seen to decrease with an increase in the steel grade. Figure 5-17 shows the material properties evaluated for the steel grade having 0.451% C.

It can be seen that the steel properties change with temperature. Within the casting temperature in secondary cooling (>1000K), all the properties except specific heat has a strong dependence on temperature. So the specific heat was maintained as a constant while the other properties were set as temperature dependent.

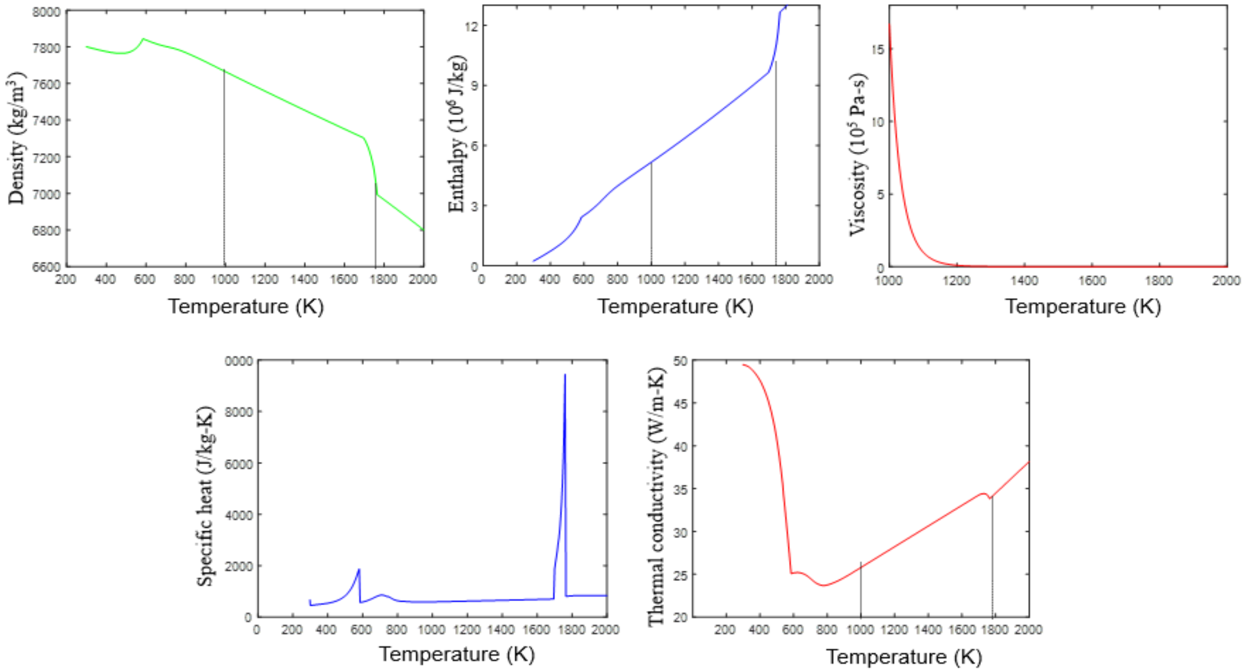

Figure 5-17. Material properties plots

### 5.3.2 Slab temperature along the caster

Figure 5-18 shows the predicted surface and centre temperature of the slab. The result follows similar analysis above for steel with 0.2% carbon.

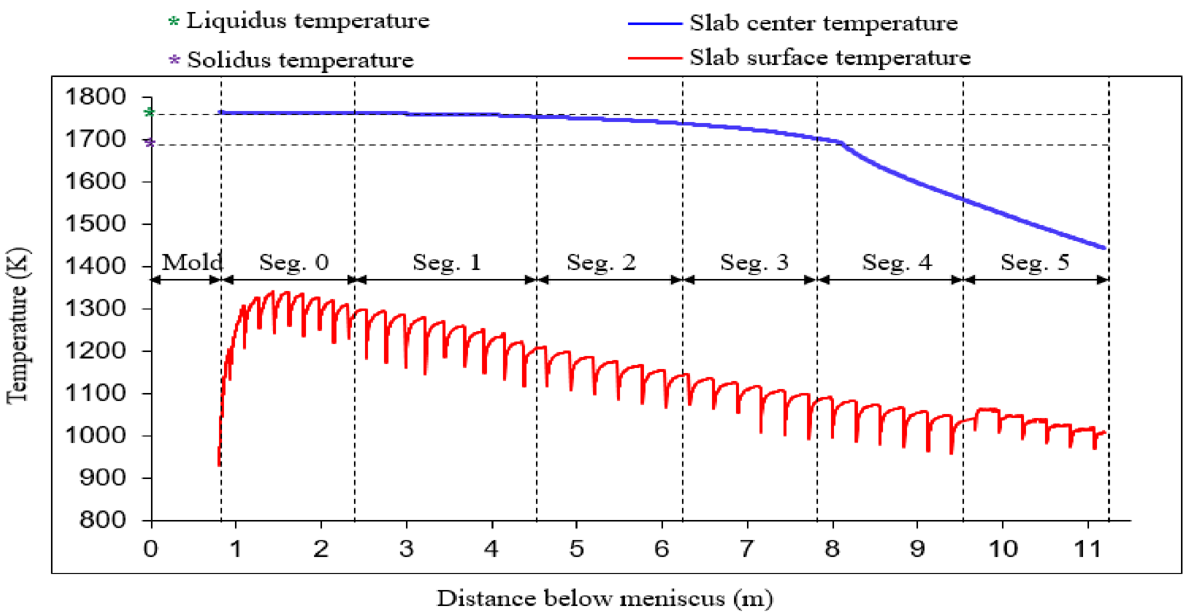

Figure 5-18. Slab temperature profile

### 5.3.3 Metallurgical Length Prediction

Figure 5-19(a) shows a 3-D contour of the slab. The temperature is within the mushy zone range ($T_{solidus} \leq T \leq T_{liquidus}$). It is therefore the liquid portion of the steel as it solidifies down the caster. Figure 5-19(b) shows the shell growth along the caster until a complete solidification (metallurgical length) was achieved.

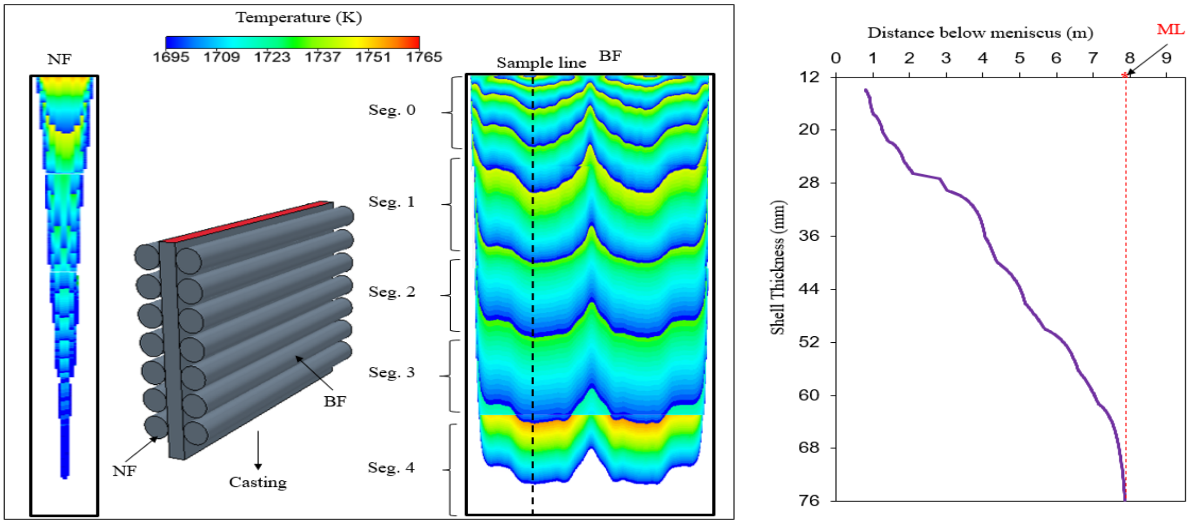

(a)

(b)

Figure 5-19. Whole caster solidification

# CONCLUSIONS

The study numerically investigated air-mist spray cooling by a Spraying System Co. flat-fan nozzle during the secondary cooling in continuous casting of steel using a three dimensional computational fluid dynamics simulation. The results have shown that the casting conditions have impact on the heat transfer during continuous casting of steel. A multivariable linear regression has been used to develop a correlation to predict the heat transfer coefficient using casting conditions such as air pressure, water flow rate, casting speed and standoff distance. The following conclusions can be drawn from the results of this study:

- Increase in air pressure increases the instabilities in the water nozzle resulting in faster breakup of water; the increased air pressure also impacts on the kinetic energy of the droplets and formation of smaller droplets that ultimately improves cooling. By increasing the air pressure from 30psi to 40psi, the droplets size could be reduced by 17% while the droplet velocity could be increased by 27.9%. This would result in an increase in the lumped HTC by 9.2%. this effect would be more if the air pressure is increased further although there is a risk of reduced cooling effect as the very small droplets produced upon further increase could evaporate before reaching the slab thereby reducing drastically the quantity of droplets available to cool the slab.
- Increase in air pressure could also lead to droplet loss due to air entrainment or the droplets evaporating before reaching the hot steel slab if the droplet size is very small.
- With increased water flow rate from 2gpm to 2.5gpm at a constant air pressure of 30psi, the weber number and Reynolds number at the nozzle outlet reduces by 33.8% and 25.9% respectively. Increase in water flow rate increases the number of droplets on the slab but the droplets have lower velocity and higher size resulting in lower cooling of the slab. The HTC could reduce by
- Increase in casting speed results in lower contact time between the droplets and the slab and thus lower cooling of the slab. At an air pressure of 40psi and a water flow rate of 2gpm, the cooling of the slab could decrease by 4.41% when the casting is increased from 45ipm to 50ipm and by 10.29% when it is further increased to 60ipm.

The solidification of steel was also studied to investigate certain parameters and how they affect shell growth and surface temperature. The air-mist spray cooling result was integrated into the solidification model and a simulation approach was developed to simulate the entire caster in order to predict the shell growth, metallurgical length and surface temperature of the steel slab. The following conclusions can be deduced from this study:

- As the roll diameter increases, the roller-slab contact spray area increases resulting in higher heat transfer and shell growth. However, this would limit the spray coverage area resulting in decrease in shell growth.
- As the roll gap increases, the spray coverage area increases resulting in higher heat transfer and shell growth. However, there is higher tendency of bulging to occure as the roll gap increases since the resistance to ferrostatic pressure would decrease
- Smaller ratio of the roll gap to roll diameter improves heat transfer and slab cooling as the heat transfer would increase and there would be sufficient resistance to ferrostatic pressure.
- Casting speed has a significant effect on solidification of steel while superheat has a negligible effect on solidification of steel in the secondary cooling zone. With higher casting speed, the slab surface temperature increases, shell thickness decreases which would also result in higher metallurgical length.

# FUTURE WORKS

Some works that would be done in the future includes investigation of the effect of nozzle-to-nozzle distance on slab cooling as well as the effect of water temperature on slab cooling in the two-fluid spray nozzle. Also, a two-dimensional HTC distribution could be developed using the HTC database and simulation results. For the solidification model, the bend along the caster would be considered as it was neglected in the present study. Also, an investigation would be made to find the cause of the high solidification rate that results in under-prediction of the metallurgical length. Finally, multiple cases could be simulated at different casting conditions and for different steel grades and a database could be generated from which a correlation could be generated to predict the metallurgical length from steel composition, casting speed and superheat.

# REFERENCES

[1] Laitinen, E.; Neittaanmaaki, P. On Numerical Simulation of the Continuous Casting Process. *J. Eng. Math.* **2003**, *22*, 335–354.

[2] Thomas, B.G. Continuous Casting (metallurgy). In *Yearbook of Science and Technology*; McGrow-Hill Co.: New York, NY, USA, 2004.

[3] Stahl: World Steel Production. 2009. Available online: http://www.stahlonline.de/english/business_and_politics/economic_and_trade_policy/steel_in_figures/start.asp (accessed on day 02-13-2020).

[4] "From steel to semi-finished products – tec-science", tec-science. [Online]. Available: https://www.tec-science.com/material-science/steel-making/steel-semi-finished-products-continuous-ingot-casting/ [Accessed: 14-Nov-2019].

[5] Sengupta, J.; Thomas, B.G.; Wells, M.A. The use of water cooling during the continuous casting of steel and aluminium. *Metall. Mater. Trans. B* **2005**, *36*, 187–204.

[6] Camporredondo, S.J.E.; Castillejos, E.A.H.; Acosta, G.F.A.; Gutie'rrez, M.E.P.; Herrera, G.M.A. Analysis of Thin-Slab Casting by the Compact-Strip Process: Part I. Heat Extraction and Solidification. *Metall. Mater. Trans. B* **2004**, *35*, 541–559.

[7] Hibbins, S.G.; Brimacombe, J.K. Characterization of heat transfer in the secondary cooling system of a continuous slab caster. *ISS Trans*. **1983**, *3*, 77–89.

[8] Lefebvre, A. H.; McDonell, V. G. Atomization and Sprays. In *Atomization and Sprays*, 2017

[9] R. A. Castleman, The Mechanism of atomization accompanying solid injection. NACA Report No 440 1932.

[10] Mitsutsuka, M.; Fukuda, K. Boiling phenomena and effects of water temperature on heat transfer in the process of immersion cooling of *Tsetsu Hagane* **1979**, *65*, 608–616.

[11] Mitsutsuka, M.; Fukuhisa, Y.; Wake, M.; Okajima, M.; Miyashita, N.; Takeda, Y. Development of Air-atomizing Mist Nozzles and Mist Cooling System for Continuous Casting *Trans. ISIJ* **1985**, *25*, 1244–1250.

[12] Mishra, P.C.; Nayak, S.K.; Pradhan, P.; Durga, P.G. Impingement Cooling of Hot Metal Strips in Runout Table—A Review. *Interfac. Phenom. Heat Transfer* **2015** *Vol. 3*, page 117-137 DOI: 10.1615/InterfacPhenomHeatTransfer.2014010574.

[13] Jeschar, R.; Reiners, U.; Scholz, R. Heat Transfer During Water and Water-Air Spray Cooling in the Secondary Cooling Zone of Continuous Casting Plants. In Proceedings of the 69th Steelmaking Conference, Washington, DC, USA, 6–9 April 1986; pp. 511–521.

[14] Raudensky, M.; Horsky, J. Secondary cooling in continuous casting and Leidenfrost temperature effects. *Ironmak. Steelmak.* **2005**, *32*, 159–164. https://doi.org/10.1179/174328105X15913.

[15] Horský, J.; Raudenský, M. Measurement of heat transfer characteristics of secondary cooling in continuous casting. *Metal* **2005**, 24–26.5.

[16] McGinnis, F.K.; Holman, J.P. Individual droplet heat-transfer rates for splattering on hot surfaces *Int. J. Heat Mass Transf.* **1969**, *12*, 95–108.

[17] Pedersen, C.O. An experimental study of the dynamic behavior and heat transfer characteristics of water droplets impinging upon a heated surface. *Int. J. Heat Mass Transf.* **1970**, *13*, 369–379.

[18] Balachandar, S.; Eaton, J.K. Turbulent dispersed multiphase flow. *Annu. Rev. Fluid Mech.* **2010**, *42*, 111–133.

[19] Crowe, C.T.; Schwarzkopf, J.D.; Sommerfeld, M.; Tsuji, Y. *Multiphase Flows with Droplets and Particles*; CRC Press: Boca Raton, FL, USA, 2011.

[20] Elghobashi, S. Particle-laden turbulent flows: Direct simulation and closure models. *Appl. Sci. Res*. **1991**, *48*, 301–314.

[21] Elghobashi, S. On predicting particle-laden turbulent flows. *Appl. Sci. Res*. **1994**, *52*, 309–329

[22] Elghobashi, S.; Truesdell, G.C. Direct simulation of particle dispersion in a decaying isotropic turbulence. *J. Fluid Mech*. **1992**, *242*, 655–700.

[23] Maxey, M.R. The gravitational settling of aerosol particles in homogeneous turbulence and random flow fields. *J. Fluid Mech*. **1987**, *174*, 441–465.

[24] Squires, K.D.; Eaton, J.K. Preferential concentration of particles by turbulence. *Phys. Fluids A* **1991**, *3*, 1169–1179.

[25] Momenifar, M.; Dhariwal, R.; Bragg, A.D. Influence of Reynolds number on the motion of settling, bidisperse inertial particles in turbulence. *Phys. Rev. Fluids* **2019**, *4*, 054301.

[26] Bec, J.; Homann, H.; Ray, S.S. Gravity-Driven Enhancement of Heavy Particle Clustering in Turbulent Flow. *Phys. Rev. Lett.* **2014**, *112*, 184501.

[27] Ireland, P.J.; Bragg, A.D.; Collins, L.R. The effect of Reynolds number on inertial particle dynamics in isotropic turbulence. Part 2. Simulations with gravitational effects. *J. Fluid Mech.* **2016**, *796*, 659.

[28] Dhariwal, R.; Bragg, A.D. Enhanced and suppressed multiscale dispersion of bidisperse inertial particles due to gravity. *Phys. Rev. Fluids* **2019**, *4*, 034302.

[29] Zhou, Y.; Wexler, A.S.; Wang, L.P. Modelling turbulent collision of bidisperse inertial particles. *J. Fluid Mech*. **2001**, *433*, 77.

[30] Chen, J.; Jin, G. Large-eddy simulation of turbulent preferential concentration and collision of bidisperse heavy particles in isotropic turbulence. *Powder Technol*. **2017**, *314*, 281.

[31] Kruis, F.E.; Kusters, K.A. The collision rate of particles in turbulent flow. *Chem. Eng. Commun*. **1997**, *158*, 201.

[32] Wang, L.P.; Maxey, M.R. Settling velocity and concentration distribution of heavy particles in homogeneous isotropic turbulence. *J. Fluid Mech*. **1993**, *256*, 27.

[33] Bec, J.; Biferale, L.; Boffetta, G.; Celani, A.; Cencini, M.; Lanotte, A.S.; Musacchio, S.; Toschi, F. Acceleration statistics of heavy particles in turbulence. *J. Fluid Mech*. **2006**, *550*, 349

[34] Ayyalasomayajula, S.; Warhaft, Z.; Collins, L.R. Modeling inertial particle acceleration statistics in isotropic turbulence. *Phys. Fluids* **2008**, *20*, 095104.

[35] Chang, K.; Malec, B.J.; Shaw, R.A. Turbulent pair dispersion in the presence of gravity. *New J. Phys*. **2015**, *17*, 033010.

[36] J.C. Lasheras, E. Villermauxm, E.J. Hopfinger, Break-up and atomization of a round water jet by a high-speed annular air jet by a high-speed annular air jet, J. Fluid Mech. 357 (1998)

[37] Jiang, D. J., Liu, H. F., Li, W. F., Xu, J. L., Wang, F. C., & Gong, X. (2012). Modeling atomization of a round water jet by a high-speed annular air jet based on the self-similarity of droplet breakup. *Chemical Engineering Research and Design*, *90*(2), 185–192. https://doi.org/10.1016/j.cherd.2011.07.006

[38] Ibrahim, A. A., & Jog, M. A. (2006). Nonlinear breakup of a coaxial liquid jet in a swirling gas stream. *Physics of Fluids*, *18*(11). https://doi.org/10.1063/1.2364262

[39] Eroglu, H.; Chigier, N.; Farago, Z. Coaxial atomizer liquid intact lengths. *Phys. Fluids A* **1991**, *3*, 303–308. https://doi.org/10.1063/1.858139.

[40] Engelbert, C.; Hardalupas, Y.; Whitelaw, J.H. Breakup phenomena in coaxial airblast atomizers. *Proc. R. Soc. Lond. A* **1995**, *451*, 189–229.

[41] Lin, S. P., & Reitz, R. D. (1998). Drop and Spray Formation From a Liquid Jet. *Annual Review of Fluid Mechanics*, *30*(1), 85–105. https://doi.org/10.1146/annurev.fluid.30.1.85

[42] Zhang, F., Müller, T., Zirwes, T., Wachter, S., Jakobs, T., Habisreuther, P., Zarzalis, N., Trimis, D., & Kolb, T. (2019). Numerical and Experimental Investigation of Primary Breakup of High-Viscous Fluid at Elevated Pressure. *Conference on Liquid Atomization and Spray Systems*, *December*, 1–8.

[43] Lasheras J and Hopfinger E. Liquid jet instability and atomization in a coaxial gas stream. Ann. Rev Fluid Mech 2000; 32: 275–308.

[44] Leroux, B.; Delabroy, O.; Lacas, F. Experimental study of coaxial atomizers scaling. Part I: Dense core zone. *At. Sprays* **2007**, *17*, 381–407.

[45] Zhao, H.; Liu, H.F.; Tian, X.S. Influence of atomizer exit area ratio on the breakup morphology of coaxial air and round water jets. *AIChE J.* **2014**, *60*, 2335–2345.

[46] Kumar, A.; Sahu, S. Liquid jet breakup unsteadiness in a coaxial air-blast atomizer. *Int. J. Spray Combust. Dyn.* **2018**, *10*, 211–230. https://doi.org/10.1177/1756827718760905.

[47] Dumouchel, C. (2008). On the experimental investigation on primary atomization of liquid streams. *Experiments in Fluids*, *45*(3), 371–422. https://doi.org/10.1007/s00348-008-0526-0

[48] Varga, C. M., Lasheras, J. C., & Hopfinger, E. J. (2003). Initial breakup of a small-diameter liquid jet by a high-speed gas stream. *Journal of Fluid Mechanics*, *497*, 405–434. https://doi.org/10.1017/S0022112003006724

[49] Lasheras J and Hopfinger E. Liquid jet instability and atomization in a coaxial gas stream. AnnRev Fluid Mech 2000; 32: 275–308

[50] Marmottant, P. H., & Villermaux, E. (2004). On spray formation. *Journal of Fluid Mechanics*, *498*, 73–111. https://doi.org/10.1017/S0022112003006529

[51] Kalaaji, A., Lopez, B., Attané, P., & Soucemarianadin, A. (2003). Breakup length of forced liquid jets. *Physics of Fluids*, *15*(9), 2469–2479. https://doi.org/10.1063/1.1593023

[52] Fraser, R. P., Dombrowski, N., & Routley, J. H. (1963). The atomization of a liquid sheet by an impinging air stream. *Chemical Engineering Science*, *18*(6), 339–353. https://doi.org/10.1016/0009-2509(63)80027-5

[53] Mugele, R. A., & Evans, H. D. (1951). Droplet size distribution in sprays. Industrial & Engineering Chemistry, 43(6), 1317-1324.

[54] Bhatia, J. C., Domnick, J., Durst, F., & Tropea, C. (1988). Phase-Doppler-anemometry and the log-hyperbolic distribution applied to liquid sprays. Particle & Particle Systems Characterization, 5(4), 153-164.

[55] Babinsky, E., & Sojka, P. E. (2002). Modeling drop size distributions. Progress in Energy and Combustion Science, 28(4), 303-329.

[56] Bhatia, J. C., Domnick, J., Durst, F., & Tropea, C. (1988). Phase-Doppler-anemometry and the log-hyperbolic distribution applied to liquid sprays. Particle & Particle Systems Characterization, 5(4), 153-164.

[57] Rosin, P., & Rammler, E. (1933). Laws governing the fineness of a powdered coal. Journal of the Institute of Fuel, 7.

[58] Hernández-Bocanegra, C. A., Minchaca-Mojica, J. I., Acosta-González, F. A., Zhou, X., & Thomas, B. G. (2013). Measurement of heat flux in dense air-mist cooling: Part II–The influence of mist characteristics on steady-state heat transfer. Experimental Thermal and Fluid science, 44, 161-173.

[59] Presser, C., Papadopoulos, G., & Widmann, J. F. (2006). PIV measurements of water mist transport in a homogeneous turbulent flow past an obstacle. Fire Safety Journal, 41(8), 580-604.

[60] Sheppard, D. T., & Lueptow, R. M. (2005). Characterization of fire sprinkler sprays using particle image velocimetry. Atomization and Sprays, 15(3)

[61] Popper, J., Abuaf, N., & Hetsroni, G. (1974). Velocity measurements in a two-phase turbulent jet. International Journal of Multiphase Flow, 1(5), 715-726.

[62] Yanta, W. (1973, July). Measurements of aerosol size distributions with a laser Doppler velocimeter/LDV. Proceedings of 6 th Fluid and Plasma Dynamics Conference, 705. Reston, VA: American Institute of Aeronautics and Astronautics.

[63] Zalay, A. D., Bouse, L. F., Carlton, J. B., Crookshank, H. R., Eberle, W. R., Howie, R. E., & Shrider, K. R. (1980). Measurement of airborne spray with a laser Doppler velocimeter. Transactions of the ASAE, 23(3), 548-0552.

[64] Zhang, Y. Z., Wen, Z., Zhao, Z. W., Huang, J., Wu, W. F., & Li, B. W. (2019). Velocity characteristics of air-mist jet during secondary cooling of continuous casting using PIV and LDV. ISIJ International, 59(6), 1072-1080.

[65] Lane, W. R. (1951). Shatter of drops in streams of air. Industrial & Engineering Chemistry, 43(6), 1312-1317.

[66] Hinze, J. O. (1955). Fundamentals of the hydrodynamic mechanism of splitting in dispersion processes. AIChE Journal, 1(3), 289-295.

[67] Kennedy, J. B., & Roberts, J. (1990, May). Rain ingestion in a gas turbine engine. Proceedings of 4th ILASS Meeting (p. 154). Institute for Liquid Atomization and Spray Systems.

[68] Nicholls, J. A., & Ranger, A. A. (1969). Aerodynamic shattering of liquid drops. AIAA Journal, 7(2), 285-290.

[69] AVCO Systems Division Wilmington. (1970). A study of drop breakup behind strong shocks with applications to flight (No. AVSD-0110-70-RR). Wilmington, MA: Reinecke, W. G., & Waldman, G. D.

[70] Liu, Z., & Reitz, R. D. (1997). An analysis of the distortion and breakup mechanisms of high speed liquid drops. International Journal of Multiphase Flow, 23(4), 631-650

[71] Taylor, G. I. (1963). The shape and acceleration of a drop in a high speed air stream. The Scientific Papers of GI Taylor, 3, 457-464.

[72] O'Rourke, P. J., & Amsden, A. A. (1987). The TAB method for numerical calculation of spray droplet breakup (No. 872089). SAE Technical Paper.

[73] Reitz, R. (1987). Modeling atomization processes in high-pressure vaporizing sprays. Atomization and Spray Technology, 3(4), 309-337.

[74] Reitz, R. D., & Bracco, F. V. (1986). Mechanisms of Breakup of Round Liquid Jets. In N. Cheremisnoff (Ed.), The Encyclopedia of Fluid Mechanics, 3. 223–249. Washington, D.C.: Department of Energy.

[75] Reitz, R. D., & Bracco, F. V. (1982). Mechanism of atomization of a liquid jet. Physics of Fluids, 25(10), 1730-1742.

[76] Beale, J. C., & Reitz, R. D. (1999). Modeling spray atomization with the KelvinHelmholtz/Rayleigh-Taylor hybrid model. Atomization and Sprays, 9(6).

[77] Patterson, M. A., & Reitz, R. D. (1998). Modeling the effects of fuel spray characteristics on diesel engine combustion and emission. SAE Transactions, 27-43.

[78] Apte, S. V., Gorokhovski, M., & Moin, P. (2003). LES of atomizing spray with stochastic modeling of secondary breakup. International Journal of Multiphase Flow, 29(9), 1503-1522.

[79] Tanner, F. X. (1997). Liquid jet atomization and droplet breakup modeling of nonevaporating diesel fuel sprays. SAE Transactions, 127-140.

[80] Ibrahim, E. A., Yang, H. Q., & Przekwas, A. J. (1993). Modeling of spray droplets deformation and breakup. Journal of Propulsion and Power, 9(4), 651-654.

[81] Chryssakis, C., & Assanis, D. N. (2008). A unified fuel spray breakup model for internal combustion engine applications. Atomization and Sprays, 18(5).

[82] Chryssakis, C. A., Assanis, D. N., & Tanner, F. X. (2011). Atomization models. In Handbook of Atomization and Sprays (pp. 215-231). Springer, Boston, MA.

[83] Haibo, M.; Justina, L.; Kaile, T.; Rui, L.; Michael, L.; Armin, S.; Chenn, Q.Z. Modelling of spray cooling with a moving steel slab during the continuous casting process. *Steel Res. Int.* **2019**, *90*, 18000393.

[84] Visaria, M.; Issam, M. Theoretical and experimental study of the effects of spray inclination on two-phase spray cooling and critical heat flux *Int. J. Heat Mass Transfer* **2008**, *51*, 2398.

[85] Mitsutake, Y.; Monde, M.J. Analytical method of two-dimensional inverse heat conduction problem using Laplace transformation: Effect of number of measurement point. *Heat Transfer* **2003**, *125*, 6.

[86] Mozumder, A.K.; Monde, M.; Woodfield, P.L.; Islam, M.A. Maximum heat flux in relation to quenching of a high temperature surface with liquid jet impingement *Int. J. Heat Mass Transfer* **2006**, *49*, 2877.

[87] Moravec, R.; Blazek, K.; Horsky, J.; Graham, J.; Fiegle, S.; Dombovic, T.; Kaurich, T. Coupling of Solidification model and Heat Transfer Coefficients to have Valuable Tool for Slab Surface Temperatures Prediction In Proceedings of the T in METEC InSteelCon, Düsseldorf, Germany, 27 June–1 July 2011.

[88] Kim, J. Spray cooling heat transfer: The state of the art. *Int. J. Heat Fluid Flow* **2007**, *28*, 753–767.

[89] Nitin, K.; Tatiana, G.R.; Peter, S.; Cam, T. A hydrodynamic model for subcooled liquid jet impingement at the Leidenfrost condition. *Int. J. Therm. Sci.* **2011**, *50*, 993–1000.

[90] Müller, H.; Jeschar, R. Untersuchung des Wärmeübergangs an einer simulierten Sekundärkühlzone beim Stranggießverfahren. *Arch. Eisenhüttenwesen* **1978**, *44*, 589–594.

[91] Choi, K.J.; Yao, S.C. Mechanisms of film boiling heat transfer of normally impacting spray. *Int. J. Heat Mass Transf.* **1987**, *30*, 311–318.

[92] Deb, S.; Yao, S.C. Analysis on film boiling heat transfer of impacting sprays. *Int. J. Heat Mass Transf.* **1989**, *32*, 2099–2112.

[93] Fujimoto, H.; Hatta, N.; Asakawa, H.; Hashimto, T. Predictable Modelling of Heat Transfer Coefficient between Spraying Water and a Hot Surface above the Leidenfrost Temperature. *ISIJ Int.* **1997**, *37*, 492–497.

[94] Horsky, J.; Raudensky, M.; Tseng, A.A. Heat transfer study of secondary cooling in continuous casting. In Proceedings of the AISTech 2005, Iron & Steel Technology Conference and Exposition, Charlotte, NC, USA, 9–12 May 2005.

[95] Mario, E.H.L.; Esther, M.G.M.; Castillejos, E.A.H. Heat Transfer and Observation of Droplet-Surface Interactions During Air-Mist Cooling at CSP Secondary System Temperatures. *Metall. Mater. Trans. B* **2016**, *47*, 1409.

[96] Gradeck, M.; Kouachi, A.; Lebouche, M.; Volle, F.; Maillet, D.; Borean, J.L. *Int. J. Heat Mass Transf.* **2009**, *52*, 1094.

[97] Islam, M.A.; Monde, M.; Woodfield, P.L.; Mitsutake, Y. *Int. J. Heat Mass Transf.* **2008**, *51*, 1226.

[98] Araki, K.; Moriyama, A. Theory on Deformation Behaviour of a Liquid Droplet Impinging onto Hot Metal Surface. *Trans. ISIJ* **1981**, *21*, 583–590.

[99] Wachters, L.H.J.; Westerling, N.A. The heat transfers from a hot wall to impinging mist droplets in the spheroidal state. *Chem. Eng. Sci.* **1966**, *21*, 1047–1056.

[100] Prinz, B.; Bamberger, M. Determination of heat transfer coefficient of air mist sprays. *Mater. Sci. Technol.* **1989**, *5*, 389–393.

[101] Jenkins, M.S.; Story, S.R.; Davies, R.H. Measurement and Characterisation of Air-Mist Nozzles for Spray Quenching Heat Transfer. In Proceedings of the 19th Australasian Chemical Engineering Conference, Newcastle, UK, 18–20 September 1991; pp. 161–169.

[102] Puschmann, F.; Specht, E. Transient measurement of heat transfer in metal quenching with atomized sprays. *Exp. Therm. Fluid Sci*. **2004**, *28*, 607–615.

[103] Bendig, L.; Raudensky, M.; Horsky, J. Spray parameters and heat transfer coefficients of spray nozzles for continuous casting. In Proceedings of the Seventy-Eight Steelmaking Conference, Iron and Steel Society, Nashville, TN, USA, 2–5 April 1995; pp. 391–398.

[104] Montes, R.J.J.; Castillejos, E.A.H.; Acosta, G.F.A.; Gutiérrez, M.E.P.; Herrera, G.M.A. Effect of the operating conditions of air-mists nozzles on the thermal evolution of continuously cast thin slabs. *Can. Metall. Q.* **2008**, *47*, 187–204.

[105] Castillejos, E.A.H.; Acosta, G.F.A.; Herrera, M.A.; Hernández, C.I.; Gutiérrez, M.E.P. Practical productivity gains—Towards a better understanding of air-mist cooling in thin slab continuous casting. In Proceeding of the Third International Congress of Steelmaking, Association of Iron and Steel Technology, Charlotte, NC, USA, 9–12 May 200., pp. 881–890.

[106] Schmidt, J.; Boye, H. Influence of velocity and size of the droplets on the heat transfer in spray cooling. *Chem. Eng. Technol.* **2001**, *24*, 255–260.

[107] Haibo, M.; Armin, S.; Chenn, Z. Numerical Development of Heat Transfer Coefficient Correlation for Spray Cooling in Continuous Casting. *Front. Mater.* **2020**, *7*, 577265.

[108] Mascarenhas, N.; Mudawar, I. Methodology for predicting spray quenching of thick-walled metal alloy tubes. *Int. J. Heat Mass Transfer* **2012**, *55*, 2953–2964.

[109] Agnieszka, C.R.; Zbigniew, M.; Andrzej, B. The influence of selected parameters of spray cooling and thermal conductivity on heat transfer coefficient. *Int. J. Therm. Sci.* **2016**, *110*, 52–64.

[110] Haibo, M.; Rui, L.; Micheal, L.; Armin, S.; Chenn, Z. Numerical Investigation of Spray Cooling at Various Operation Conditions during Continuous Casting of Steel. In Proceedings of the AISTech Conference, Pittsburgh, PA, USA, 6–9 May 2019.

[111] J. K. Brimacombe and K. Sorimachi, "Crack formation in the continuous casting of steel," *Metall. Trans. B*, vol. 8, no. 2, pp. 489–505, 1977.

[112] F. R. Camisani-Calzolari, I. K. Craig, and P. C. Pistorius, "A review on causes of surface defects in continuous casting," in *IFAC Proceedings Volumes (IFAC-PapersOnline)*, 2003, vol. 36, no. 24, pp. 113–121.

[113] S. Yu *et al.*, "Stress and Friction Distribution around Slab Corner in Continuous Casting Stress and Friction Distribution around Slab Corner in Continuous Casting Mold with Different Corner Structures," *Metall. Mater. Trans. B*, vol. 49, no. 3, pp. 866–876, 2018.

[114] Metzner AB (1985) Rheology of Suspensions in Polymeric Liquids. J. Rheol. New York, New York. vol. 29, no. 6:739–775

[115] Carman PC (1997) Fluid flow through granular beds, Chem. Eng. Res. Des., vol. 75:S32–S48.

[116] Thomas BG (2018) Intro to Continuous Casting - CCC - U of I. Continuous Casting Consortium. http://ccc.illinois.edu/introduction/basicphenom.html

[117] Thomas BG (2005) Modeling of Continuous-Casting Defects Related to Mold Fluid Flow. *AIST - 3rd Internat. Congress on Science & Technology of Steelmaking*, vol. 3, no. 7, pp. 847–861.

[118] Thomas BG (2003) Chapter 14 – Fluid Flow in the Mold. In: AISE Steel Foundation, Pittsburg, Pennsylvania

[119] Thomas, B. G., & Stone, D. (1998). Measurement of temperature, solidification, and microstructure in a continuous cast thin slab. Retrieved from CiteSeer$^X$

[120] J.K. Brimacombe, Crack formation in Continuous Casting of Steel, Continuous Casting, vol. 2, Iron & Steel Society of AIME, 410, Commonwealth Drive, Warrendale, PA 15086, p. 119–227.

[121] M.M. Wolf, Strand cast halfway cracks — how to read a sulphur print, ISS Steelmaking Conference Proceedings 82 (1999) 3–10.

[122] Thomas, B. G., O'Malley, R., Shi, T., Meng, Y., Creech, D., & Stone, D. (2000, August). Validation of fluid flow and solidification simulation of a continuous thin-slab caster. *Proceedings of Modeling of Casting, Welding, and Advanced Solidification Processes IX*, 20, 25. Aachen, Germany: Shaker Verlag GmbH.

[123] Thomas, B.G. Continuous Casting of Steel. Chapter 15 in Modeling for Casting and Solidification Processingx, New York, NY, 2001, pp. 499-540.

[124] J.K. Brimacombe, P.K. Agarwal, S. Hibbins, B. Prabhaker, and L.A. Baptista: in Continuous Casting, J.K. Brimacombe, ed., 1984, vol. 2, pp. 105–23.

[125] M.M. Wolf: Continuous Casting: Initial Solidification and Strand Surface Quality of Peritectic Steels, Iron and Steel Society, Warrendale, PA, 1997, vol. 9, pp. 1–111.

[126] Bryan Petrus, Kai Zheng, X. Zhou, Brian Thomas, Joseph Bentsman. Real-Time, Model-Based Spray-Cooling Control System for Steel Continuous Casting.

[127] K. Okuno, H. Naruwa, T. Kuribayashi, and T. Takamoto: Iron Steel Eng., 1987, vol. 12 (4), pp. 34–38.

[128] K.-H. Spitzer, K. Harste, B. Weber, P. Monheim, and K. Schwerdtfeger: ISIJ Int., 1992, vol. 32 (7), pp. 848–56.

[129] S. Barozzi, P. Fontana, and P. Pragliola: Iron Steel Eng., 1986, vol. 11, pp. 21–26.

[130] B. Lally, L. Biegler, and H. Henein: Metall. Trans. B, 1990, vol. 21B, pp. 761–70.

[131] A. Diener, A. Drastik: Archiv Eisenhu¨ttenwesen, 53 (1982), No 1, 13–20.

[132] B. Barber, B. Patrick, P. Watson, R. York, F. Kitching, H. Sha, K. Kraushaar, K. H. Spitzer: Revue de Metallurgie-CIT, 92 (1996), 1403–1412.

[133] R. Davies, N. P. Blake: Campbell: 4th Int. Continuous Casting Conference, Brussels (1988), 645–654.

[134] Nukiyama, S.; Tansawa, Y. Experiments on the atomization of liquids in anatomized jet. *Trans. Soc. Mech. Engrs. (Japan)* **1939**, *6*, II-7, II-15.

[135] Zeoli, N.; Tabbara, H.; Gu, S. CFD Modeling of Primary Breakup during Metal Powder Spray. *Chem. Eng. Sci.* **2011**, *66*, 6498–6504. https://doi.org/10.1016/j.ces.2011.09.014

[136] Altimira, M.; Rivas, A.; Anton, R.; Sanchez, L.G.; Ramos, J.C. Fan-Spray Atomizers Analysis through Mathematical Modeling. In Proceedings of the ILASS-Europe Conferences, Mugla, Turkey, 10–13 September 2007.

[137] Koutsakis, K.; Gu, S.; Vardelle, A. Three Dimensional CFD Simulation of Liquid Copper Break up for the Liquid Precursor Spraying. *Surf. Coat. Technol.* **2011**, *220*, 214–218. https://doi.org/10.1016/j.surfcoat.2012.12.010.

[138] Kalata, W.; Brown, K.; O'Donnell, S.; Schick, R.J. Transfer Efficiency for an Oil Spray Application. In Proceedings of the 26th ILASS Americas Annual Conference on Liquid Spray and Spray Systems, Portland, OR, USA, 16–19 May 2016.

[139] Alkhedhair, A.; Jahn, I.; Gurgenci, H.; Guan, Z.; He, S.; Lu, Y. Numerical Simulation of Water Spray in Natural Draft Dry Cooling Towers with a New Nozzle Representation Approach. *Appl. Therm. Eng.* **2016**, *98*, 924–935. https://doi.org/10.1016/j.applthermaleng.2015.10.118.

[140] http://www.spray-imaging.com/spray-description.html

[141] Crowe, C.T.; Sharma, M.P.; Stock, D.E. The Particle-Source-In Cell (PSI-CELL) Model for Gas-Droplet Flows. *J. Fluids Eng.* **1977**, *99*, 325–332.

[142] Zuckerman, N.; Lior, N. Jet impingement heat transfer: physics, correlations, and numerical modeling. *Adv. Heat Transfer* **2006**, *39*, 565.

[143] Menter, F.R. Multiscale model for turbulent flows In Proceedings of the AIAA 24th Fluid Dynamics Confernce, Orlando, FL, USA, 6–9 July 1993.

[144] Ishii, M. Thermo-fluid Dynamics Theory of Two-phase Flow. *Eyrolles Paris* **1975**, *75*, 29657.

[145] Hirt, C.W.; Nichols, B.D. Volume of fluid (VOF) method for the dynamics of free boundaries. *J. Comp. Phys.* **1981**, *39*, 201.

[146] Kothe, D.B.; Mjolsness, R.C. RIPPLE: A new model for incompressible flows with free surfaces. *AIAA J.* **1992**, *30*, 2694.

[147] Kothe, D.B.; Rider, W.J.; Mosso, S.J.; Brock, J.I.; Hochstein, J.S. Volume tracking of interfaces having surface tension in two and three dimensions. In Proceedings of the AIAA 34th Aerospace Sciences Meeting and Exhibit, Reno, NV, USA, 15–18 January 1996.; Paper 96-0859.

[148] Richards, J.R.; Beris, A.N.; Lenhoff, A.M. Drop formation in liquid–liquid systems before and after jetting. *Phys. Fluids* **1995**, *7*, 2617.

[149] Rayleigh, L. On the instability of jets. *Proc. Lond. Math. Soc.* **1878**, *1*, 4–13. https://doi.org/10.1112/plms/s1-10.1.4.

[150] Reitz, R.D. Atomization and Other Breakup Regimes of a Liquid Jet. Ph.D. Thesis, Princeton University, Princeton, NJ, USA, 1978.

[151] Nijdam, J.J.; Guo, B.; Fletcher, D.F.; Langrish, T.A. Lagrangian and Eulerian models for simulating turbulent dispersion and coalescence of droplets within a spray. *Appl. Math. Model*. **2006**, *30*, 1196–1211. https://doi.org/10.1016/j.apm.2006.02.001.

[152] Fung, M.C.; Inthavong, K.; Yang, W.; Tu, J. CFD modeling of spray atomization for a nasal spray device. *Aerosol. Sci. Technol.* **2012**, *46,* 1219–1226. https://doi.org/10.1080/02786826.2012.704098.

[153] O'Rourke, P.J.; Bracco, F.V. Modeling of Drop Interactions in Thick Sprays and Comparison with Experiments. *Instit. Mech. Eng.* **1980**, *404*, 80.

[154] Liu, A.B.; Mather, D.; Reitz, R.D. Modeling the Effects of Drop Drag and Breakup on Fuel Sprays. *SAE Int. J. Eng.* **1993**, *102,* 83–95.

[155] Ranz, W.E.; Marshall, W.R. Evaporation from Drops. *Chem. Eng. Progress* **1952**, *48*, 141–146.

[156] Naber, J.D.; Reitz, R.D. Modeling Engine Spray/Wall Impingement. *SAE Int. J. Eng.* **1988**, *97*, 118–140.

[157] Bernardin, J.D.; Mudawar, I. The Leidenfrost point: Experimental study and assessment of existing models. *J. Heat Trans*. **1999**, *121*, 894–903. https://doi.org/10.1115/1.2826080.

[158] Miller, R.S.; Harstad, K.; Bellan, J. Evaluation of Equilibrium and Non-Equilibrium Evaporation Models for Many Droplet Gas-Liquid Flow Simulations. *Int. J. Multiphase Flow* **1998**, *24*, 1025–1055.

[159] Sazhin, S.S. Advanced Models of Fuel Droplet Heating and Evaporation. *Progress Energy Combust. Sci.* **2006**, *32*, 162–214.

[160] Brackbill, J.U.; Kothe, D.B.; Zemach, C. A continuum method for modeling surface tension. *J. Comput. Phys.* **1992**, *100*, 335–354.

[161] Menter, F.R.; Kuntz, M.; Langtry, R. Ten years of experience with the SST turbulence model. *Turbul. Heat Mass Transf.* **2003**, *4,* 625–632.

[162] Patankar, S.V.; Spalding, D.B. A calculation procedure for heat, mass and momentum transfer in three-dimensional parabolic flows. *Int. J. Heat Mass Transf.* **1972***, 15*, 1787.

[163] Jadidi, M. Introduction to Multiphase Flows-Part#2 Fundamental Definitions & Choosing a Multiphase Model. Available online: https://www.researchgate.net/publication/312228367_Introduction_to_Multiphase_Flows-Part_2_Fundamental_Definitions_Choosing_a_Multiphase_Model (accessed on 04-06-2021). https://doi.org/10.13140/RG.2.2.15465.29284.

[164] Menter FR (1994) Two-equation eddy-viscosity turbulence models for engineering applications. AIAA J., vol. 32, no. 8:1598–1605

[165] Pfeiler, C. (2008). *Modeling of turbulent particle/gas dispersion in the mold region and particle entrapment into the solid shell of a steel continuous caster* [Doctoral dissertation; University of Leoben]. ResearchGate

[166] Pfeiler, C., Wu, M., & Ludwig, A. (2005). Influence of argon gas bubbles and non-metallic inclusions on the flow behavior in steel continuous casting. *Materials Science and Engineering: A*, *413*, 115-120

[167] Pfeiler, C., Thomas, B. G., Wu, M., Ludwig, A., & Kharicha, A. (2008). Solidification and particle entrapment during continuous casting of steel. *Steel Research International*, *79*(8), 599-607

[168] Voller, V., Markatos, N., & Cross, M. (1985). Techniques for accounting for the moving interface in convection/diffusion phase change. In R.W. Lewis & K. Morgan (Eds.), *Unknown Book Title* (pp. 595-609). Swansea, U. K.: Pineridge Press

[169] Voller, V. R., Markatos, N. C., & Cross, M. (1986). Solidification in convection-diffusion. In N. C. Markatos, M. Cross, D. G. Tatchell, & N. Rhodes (Eds.), *Numerical simulation of fluid flow and heat/mass transfer processes* (pp. 425-432). Berlin, Germany: Springer

[170] Voller, V. R., Cross, M., & Markatos, N. C. (1987). An enthalpy method for convection/diffusion phase change. *International Journal for Numerical Methods in Engineering*, *24*(1), 271-284

[171] Voller, V. R., & Prakash, C. (1987). A fixed grid numerical modelling methodology for convection-diffusion mushy region phase-change problems. *International Journal of Heat and Mass Transfer*, *30*(8), 1709-1719

[172] Voller, V. R., Brent, A. D., & Prakash, C. (1989). The modelling of heat, mass and solute transport in solidification systems. *International Journal of Heat and Mass Transfer*, *32*(9), 1719-1731.

[173] Ma, H. Numerical Study of Fluid Flow, Spray Cooling, and Thermo-Mechanical Behaviour in the Continuous Casting of Steel, [Doctoral dissertation; Purdue University, West Lafayette, Indiana], 2021.

[174] Reitz, R.D.; Diwakar, R. Structure of high-pressure fuel sprays. *SAE Paper* **1987**, 492–509.

[175] Louhenkilpi, Seppo, Jyrki Miettinen, and Lauri Holappa. "Simulation of microstructure of as-cast steels in continuous casting." *ISIJ international* 46, no. 6 (2006): 914-920.

[176] Leong, M.Y.; Hautman, D.J. TITLE In Proceedings of the ILASS Americas, 15th Annual Conference on Liquid Atomization and Spray Systems, Madison, WI, USA, 14–17 May 2002.

[177] Spray Analysis and Research Services. Spray Characterization of Nozzles Used in Casting Application. Laboratory Test Report. April 2016.

[178] Minchacha, M.J.I.; Castillejos, E.A.H.; Acosta, G.F.A. Size and velocity characteristics of droplets generated by thin steel slab continuous casting secondary cooling air-mist nozzles. *Metall. Mater. Trans. B* **2011**, *42*, 500–515.

[179] Sobhan Mosayebidorcheh; Mofid Gorji-Bandpy. Solidification and Thermal Performance Analysis of the Low Carbon Steel During the Continuous Casting Process. Journal of Advanced Materials and Processing, 2017, Vol. 5, No.3, 3-11.

[180] Hongming Wang, Guirong Li, Yucheng Lei, Yutao Zhao, Qixun Dai, Junjie Wang. Mathematical Heat Transfer Model Research for the Improvement of Continuous Casting Slab Temperature

# PUBLICATIONS

Anisiuba, V.; Ma, H.; Silaen, A.; Zhou, C. Computational Studies of Air-Mist Spray Cooling in Continuous Casting. Energies 2021, 14, 7339. https://doi.org/10.3390/en14217339

Anisiuba, V. E., Ma, H., Silaen, A., & Zhou, C. Q. (2021). Modeling of Air-Mist Spray in Continuous Casting of Steel. *Proceedings of AISTech-Iron and Steel Technology Conference 2021*, (12 pages). AIST Digital Library

Anisiuba, V. E., Ma, H., Silaen, A., & Zhou, C. Q. (2021). Numerical Investigation of Air-Mist Spray in the Secondary Cooling during Continuous Casting of Steel . *Proceedings of the 9th International on Modeling and Simulation of Metallurgical Processes in Steelmaking*. *STEELSIM Conference 2021*.The Austrian Society for Metallurgy and Materials